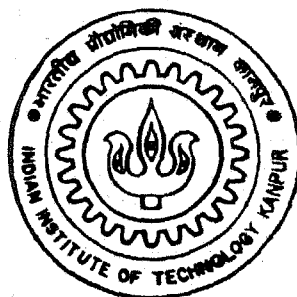


# Optimum Spacing of Vertical Parallel Plate Channels with Natural and Mixed Convection Cooling

By

**Ghulam Jilani**



TH  
ME/2001/D  
J563a

DEPARTMENT OF MECHANICAL ENGINEERING  
**INDIAN INSTITUTE OF TECHNOLOGY KANPUR**  
JUNE, 2001

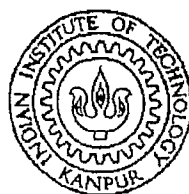
# Optimum Spacing of Vertical Parallel Plate Channels with Natural and Mixed Convection Cooling

A Thesis Submitted  
in Partial Fulfillment of the Requirements  
for the Degree of

DOCTOR OF PHILOSOPHY

*by*

Ghulam Jilani



to the

Department of Mechanical Engineering  
INDIAN INSTITUTE OF TECHNOLOGY, KANPUR

June, 2001

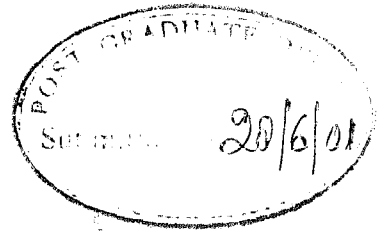
23 SEP 2003 / ME

पुष्पवैज्ञानिक कान्तिनाथ केतकर पुस्तकालय  
भारतीय प्रौद्योगिकी संस्थान कानपुर  
प्राप्ति क्र. A 145042.....



A145042

## CERTIFICATE



It is certified that the work contained in the thesis entitled **Optimum Spacing of Vertical Parallel Plate Channels with Natural and Mixed Convection Cooling**, by GHULAM JILANI, has been carried out under my supervision and that this work has not been submitted elsewhere for a degree.

Date: June 27, 2001

Professor V. Eswaran  
Department of Mechanical Engineering  
Indian Institute of Technology Kanpur  
Kanpur, 208016



To

my respected  
father and mother

# Acknowledgements

How inadequate are words in expressing my indebtedness, heartfelt gratitude, warm regards and sincere thanks to my humane thesis supervisor Professor Vinayak Eswaran, for giving me the freedom to work on my own problem which instilled in me the confidence in pursuing further research, earnest supervision, inspiring guidance, systematic approach, stimulating discussions, extensive care and generous help! He has been extremely kind, sympathetic and considerate to me. Without his extraordinary help during many crucial periods, this thesis could not have seen the light of day. His unwarranted help can never be forgotten.

With gratitude and respect I thank Professor P.S. Ghoshdastidar for his genuine help during a very crucial period of my research programme. I am greatly indebted to Professor T. Sunderajan for initiating me into the exciting field of Computational Fluid Dynamics and Heat Transfer, and to Professor V.K. Garg for giving me the opportunity to work on a CFD problem for my M.Tech thesis. I am also grateful to Professor Y. Jaluria for introducing me to the exciting field of Optimal Design of Thermal Systems.

With a deep sense of gratefulness, I would like to thank Professor M.P. Chandrashekar, Principal of R.E.C., Calicut, for taking a bold step in sanctioning me extraordinary leave which facilitated the completion of this thesis. I would like to express my deep sense of gratitude and thankfulness to Dr. Mohammed Ameen for taking care of my family at Calicut during my long stay at this Institute. I also wish to express my deep sense of appreciation to Professor P.M. Abdul Majeed who has been a constant source of encouragement.

I would like to thank Satya Prakash for his help while learning the spec-

tral element code, Asif Masood for his help while learning GnuPlot, Andallib Tariq for tips that improved the plots, and Atul Sharma, Abir, Arnab, and Rakesh for their generous cooperation. My sincere thanks are due to Miss Parvathi for the exemplary patience and dedication with which she typed the whole thesis.

I shall always carry fond memories of the time I have spent with Dr S.S.A. Razee, Dr. Faiz Ahmed Khan, M. Jawaid Siddiqui, Sheik Nazeer Ahmed, M. Sajid Khan, and Syed Atif Hussain.

Words fail me when I try to record the earnest support given by my brother-in-law Ehtesham bhai and my sister Ishrat during my research programme. I am also grateful to my father-in-law Janab Md. Zeauddin Saheb for his infallible support and help throughout my stay at this Institute. The help extended by brother-in-law Dr. Md.Shahabuddin during the last crucial period of the thesis is gratefully acknowledged.

This thesis has been a great test of patience for my wife Gulshan, sons Labeeb and Yoosuf, and daughters Nabeelah and Zakiyyah. They will really be relieved at its completion. I am immensely indebted to them for their enormous cooperation, endurance and understanding while I was occupied by this endeavour month after month, year after year!

Last but not the least, the silent support, best wishes and blessings of my parents and other family members have been the constant source of inspiration and encouragement throughout my research programme. Even to think of thanking them is to trivialise all that they have done for me. My profound debt to them, therefore, remains silent and unacknowledged.

Date: June 26, 2001

Ghulam Jilani  
Indian Institute of Technology Kanpur  
Kanpur, 208016

# Synopsis

---

Name of the Student: Ghulam Jilani Roll No.: 9310562

Degree for which submitted: Ph.D. in Mechanical Engineering

Thesis Title: Optimum Spacing of Vertical Parallel Plate Channels  
with Natural and Mixed Convection Cooling

Name of Thesis Supervisor: Professor V. Eswaran

Month & Year of Submission: June, 2001

---

This thesis is concerned with the optimum inter-plate spacing in vertical channels cooled by natural and mixed convective flows, in the particular context of applications in electronic cooling. The objective is to determine the optimum spacing between the channel walls that maximizes the heat transfer for various Grashof numbers ( $Gr_H$ ), in natural convection, and various combinations of Grashof and Reynolds ( $Re_H$ ) numbers, in mixed convection.

For the single channel case this is equivalent to maximising the average wall Nusselt number ( $Nu_{av}$ ), while in the multiple channel case it involves maximising the product of  $Nu_{av}A_r$ , where  $A_r$  is the aspect ratio of the channel. The computations are done on a single channel that is assumed to be one of an infinite array of similar channels. The single channel and multiple channel cases are essentially the volume unconstrained and volume constrained optimisation of the inter-plate spacing in an array of identical channels.

The flow is assumed to be two dimensional, incompressible and laminar, with negligible viscous dissipation. The Boussinesq approximation is assumed to be valid. The approach followed is to numerically solve the stream function, vorticity and temperature equations in the channel for flow conditions of natural and mixed convection, at various parameter values. The spectral element method of Patera (1984) is applied to the governing equations in pseudo-transient form. The latter are solved by time-stepping the stream function, vorticity and temperature fields to steady state, from arbitrary initial conditions. The average Nusselt number is then obtained from the steady state temperature field, and the optimum spacing is determined from computations in an appropriate range of  $A_r$ .

The optimisation for mixed convection is simpler to perform because the volume flow rate through the channel is known *a priori*. However in the natural convection case, the flow rate is unknown and has to be determined iteratively by obtaining a solution that balances the inertial, viscous, buoyancy and pressure forces in the channel.

The numerical simulations are done for  $Gr_H$  values of  $10^3$ ,  $10^4$ , and  $10^5$  for a Prandtl number of 0.70. For the mixed convection case, simulations are done for  $Gr_H = 10^3$ ,  $10^4$ , and  $10^5$ , and buoyancy parameter ( $Gr_H/Re_H^2$ ) values ranging from 0.1 to 1.5. In the natural convection multiple channel case and the mixed convection single channel case clearly optimal spacings are obtained. In the other cases either weak or asymptotic optima are observed. In the natural convection case, the flow rate vs  $A_r$  at the various  $Gr_H$  is also determined. The velocity and temperature fields give a graphic explanation of the physical processes that go into determining the optimum spacing.

Chapter 1 ("Introduction") of the thesis underscores the importance of the thesis problem in view of the great and continuing interest in electronic cooling. The latter has often been stylised, in a vast body of literature, in terms of the problem of convective heat transfer in parallel plate channels with and without protuberances. The literature on natural and mixed convection in parallel plate channels is surveyed in the chapter. The smaller body of work specifically referring to optimum inter-plate spacing is reviewed in detail.

These studies have been previously attempted for natural and forced convection flows only, making a similar study of the mixed convection problem a logical imperative. The present thesis seeks to remedy this lacuna and also to investigate aspects of the natural convection problem hitherto unexamined in earlier studies.

**Chapter 2** (“Mathematical Formulation”) formally presents the physical model assumed, the idealisations made, and the resulting mathematical model in terms of both the primitive variable velocity and pressure as well as the derived stream function and vorticity formulations. The separately nondimensionalised equations for natural and mixed convection are presented. The computation domain to be used and the associated boundary conditions are discussed in detail. The inertial, viscous, buoyancy and pressure force balance equation that needs to be satisfied by a natural convective flow is derived. The optimisation criterion for the inter-plate spacing for multiple channels is obtained.

**Chapter 3** (“Numerical Formulation”) presents the spectral element method of Patera (1984) adapted to the stream function and vorticity formulation used in the present study. The spectral discretisation based on the Chebyshev Gauss-Lobatto grid points is described. A finite-difference discretisation of the transient term of each governing equation, along with an implicit representation of the Laplacian terms, and explicit representations for the remaining terms, is shown to yield a Helmholtz equation. This is solved by a Chebyshev polynomial based variational formulation that yields a system of linear equations for the unknown variables at the grid points of each element. These elemental equations are combined, and along with the boundary conditions, solved by an LU decomposition method. A grid independence study demonstrates the levels of accuracy reached in the simulations.

**Chapter 4** (“Results and Discussion”) presents the numerical simulations for the natural and mixed convection cases separately. For natural convection, the steady state fields are obtained iteratively, for  $Gr_H = 10^3, 10^4$ , and  $10^5$ , over a range of  $A_r$ , and the optimum aspect ratio (i.e. the inverse of the optimum spacing) is determined for each  $Gr_H$ . Both constrained and unconstrained volume optima are determined, and are found to be strongly

dependent on  $Gr_H$ . The streamlines, velocity vectors and isotherms for typical cases are depicted and help to elucidate the physics involved. The volume flow rate as a function of  $Gr_H$  and  $A_r$  is also determined. A similar presentation of the mixed convection results is done for  $Gr_H = 10^3$ ,  $10^4$ , and  $10^5$ , with  $Gr_H/Re_H^2 = 0.1$ ,  $0.5$ ,  $1.0$ , and  $1.5$ . The optimum spacing is found to be strongly related to the  $Gr_H$  and buoyancy parameter values.

The conclusions of this study and the scope for future work are presented in Chapter 5.

# Contents

Certificate	iii
Dedication	v
Acknowledgements	vii
Synopsis	ix
List of Figures	xv
List of Tables	xix
Nomenclature	xxiii
<b>1 Introduction</b>	<b>1</b>
1.1 Background	1
1.2 Parallel Plate Channels and Electronic Cooling	3
1.3 Optimum Spacing of Parallel Plate Channels	5
1.4 Previous Studies on Parallel Plate Channels	7
1.4.1 Studies on Natural Convection	8
1.4.2 Studies on Mixed Convection	14
1.4.3 Studies on Optimum Spacing	18
1.5 Objective of the Present Investigation	24
<b>2 Mathematical Formulation</b>	<b>27</b>
2.1 Introduction	27
2.2 Physical Model	28
2.2.1 The Problem of Many Channels	28
2.2.2 The Problem in a Single Channel	29
2.3 Approximations and Idealisations	31
2.3.1 Boussinesq Approximation	31
2.4 Mathematical Model	32
2.4.1 Governing Equations	32
2.4.2 Boundary Conditions	33
2.5 Dimensionless Representation	37
2.5.1 Dimensionless Variables	39



2.5.2	Dimensionless Governing Equations . . . . .	40
2.5.3	Dimensionless Boundary Conditions . . . . .	41
2.6	Stream Function-Vorticity Formulation . . . . .	42
2.6.1	Vorticity Transport and Stream Function Equations . .	43
2.6.2	The Pseudo-Transient Forms . . . . .	44
2.6.3	Boundary Conditions . . . . .	45
2.7	Criteria for Optimum Spacing . . . . .	49
<b>3</b>	<b>Numerical Formulation</b>	<b>53</b>
3.1	Introduction . . . . .	53
3.2	Discretization of the Domain . . . . .	54
3.2.1	Grid Point Numbering . . . . .	57
3.3	Discretization of Governing Equations . . . . .	60
3.3.1	Temporal Discretization . . . . .	60
3.3.2	Spatial Discretization . . . . .	62
3.3.3	Variational Formulation . . . . .	62
3.3.4	Formation of Elemental Equations . . . . .	66
3.3.5	Formation of Global Equations . . . . .	68
3.4	Imposition of Boundary conditions . . . . .	69
3.5	Solution of Global Equations . . . . .	70
3.6	Numerical Solution Procedure . . . . .	70
3.7	Spatial Derivatives at Collocation Points . . . . .	71
3.8	Accuracy of the Simulations . . . . .	72
<b>4</b>	<b>Results and Discussion</b>	<b>75</b>
4.1	Natural Convection Case . . . . .	75
4.1.1	Fluid Flow and Heat Transfer Patterns . . . . .	76
4.1.2	Optimum Spacing and Volume Flow Rate in the Nat- ural Convection Case . . . . .	86
4.2	Mixed Convection Case . . . . .	96
4.2.1	Fluid Flow and Heat Transfer Patterns . . . . .	96
4.2.2	Optimum Spacing in the Mixed Convection Case . . .	104
4.2.3	Pressure Drop . . . . .	127
4.2.4	Flow Rates in Natural and Mixed Convection . . . . .	131
<b>5</b>	<b>Conclusions and Scope for Future Work</b>	<b>139</b>
5.1	Conclusions . . . . .	139
5.2	Scope of Future Work . . . . .	141
	<b>Bibliography</b>	<b>143</b>

# List of Figures

2.1	The Physical Model and the Coordinate System . . . . .	30
2.2	The Computational Domain and Boundary Conditions . . . . .	35
2.3	An alternate computational domain and boundary conditions .	38
2.4	Boundary conditions for the Vorticity & Stream-function formulation . . . . .	46
3.1	A nominal discretized computational domain . . . . .	55
3.2	A typical element in (a) the original coordinates, and (b) transformed local coordinates. . . . .	56
3.3	The grid-points and local two-index numbering in a typical element. . . . .	57
3.4	The (a) two-index and (b) one-index local numbering of grid-points in a typical element. . . . .	58
3.5	The global numbering of grid points in the computational domain. . . . .	59
4.1	Computational domain with boundary conditions for stream-function, vorticity and temperature. . . . .	77
4.2	Vector plots for three different Grashof numbers and aspect ratio, $A_r = 2.500$ , for the case of natural convection: (a) $Gr_H = 10^3$ ; (b) $Gr_H = 10^4$ ; (c) $Gr_H = 10^5$ . . . . .	79
4.3	Streamlines for three different Grashof numbers and aspect ratio, $A_r = 2.50$ , for the case of natural convection: (a) $Gr_H = 10^3$ ; (b) $Gr_H = 10^4$ ; (c) $Gr_H = 10^5$ . . . . .	80
4.4	Isotherms for three different Grashof numbers and aspect ratio, $A_r = 2.500$ , for the case of natural convection: (a) $Gr_H = 10^3$ ; (b) $Gr_H = 10^4$ ; (c) $Gr_H = 10^5$ . . . . .	81
4.5	Vector plots for four different plate-to-plate channel spacing and $Gr_H = 10^4$ , for the case of natural convection: (a) $A_r = 1.000$ ; (b) $A_r = 1.515$ ; (c) $A_r = 2.000$ ; (d) $A_r = 3.125$ . . . . .	82
4.6	Streamlines for four different plate-to-plate channel spacing and $Gr_H = 10^4$ , for the case of natural convection: (a) $A_r = 1.000$ ; (b) $A_r = 1.515$ ; (c) $A_r = 2.000$ ; (d) $A_r = 3.125$ . . . . .	83

4.7	Isotherms for four different plate-to-plate channel spacing and $Gr_H = 10^4$ , for the case of natural convection: (a) $A_r = 1.000$ ; (b) $A_r = 1.515$ ; (c) $A_r = 2.000$ ; (d) $A_r = 3.125$ . . . . .	85
4.8	Variation of average Nusselt number with aspect ratio at three different Grashof numbers, for the natural convection case. . .	91
4.9	Variation of the product of average Nusselt number and aspect ratio with aspect ratio at three different Grashof numbers, for the natural convection case. . . . .	93
4.10	Variation of dimensionless induced volume flow rate with aspect ratio at three different Grashof numbers, for the natural convection case. . . . .	94
4.11	Variation of the induced volume flow rate, differently non-dimensionalised, with aspect ratio at three different Grashof numbers, for the natural convection case. . . . .	95
4.12	Vector plots for three different Grashof numbers and $A_r = 2.50$ , $Gr_H/Re_H^2 = 1.0$ , for the case of mixed convection: (a) $Gr_H = 10^3$ ; (b) $Gr_H = 10^4$ ; (c) $Gr_H = 10^5$ . . . . .	98
4.13	Streamlines for three different Grashof numbers and $A_r = 2.50$ , $Gr_H/Re_H^2 = 1.0$ , for the case of mixed convection: (a) $Gr_H = 10^3$ ; (b) $Gr_H = 10^4$ ; (c) $Gr_H = 10^5$ . . . . .	99
4.14	Isotherms for three different Grashof numbers and $A_r = 2.50$ , $Gr_H/Re_H^2 = 1.0$ , for the case of mixed convection: (a) $Gr_H = 10^3$ ; (b) $Gr_H = 10^4$ ; (c) $Gr_H = 10^5$ . The volume flow rate $\Delta\Psi = 0.4$ for all cases. . . . .	100
4.15	Vector plots for four different channel spacing and $Gr_H = 10^4$ , $Gr_H/Re_H^2 = 1.0$ , for the case of mixed convection: (a) $A_r = 1.6667$ ; (b) $A_r = 2.7778$ ; (c) $A_r = 3.3333$ ; (d) $A_r = 5.0000$ . . .	101
4.16	Streamlines for four different channel spacing and $Gr_H = 10^4$ , $Gr_H/Re_H^2 = 1.0$ , for the case of mixed convection: (a) $A_r = 1.6667$ , $\Delta\Psi = 0.6$ ; (b) $A_r = 2.7778$ , $\Delta\Psi = 0.36$ ; (c) $A_r = 3.3333$ , $\Delta\Psi = 0.30$ ; (d) $A_r = 5.0000$ , $\Delta\Psi = 0.2$ . . . . .	102
4.17	Isotherms for four different channel spacing and $Gr_H = 10^4$ , $Gr_H/Re_H^2 = 1.0$ , for the case of mixed convection: (a) $A_r = 1.6667$ ; (b) $A_r = 2.7778$ ; (c) $A_r = 3.3333$ ; (d) $A_r = 5.0000$ . . .	103
4.18	Vector plots for four different channel buoyancy parameters and $Gr_H = 10^4$ , $A_r = 2.50$ , for the case of mixed convection: (a) $Gr_H/Re_H^2 = 0.1$ ; (b) $Gr_H/Re_H^2 = 0.5$ ; (c) $Gr_H/Re_H^2 = 1.0$ ; (d) $Gr_H/Re_H^2 = 1.5$ . . . . .	105
4.19	Streamlines for four different buoyancy parameters and $Gr_H = 10^4$ , $A_r = 2.50$ , for the case of mixed convection: (a) $Gr_H/Re_H^2 = 0.1$ ; (b) $Gr_H/Re_H^2 = 0.5$ ; (c) $Gr_H/Re_H^2 = 1.0$ ; (d) $Gr_H/Re_H^2 = 1.5$ . The volume flow rate $\Delta\Psi = 0.40$ for all cases. . . . .	106

4.20	Isotherms for four different buoyancy parameters and $Gr_H = 10^4$ , $A_r = 2.50$ , for the case of mixed convection: (a) $Gr_H/Re_H^2 = 0.1$ ; (b) $Gr_H/Re_H^2 = 0.5$ ; (c) $Gr_H/Re_H^2 = 1.0$ ; (d) $Gr_H/Re_H^2 = 1.5$ .	107
4.21	Variation of average Nusselt number with aspect ratio and buoyancy parameter, $Gr_H/Re_H^2$ , at $Gr_H = 10^3$ , for the case of mixed convection.	121
4.22	Variation of average Nusselt number with aspect ratio and buoyancy parameter, $Gr_H/Re_H^2$ , at $Gr_H = 10^4$ , for the case of mixed convection.	122
4.23	Variation of average Nusselt number with aspect ratio and buoyancy parameter, $Gr_H/Re_H^2$ , at $Gr_H = 10^5$ , for the case of mixed convection.	123
4.24	Variation of the product of average Nusselt number and aspect ratio with aspect ratio and buoyancy parameter, $Gr_H/Re_H^2$ , at $Gr_H = 10^3$ , for the case of mixed convection.	128
4.25	Variation of the product of average Nusselt number and aspect ratio with aspect ratio and buoyancy parameter, $Gr_H/Re_H^2$ , at $Gr_H = 10^4$ , for the case of mixed convection.	129
4.26	Variation of the product of average Nusselt number and aspect ratio with aspect ratio and buoyancy parameter, $Gr_H/Re_H^2$ , at $Gr_H = 10^5$ , for the case of mixed convection.	130
4.27	Variation of average pressure drop with aspect ratio and buoyancy parameter, $Gr_H/Re_H^2$ , at $Gr_H = 10^3$ , for the case of mixed convection.	132
4.28	Variation of average pressure drop with aspect ratio and buoyancy parameter, $Gr_H/Re_H^2$ , at $Gr_H = 10^4$ , for the case of mixed convection.	133
4.29	Variation of average pressure drop with aspect ratio and buoyancy parameter, $Gr_H/Re_H^2$ , at $Gr_H = 10^5$ , for the case of mixed convection.	134
4.30	Variation of imposed volume flow rate with aspect ratio and buoyancy parameter, $Gr_H/Re_H^2$ , at $Gr_H = 10^3$ and their comparison with the induced volume flow rate in the natural convection case.	135
4.31	Variation of imposed volume flow rate with aspect ratio and buoyancy parameter, $Gr_H/Re_H^2$ , at $Gr_H = 10^4$ and their comparison with the induced volume flow rate in the natural convection case.	136
4.32	Variation of imposed volume flow rate with aspect ratio and buoyancy parameter, $Gr_H/Re_H^2$ , at $Gr_H = 10^5$ and their comparison with the induced volume flow rate in the natural convection case.	137



# List of Tables

3.1	Expression for Parameter $\lambda^2$ and forcing function $f$ (natural convection flow) . . . . .	72
3.2	Expression for Parameter $\lambda^2$ and forcing function $f$ (mixed convection flow) . . . . .	72
3.3	Grid Convergence test based on average Nusselt numbers for three different aspect ratio of the channel in the natural convection case at $Gr_H = 10^5$ . . . . .	73
4.1	Dimensionless induced flow rate( $\Delta\Psi$ ), average Nusselt number, and the product of average Nusselt number and aspect ratio for different aspect ratio of the channel at $Pr = 0.70$ , $Gr_H = 10^3$ . . . . .	86
4.2	Dimensionless induced flow rate ( $\Delta\Psi$ ), average Nusselt number, and the product of average Nusselt number and aspect ratio for different aspect ratio of the channel at $Pr = 0.70$ , $Gr_H = 10^4$ . . . . .	87
4.3	Dimensionless induced flow rate ( $\Delta\Psi$ ), average Nusselt number, and the product of average Nusselt number and aspect ratio for different aspect ratio of the channel at $Pr = 0.70$ , $Gr_H = 10^5$ . . . . .	88
4.4	Comparison of the present work with Anand et al. (1992), with regards to maximum average Nusselt number . . . . .	90
4.5	Range of optimum aspect ratios and maximum heat transfer rate for the single and multiple channel cases . . . . .	92
4.6	Variation of pressure drop, average Nusselt number, and the product of average Nusselt number and aspect ratio, with aspect ratio for mixed convection case at $Pr = 0.70$ , $Gr_H = 10^3$ , and $\frac{Gr_H}{Re_H^2} = 0.1$ . . . . .	108
4.7	Variation of pressure drop, average Nusselt number, and the product of average Nusselt number and aspect ratio, with aspect ratio for mixed convection case at $Pr = 0.70$ , $Gr_H = 10^3$ , and $\frac{Gr_H}{Re_H^2} = 0.5$ . . . . .	109

4.8	Variation of pressure drop, average Nusselt number, and the product of average Nusselt number and aspect ratio, with aspect ratio for mixed convection case at $Pr = 0.70$ , $Gr_H = 10^3$ , and $\frac{Gr_H}{Re_H^2} = 1.0$ . . . . .	110
4.9	Variation of pressure drop, average Nusselt number, and the product of average Nusselt number and aspect ratio, with aspect ratio for mixed convection case at $Pr = 0.70$ , $Gr_H = 10^3$ , and $\frac{Gr_H}{Re_H^2} = 1.5$ . . . . .	111
4.10	Variation of pressure drop, average Nusselt number, and the product of average Nusselt number and aspect ratio, with aspect ratio for mixed convection case at $Pr = 0.70$ , $Gr_H = 10^4$ , and $\frac{Gr_H}{Re_H^2} = 0.1$ . . . . .	112
4.11	Variation of pressure drop, average Nusselt number, and product of average Nusselt number and aspect ratio with aspect ratio for mixed convection case at $Pr = 0.70$ , $Gr_H = 10^4$ , and $\frac{Gr_H}{Re_H^2} = 0.5$ . . . . .	113
4.12	Variation of pressure drop, average Nusselt number, and the product of average Nusselt number and aspect ratio, with aspect ratio for mixed convection case at $Pr = 0.70$ , $Gr_H = 10^4$ , and $\frac{Gr_H}{Re_H^2} = 1.0$ . . . . .	114
4.13	Variation of pressure drop, average Nusselt number, and the product of average Nusselt number and aspect ratio, with aspect ratio for mixed convection case at $Pr = 0.70$ , $Gr_H = 10^4$ , and $\frac{Gr_H}{Re_H^2} = 1.5$ . . . . .	115
4.14	Variation of pressure drop, average Nusselt number, and the product of average Nusselt number and aspect ratio, with aspect ratio for mixed convection case at $Pr = 0.70$ , $Gr_H = 10^5$ , and $\frac{Gr_H}{Re_H^2} = 0.1$ . . . . .	116
4.15	Variation of pressure drop, average Nusselt number, and the product of average Nusselt number and aspect ratio, with aspect ratio for mixed convection case at $Pr = 0.70$ , $Gr_H = 10^5$ , and $\frac{Gr_H}{Re_H^2} = 0.5$ . . . . .	117
4.16	Variation of pressure drop, average Nusselt number, and the product of average Nusselt number and aspect ratio, with aspect ratio for mixed convection case at $Pr = 0.70$ , $Gr_H = 10^5$ , and $\frac{Gr_H}{Re_H^2} = 1.0$ . . . . .	118
4.17	Variation of pressure drop, average Nusselt number, and the product of average Nusselt number and aspect ratio, with aspect ratio for mixed convection case at $Pr = 0.70$ , $Gr_H = 10^5$ , and $\frac{Gr_H}{Re_H^2} = 1.5$ . . . . .	119

4.18	Range of optimum aspect ratio and corresponding average Nusselt number for different Grashof numbers and buoyancy parameters: single channel case . . . . .	120
4.19	Comparison of the theoretical and numerical values of the maximum product of average Nusselt number and aspect ratio for different Grashof numbers and buoyancy parameters . . . .	126
4.20	Optimum aspect ratio for different Grashof numbers and buoyancy parameters: multiple channel case . . . . .	126





# Nomenclature

Lower case symbols given in parenthesis are the dimensional counterparts of the nondimensional quantities denoted by upper case symbols on the same line.

$A_r$	aspect ratio of the channel
$a, b$	elemental location
$[C^i], [C]$	elemental left hand side coefficient matrices
$C_p$	specific heat at constant pressure
$\{e^i\}, \{e\}$	elemental right hand side coefficient matrices
$f$	forcing function in Helmholtz equation
$\{f\}$	array of forcing function values at the grid points
$Gr$	Grashof number
$g$	gravitational acceleration
$H$	channel height
$h$	convective heat transfer coefficient
$I$	functional in the variational formulation
$i_e, j_e$	element numbering indices
$k$	thermal conductivity
$L$	inter-plate spacing
$l$	dimensional height of the upstream plenum
$\dot{m}$	mass flow rate
$N_x$	Gauss-Lobatto Chebyshev points in $X$ -direction
$N_y$	Gauss-Lobatto Chebyshev points in $Y$ -direction
$P, (p)$	modified pressure
$Pr$	Prandtl number
$Q$	heat transfer rate
$q$	heat flux
$Re$	Reynolds number
$r_x$	number of elements in $X$ -direction
$r_y$	number of elements in $Y$ -direction
$S_\phi$	source term in the general transport equation
$T$	dimensional temperature
$t$	dimensional time

$U (u)$	velocity component in the X-direction
$U_c$	characteristic velocity
$U_o$	uniform inflow velocity (mixed convection case)
$V (v)$	velocity component in the Y-direction
$\dot{v}$	volume flow rate per unit channel depth
$W$	width of the constrained volumetric space
$X (x)$	coordinate along the plate
$\bar{x}, \bar{y}$	local elemental coordinates
$Y (y)$	coordinate normal to the plate surface

## Greek Symbols

$\alpha$	thermal diffusivity
$\beta$	coefficient of volumetric thermal expansion
$\Gamma$	diffusion coefficient
$\delta$	dimensionless temperature difference
$\epsilon_l$	dimensionless length of the upstream plenum
$\theta$	dimensionless temperature
$\Lambda$	constant coefficient in transport equation
$\lambda$	parameter in Helmholtz equation
$\nu$	kinematic viscosity
$\rho$	density
$\tau$	dimensionless time $\left[ = \frac{tU_c}{H} \right]$
$\Delta\tau$	dimensionless time step
$\phi$	dependent variable in general transport equation
$\Delta\Psi$	dimensionless volume flow rate $[ = -\Psi_b ]$
$\Psi (\psi)$	stream function
$\Delta\Psi^*$	differently nondimensionalised volume flow rate
$\Omega (\omega)$	vorticity

Subscripts

<i>av</i>	average
<i>b</i>	solid boundary
<i>ch</i>	channel
<i>j, k, l, m, p, q</i>	indices (including matrix indices)
<i>max</i>	maximum
<i>min.opt</i>	minimum optimum
<i>opt</i>	optimum
<i>w</i>	wall
$\infty$	free stream condition

Superscripts

<i>i</i>	elemental
<i>n</i>	time step



# Chapter 1

## Introduction

### 1.1 Background

With the continuing advances in science and technology, there has been a corresponding increase in the number of devices involving heat transfer in a wide variety of industries such as aerospace, automotive, energy production, electronics and many others. During their normal operation, the vital components (e.g., nuclear fuel rods, electronic chips) of many of these devices (i.e., nuclear reactors, electronic equipment) dissipate energy that may result in the increase in their temperature beyond a certain allowable limit. For example, in the electronic industry, the micro-miniaturization of Very Large Scale Integration (VLSI) has the consequence of packaging a very large number of components into one very small ‘chip’; and the attendant volumetric heat generation has risen to extremely high levels. Although the energy input in most electronic devices does not exceed a few watts, the power density (volumetric heat generation) is huge due to the small volume of electronic chips. This power density can reach megawatts per cubic meter. As a matter of fact, the power per unit volume that must be dissipated by modern electronic devices is of the same order of magnitude as that of a nuclear reactor (cf. Refai and Yovanovich, 1992)

Obviously, high power densities make it difficult to meet the limiting constraint on the maximum temperature imposed on critical components of such thermal systems by considerations of fatigue, melting, thermal stresses, and variation in material properties (Nigen and Amon, 1995). For instance,

the thermal design of printed circuit boards requires that the junction temperature of electronic components mounted on boards be maintained below  $125^{\circ}\text{C}$ , while the component case temperature should be between  $85$  and  $100^{\circ}\text{C}$  by reliability considerations. If the thermal control is inadequate, the excessive temperature will cause the electronic components and equipments to malfunction or burn out. Moreover, investigations, have demonstrated that a single electronic component operating  $10^{\circ}\text{C}$  beyond the maximum temperature can reduce the reliability of some systems by as much as 50% (cf. Lin and Hung, 1993). A single electronic chip which represents a multi-layer thin coating substrate assembly typically dissipates a heat flux of  $0.1\text{--}1\text{ MWm}^{-2}$  (cf. Elperin and Rudin, 1995). Since the components of this assembly are made of different materials such as ceramics, metals, semiconductors, the mismatch of the thermal expansion coefficients can cause high thermal stresses leading to the mechanical failure of the coating (Elperin and Rudin 1995). On the other hand, the widely differing dissipation rates from different chips on a single circuit board results in large temperature differences between these chips, again causing thermal stresses. Thus, even when the maximum temperature attained by the hottest chip is held within acceptable limit both electronic and mechanical failure could occur due to large inter-chip temperature difference (Garimella and Schlitz, 1995).

The problem of heat removal from heat generating thermal systems has been an area of extensive research and is very likely to become more important in the future due to the ever-increasing component volumetric heat generation rate. It is therefore essential to innovate and develop the most effective and reliable cooling techniques in order to ensure long component life and reliable performance. On the other hand, there is another class of thermal systems such as solar plate collectors, compact heat exchangers etc. which are exclusively used for energy collection, heating and cooling fluids without involving heat generation. Even though the thermal design of these thermal systems is generally not so complex, it is important to analyse their thermal performance. While substantial effort have been directed towards the research and development of advanced heating and/or cooling technologies, there is still a wide scope of understanding the fluid flow and heat transfer characteristics of thermal systems that require high performance heat transfer using components with progressively lighter weights, minimum volumes or accommodating shapes.

## 1.2 Parallel Plate Channels and Electronic Cooling

In a large number of cases of electronic cooling the geometric configuration addressed is that of an array of printed circuit boards stacked either horizontally or vertically each with an assortment of mounted electronic devices. In the simplest case, a pair of printed circuit boards can be reasonably treated as a parallel plate channel formed by smooth and negligibly thin heat generating boards. Indeed a large number of investigations pertaining to cooling of electronic equipments do make this simplifying approximation for the purpose of general parametric studies, (Bar-Cohen and Rohsenow, 1984; Hanzawa et al., 1988; Anand et al., 1992; Bejan and Sciubba, 1992; Morrone et al., 1997; Ledezma and Bejan, 1997).

The studies on parallel plate channels can typically be categorized in terms of the type of flow, thermal configuration, and the geometry involved. The types of flow are free (i.e., natural) convection, mixed convection, and forced convection. In natural convection, the buoyancy generated in a thermal field in the presence of a gravitational field essentially induces the flow. Natural convection cooling is passive in that it does not require an external source to provide the flow. It continues to play a prominent role in thermal management of low power electronic equipment because of its characteristically low operating noise, low cost, ease of maintenance, simplicity and absence of electromagnetic interference. Moreover, it is the only mechanism of heat dissipation from a heat generating plate to a coolant in the event of power failure. Its major disadvantage is that it usually cannot provide highly intensive cooling. Forced convection cooling is more suited for the latter cases, for here the flow is driven by an external source such as a fan or pump, etc. Given the intensity of flow, the cooling provided can be varied, unlike in natural convection. However, the major disadvantage of this mode of heat transfer is that an external source of power is needed. Mixed convection cooling is an intermediate mechanism of heat transfer in which both externally imposed as well as internally induced flows operate simultaneously. In a vertical channel, the main flow can be either upward or downward. The upward forced flow is termed 'buoyancy assisted' flow because of the natural convection created by buoyancy is in the same direction as the bulk flow. In contrast, the downward forced flow is called 'buoyancy opposed' flow as its



direction is opposite to that of natural convection.

The flow parameter that characterizes natural convection is the Grashof number,  $Gr$ . When the Grashof number is much larger than unity, the natural convection effects are significant. In typical cases of electronic cooling by natural convection the  $Gr$ , based on the height of the channel, usually lies in the range of  $10^2 - 10^5$  (see Anand et al., 1992, and Morrone et al., 1997, for instance). In mixed convection case, the relevant flow parameter quantifying the ratio of natural convection to forced convection effects is the buoyancy parameter,  $Gr/Re^2$ , where the Grashof number and the Reynolds number,  $Re$ , respectively represent the vigour of the natural convection and the forced convection effects. Physically, the magnitude of  $Gr/Re^2$  indicates the relative effect of buoyancy on forced convection. The limiting value of  $Gr/Re^2 \rightarrow 0$  and  $Gr/Re^2 \rightarrow \infty$ , correspond to the forced and natural convection limit, respectively. On the other hand, when  $Gr/Re^2$  is of the order of unity, the buoyancy effect will be comparable to the forced flow effect (Gebhart et al., 1988). In this thesis, we are concerned only with cases of free and mixed convection in vertical parallel plate channels.

The actual geometry of printed circuit boards with protruding devices having irregular shapes and sizes are very rarely simulated in theoretical studies, for not only does such geometry complicate the problem, it also makes it very specific to a particular situation or configuration. Thus, the vast majority of analytical, numerical and experimental studies deal with parallel plate channels either with smooth plane surfaces or surfaces with regularly spaced rectangular protrusions simulating electronic devices. Sometimes smooth parallel plate channels are used with regularly spaced heat sources simulating flush-mounted devices. Thus, parallel plate channels are often used to give a theoretical baseline in studies of electronic cooling. In this thesis, we are concerned only with smooth parallel plate channels.

The thermal boundary conditions that are used to simulate electronic cooling in parallel plate channels are typically either uniform temperature or uniform heat flux; sometimes, in order to simulate flush-mounted devices, these boundary conditions are applied on regularly spaced intervals on the walls alternating with sections where an insulated (i.e., no flux) boundary condition is applied to simulate the gaps between the electronic components. Apart from this, the channels might be considered to be either (a) symmetri-

cally heated simulating the mounting of the electronic devices on both sides of the channel walls or (b) asymmetrically heated where the uniform heat flux (or a relatively 'hot' uniform temperature) is applied only to one wall of the channel while the other is treated as an insulated boundary (or kept relatively 'cold' at a uniform temperature). This simulates situations where only one side of the printed circuit board has mounted electronic devices. Interestingly it has been shown by Bejan and Sciubba (1992) that the type of boundary conditions, i.e., constant temperature or constant heat flux, has little effect on the optimum spacing problem, which is the focus of this thesis. Thus, the present work analyses only the symmetrically heated constant temperature case.

Air-cooling is recognised as an important technique in the thermal design of electronic packages and promises to gain in importance because it is simple and robust, particularly with respect to safe operation (cf. Ledezma and Bejan, 1996). Thermal design engineers in the electronic industry are constantly trying to achieve even better performance with air-cooling.

### 1.3 Optimum Spacing of Parallel Plate Channels

In the foregoing section, it has been highlighted that heat-generating components are typically mounted on arrays of equidistant vertical circuit boards resembling heated parallel plate channels. The cooling of these circuit boards is crucial in maintaining a safe operating temperature and peak performance. However, the problem confronting the thermal design engineers is to obtain an adequate cooling design that balances performance with manufacturing and operating costs. An ill-conceived thermal design can either be ineffective thereby threatening the life span of a system, or over-designed, adding unnecessary size, weight and costs.

The fundamental problem of heat transfer augmentation, which finds an important application in the thermal design of electronic packages as well, mainly consists of maximizing the thermal conductance between the heat generating surface and the coolant. For the thermal design of a stack of

equidistant vertical heat generating circuit boards, this can be accomplished by suitably selecting the heat transfer mechanism, such as free, mixed or forced convection, and determining the optimum spacing between the circuit boards. The latter can be further classified as (a) volume unconstrained, and (b) volume constrained, optimization of inter-plate spacing. Volume unconstrained optimization will be applicable to optimum spacing in a single channel formed by a pair of parallel plates, while volume constrained optimization applies to several plates in a fixed volume. It is important to note that volume constrained optimization offers a new opportunity as in many applications it may be possible to vary the spacing between circuit boards stacked in a fixed volume such that the overall thermal conductance is maximum while the circuit boards are maintained within safe operating temperature limit.

The optimum spacing between heated parallel plates depends on a number of thermo-geometric parameters such as the coolant Prandtl number, height of the plates, thermal and geometric configuration of the plates and, most importantly, the Grashof number (for natural convection cooling) or both the Grashof number and the buoyancy parameter (for mixed convection cooling).

In the single channel case, as the spacing between the plates is increased keeping other parameters fixed, the coolant volume flow rate can be expected to increase. This increase is more unambiguous in mixed convection cooling, where the flow is partially imposed, in contrast to natural convection case. The increase in volume flow rate manifests in greater heat transfer rate. However, this increase in heat transfer rate is not expected to occur indefinitely with increase in spacing. As the spacing between the plates become large, the heat transfer rate from each plate tends to attain the single plate limit attained by a solitary plate in an infinite medium. In fact at somewhat lower values of inter-plate spacing the heated fluid causes upward suction popularly known as the 'chimney effect' that accelerates the flow and increase the heat transfer rate. Thus, the heat transfer in a parallel plate channel typically shows an increase and then a decrease with increasing inter-plate spacing, the latter decrease being not always clearly discernable. This optimum spacing is obviously of practical interest because it would give the maximum heat transfer in the channel. Its relevance to electronic cooling is obvious.

In the multiple channel case, a slightly different problem needs to be ad-

dressed. Here we are concerned with the maximization of heat transfer from a series of equal-spaced parallel plates in a fixed volume. For an allowable maximum temperature rise, the heat transferred to the channel decreases with decreasing spacing, but the total number of plates increases. Hence there is an optimum number of plates per unit volume. Therefore, if single channel case is essentially an unconstrained optimisation of heat transfer in a channel, the multiple channel case amounts to optimisation of heat transfer constrained by the space being occupied. It will be shown later that in the single channel case, the optimum is essentially that of the maximum average Nusselt number,  $Nu_{av}$  while in the multiple channel case, it is obtained at the maximum of the product of average Nusselt number and aspect ratio, i.e.,  $Nu_{av}A_r$  where  $A_r$  is the aspect ratio of the channel. The main thrust of this thesis is to determine the optimum spacing in single channel as well as multiple channels with natural and mixed convection cooling using air as the coolant.

## 1.4 Previous Studies on Parallel Plate Channels

Convective heat transfer in heated parallel plate channels is encountered in a wide variety of practical applications, such as heat exchanger design, solar energy collection, heating of buildings via Trombe walls, cooling of nuclear reactors and electronic packages. During the past several decades, these important applications — particularly, the cooling of modern electronic equipment — have motivated a vast amount of fundamental research into the structure of free, forced, and mixed convection flows through heated parallel plate channels, and of the optimum geometric arrangement of heated parallel plates cooled by natural and forced convection.

Since the focus in the present thesis is on the optimum spacing between symmetrically heated vertical parallel plates cooled by natural and mixed convection, only those papers, from a vast literature on parallel plate channels, most relevant to the present work will be presented in this section. In order to put the present study in perspective, the review is presented thus: in the first subsection, the investigations on natural convection in heated vertical parallel plates dealing with the fundamental aspects of the present

work are discussed. The next subsection focuses on the selected fundamental investigations on mixed convection in heated vertical parallel plates. Finally, in the third subsection, the complete literature dealing with the problem of optimum spacing between heated parallel plates is reviewed, classified further by the type of flow involved.

### 1.4.1 Studies on Natural Convection

Since the pioneering work of Elenbaas (1942), this topic has been studied extensively by many investigators. Analytical, experimental and numerical studies dealing with the effects of the heating mode (symmetrical or asymmetrical, uniform heat flux or uniform wall temperature), the inlet conditions and radiant heat exchange can be found in the literature. An excellent review of the previous work on this subject can be found in Peterson and Ortega (1990) and Manca, et al. (2000).

A numerical study of transient laminar free convection between symmetrically heated vertical parallel plates maintained at uniform temperature was done by Kettleborough (1972). In order to more realistically resolve the flow profile at the inlet of the channel, he was the first to use a computational domain that included, along with the actual physical domain between the two plates, a relatively large region upstream of the channel entrance. He also assumed that the velocity at the channel outlet was parallel to the walls and that the flow in the outflow region did not affect the flow field within the channel. Following a mixed stream function-vorticity and velocity formulation, the two-dimensional Navier-Stokes and energy equations incorporating the Boussinesq approximation were solved using the finite difference technique. He concluded that the steady state velocity profile at the inlet of the channel was parabolic for low Grashof numbers, while for high Grashof numbers a minimum at the centre existed. His predicted results were in poor agreement with that of Elenbaas (1942).

The same problem, including the entrance effect, was numerically investigated by Nakamura et al. (1982). Using the stream function-vorticity formulation along with the Boussinesq approximation, the system of elliptic Navier-Stokes and energy equations was solved in a similar computational domain as employed by Kettleborough (1972) with the difference that the wall

boundary condition for the stream function was obtained from the pressure drop along the channel walls. Special emphasis was given to the determination of induced mass flow rate between the plates. Their results, although significantly different from Kettleborough (1972), were found in reasonable agreement with Elenbaas (1942).

The effect of inter-plate spacing on laminar natural convection in a vertical channel bounded by an isothermal and an insulated unheated wall was studied both experimentally and numerically by Sparrow and Azevedo (1985). Consideration was given to the full range of operating conditions between the fully-developed limit and the single plate limit. The numerical solution was carried out by taking account of both natural convection in the channel and conduction in the wall. It was found that the flat plate heat transfer does not form an upper bound for the channel heat transfer. The authors concluded that the channel heat transfer is particularly sensitive to changes in inter-plate spacing for narrow channels and at small wall-to-ambient temperature differences.

A numerical study of transient natural convection in a symmetrically heated parallel plate vertical channel due to a step change in plate temperature was carried out by Chang and Lin (1989), including both the inlet and exit effects. Following the primitive variable approach, the full elliptic governing equations were solved employing a numerical scheme derived from the SIMPLER algorithm. The computational domain comprised the actual physical domain between the two plates, together with two relatively large regions respectively upstream and downstream of the channel. The time evolution of the flow and thermal fields and a correlation for the Nusselt number as a function of the Rayleigh number ( $Ra$ ) and the channel aspect ratio were presented for air for  $Ra$  varying from  $10^3$  to  $10^6$  and the aspect ratio from 5 to 10. It was concluded that the inclusion of the outflow region at the channel exit does not have a significant effect on their predicted value of steady state heat transfer.

The influence of the inlet velocity and pressure conditions on the natural convective flow within an asymmetrically heated channel was numerically studied by Chappidi and Eno (1990), for both uniform wall temperature and uniform heat flux heating conditions. Results were obtained by solving the boundary layer type governing equations in the physical domain between

the plates employing a uniform as well as a parabolic velocity profile, with and without pressure defect, as the inlet boundary conditions. The authors observed that for low Grashof number flows, inlet conditions do not have a significant effect on the flow and thermal fields while for high Grashof number flows, the flow and thermal fields are sensitive to the inlet conditions. They concluded that the assumption of zero pressure defect at the inlet results in higher predictions of local and overall Nusselt number than those obtained by considering the pressure defect.

Laminar free convection in channels formed between a series of vertical parallel plates with flush-mounted line heat sources was numerically investigated by Kim et al. (1991), for uniform heat flux conditions. The parabolized Navier-Stokes and energy equations were solved in an elemental channel domain using an implicit finite difference scheme employing a uniform velocity profile at the channel inlet and 'repeated' boundary conditions for the walls. The conduction inside the plates separating the channels was taken into account. The effect of repeated boundary conditions, and various geometric and thermal parameters (such as the thermal conductivity ratio of solid to air, the wall thickness to channel width ratio, and the modified Grashof number) on the mass flow rate, maximum surface temperature and average Nusselt number were discussed. The authors found that the repeated boundary condition reduces the maximum temperature, which occurs at the channel exit, and increases mass flow rate. It was also observed that as the wall conduction increases, mass flow rate through the channel increases and maximum surface temperature as well as the average Nusselt number on the hot surface decrease.

A numerical study of developing free convective flow between symmetrically heated isothermal vertical parallel plates, including entrance effects, was carried out by Naylor et al. (1991). Incorporating the Boussinesq approximation, the full elliptic Navier-Stokes and energy equations were solved using a finite element commercial code. In order to resolve the inflow boundary conditions, the channel together with a semicircular region placed upstream of the channel entrance was used as computational domain. While the boundary conditions at the semicircular inflow boundary were obtained from Jeffrey-Hamel flow, fully-developed flow conditions were imposed at the channel exit. The comparison of their results to those by Kettleborough (1972) and Nakamura et al. (1982) showed a greater accordance with the

results of Nakamura et al. (1982). Considering the pressure defect at the entrance, parabolized Navier-Stokes and energy equations were also solved numerically using an explicit forward marching finite difference scheme. Detailed comparisons of the parabolic and elliptic solutions showed that an elliptic solution is necessary to get accurate local quantities. However global quantities (such as total flow rate and average Nusselt number) predicted by the elliptic and parabolic solutions were in good agreement.

With a view to enhance the understanding of flow and heat transfer in the low Rayleigh number regime, Martin et al. (1991) numerically studied the natural convection flow through a large array of equal-spaced vertical parallel plates, including entrance effects. Consideration was given to symmetrically heated thin plates at a uniform wall temperature. Invoking the Boussinesq approximation, the full elliptic Navier-Stokes and energy equations were solved employing a variant of the SIMPLE and SIMPLEC algorithms. The computational domain comprised the actual physical domain between the two plates forming a single channel together with an upstream plenum of width equal to the inter-plate spacing. The effect of the height of the plenum on the heat transfer and fluid flow characteristics of the array of channels was evaluated. It was shown that the Elenbaas(1942) asymptotic expression for low Rayleigh numbers would be valid as a very special limiting case. The authors concluded that the heat transfer at low Rayleigh numbers would depend on the shape and boundary conditions of the upstream plenum.

Buoyancy-induced flow resulting from the symmetrical heating of two vertical parallel plates maintained at constant temperature was numerically investigated by Shyy et al. (1992), including entrance and exit effects. Full elliptic Navier-Stokes and energy equations in a nonorthogonal curvilinear coordinate system, with the Boussinesq approximation, were solved using a second-order accurate finite difference scheme with a self-adaptive grid technique. Computational domain consisted of the converging inflow region beneath the parallel surfaces, the region between them, and the diverging outflow region above. The results were obtained for a Prandtl number of 0.7, Grashof numbers ranging between  $10^3$  to  $10^5$  and channel aspect ratios of 1 and 2. The authors observed that the downstream plume solution, especially the pressure distribution, did not match the interior flow field produced by the side entrainment of the wake emanating from the vertical channel, but this mismatch between the two solutions did not significantly affect the flow



field within the channel.

The behaviour of natural convective flow in a symmetrically heated vertical, isothermal, parallel plate channel when adiabatic extensions of various sizes and shapes are added to the downstream part of the channel was analysed both numerically and experimentally by Straatman et al. (1993). Full elliptic Navier-Stokes and energy equations were solved using the finite element method. While fully developed flow conditions were used at the exit of extension, the inlet boundary conditions were based on Jeffrey-Hamel flow employed previously by Naylor et al. (1991). Experiments were conducted with ambient air using a Mach-Zehnder interferometer. An excellent agreement between experimental and numerical results was obtained. The results were presented for  $Pr = 0.7$  over a wide range of wall heating conditions. The authors observed that the adiabatic extension resulted in overall heat transfer enhancement, in all cases studied. A single correlation accounting for the channel aspect ratio, expansion ratio, modified Rayleigh number and heated length ratio was presented.

The effect of Prandtl number and aspect ratio on laminar natural convection in an asymmetrically heated vertical channel was numerically investigated by Hernandez et al. (1994), for the uniform wall temperature condition. The full elliptic Navier-Stokes and energy equations incorporating the Boussinesq approximation, were solved using a finite-volume discretization technique. The computational domain comprised the region between the plates and a relatively large upstream region. The results were presented for a wide range of Prandtl numbers, aspect ratios, and modified Rayleigh numbers. Correlations of the average Nusselt number as a function of modified Rayleigh number for different Prandtl numbers were proposed. It was found that for low values of the modified Rayleigh number, the average Nusselt number does not follow the asymptotic behaviour corresponding to the fully developed regime unless the aspect ratio is sufficiently large. This was attributed to the upstream conduction effects outside the channel.

Fujii et al. (1994) numerically and experimentally investigated the laminar free convection flow in an array of asymmetrically heated vertical parallel plate channels, taking into account the conduction within the plates. While one side of each plate was subjected to a uniform heat flux, the other side was cooled in the adjacent channel. Using stream function-vorticity ap-

proach, the full elliptic Navier-Stokes and energy equations in the fluid and the two-dimensional heat conduction equation in the plate were solved. A single heated plate along with the fluid regions in the two channels adjacent to the plate was taken as the computational domain. The experiments were carried out for an array of five vertical parallel plates. A close agreement between measured and computed induced flow rates was reported, except at aspect ratios below 8. Correlation expression for the local Nusselt number proposed could predict the plate temperature distributions within an error of  $\pm 5\%$ .

Free convection heat transfer in multiple vertical channels formed by a series of symmetrically heated parallel plates of finite thickness and maintained at uniform temperature was numerically studied by Floryan and Novak (1995). Special emphasis was given to inflow regions below the inlet of the channels. Invoking the Boussinesq approximation, the full elliptic Navier-Stokes and energy equations in primitive variables were solved using the finite element FIDAP code. The computational domain comprised half of the plate, half of the flow region between the two plates, together with a plenum upstream of the channel having a width equal to that of the channel. The height of the plenum was taken as ten percent of the channel height. While the boundary conditions at the outflow boundary were assumed to be fully-developed conditions, an upward free stream flow condition with zero normal gradient of the vertical component of velocity was employed at the inflow boundary of the upstream plenum. Results were presented for aspect ratios ranging from 4 to 20 and Grashof numbers (based on the channel half width) up to  $10^5$ . The authors reported that the channels interact with each other and that the heat transfer can be significantly increased by placing channels sufficiently close to each other. They also showed that the overall heat transfer can be increased up to 18 percent. If only the entrance zone is considered the average Nusselt number may increase by up to 48 percent.

The effect of adiabatic chimneys on convective heat transfer in a series of symmetrically heated vertical parallel plate channels maintained at uniform temperature was numerically investigated by Shahin and Floryan (1999). Invoking the Boussinesq approximations full elliptic Navier-Stokes and energy equations were solved using a finite element commercial code. The computational domain was similar to that of Martin et al. (1991). The authors observed that the addition of adiabatic chimneys enhances the heat transfer

for all configurations considered.

Most recently, Campo et al. (1999) numerically analysed the effect of adding insulated extensions to a symmetrically heated vertical parallel plate channel cooled by natural convection. The plates were subjected to uniform heat flux heating conditions and insulated extensions were appended either at the inlet or at the exit of the channel. Using the stream function-vorticity approach, the full elliptic Navier-Stokes and energy equations, invoking the Boussinesq approximation were solved by employing control volume method. While vorticity and energy equations were solved by implementing the alternating direction implicit (ADI) scheme with a false transient procedure, the stream function was obtained by the successive over relaxation method. The computational domain consisted of the region between the plates combined with two relatively large domains, one placed upstream of the channel inlet and the other downstream of the channel exit. The results were presented in terms of wall temperature profiles, induced mass flow rates, and pressure profiles. The authors observed that the insulated extensions appended at the exit of the channel resulted in a reduction of the maximum wall temperature. A dramatic increase in maximum wall temperature was observed when the insulated extensions was added to the inlet of the channel.

#### 1.4.2 Studies on Mixed Convection

Laminar mixed convection in vertical parallel plate channels has received considerable attention owing to its numerous practical applications. A comprehensive review of the literature on this topic can be found in Aung (1987), Incropera (1988), and Gebhart et al. (1988). In this section, the review of the most relevant previous studies are presented.

Analysis of mixed convection in the entry region of a symmetrically heated vertical parallel plate channel was obtained analytically by Yao (1983), for both uniform wall temperature and uniform heat flux. The results, valid in the developing flow region, reveal information on the different length scales that distinguish various convective mechanisms. It was also shown that natural convection eventually becomes the dominant heat transfer mode if  $Gr > Re$  for constant wall temperature, and if  $Gr^2 > Re$  for constant heat flux walls. The author also conjectured that reverse flow may be present in

the fully developed region when the channel walls are maintained at uniform temperatures.

Chow et al. (1984) numerically investigated the simultaneous effects of buoyancy and axial conduction on the forced convection in a short vertical parallel plate channel at low Peclet numbers. The plates were maintained at equal constant temperatures and both heating and cooling were considered. In order to assess the effect of axial conduction in the upstream and downstream directions, adiabatic extensions were added to the parallel plate channel. Using the stream function and vorticity formulation, the full elliptic Navier-Stokes and energy equations were solved in the extended physical domain employing a finite difference scheme. While parabolic velocity and uniform temperature profiles were assumed at the inlet of the upstream insulated region, fully developed conditions were applied at the exit of downstream insulated section. The authors observed that the effect of axial conduction at low Peclet numbers were significant both in the cases of heating and cooling. It was also observed that for the case of heating, free convection effects counter axial conduction somewhat near the entrance to the heated section whereas in cooling, axial conduction is enhanced. The enhancement of heat transfer in heating was observed when free convection effects became significant.

Steady laminar developing mixed convection of air in a vertical parallel plate channel was numerically studied by Habchi and Acharya (1986). Consideration was given to symmetric heating with uniform temperature as well as asymmetric heating with one plate maintained at uniform temperature and the other insulated. Assuming uniform velocity and temperature profiles at the inlet of the channel, the parabolic governing equations were solved using an implicit finite difference scheme. Results were presented for Rayleigh numbers ranging from  $10^3$  to  $10^6$  and buoyancy parameters in the range of 0.1-5. It was shown that air temperature in the channel increases with increasing buoyancy parameter and decreasing Rayleigh number. The authors also showed that the local Nusselt number attains its maximum value near the inlet of the channel and increases with decreasing buoyancy parameter.

Developing laminar mixed convection, including flow reversal, in a heated vertical parallel plate channel was numerically investigated by Aung and

Worku (1986a). The channel walls were subjected to uniform, but not necessarily equal, temperatures. Employing uniform velocity and temperature profiles at the inflow boundary, the parabolic conservation equations were solved using a fully implicit finite difference scheme coupled with a marching solution procedure. The results were obtained for a wide range of buoyancy parameter and wall temperature difference ratios, for  $Pr = 0.72$ . The authors showed that buoyancy forces could cause severe distortion in the velocity profiles, especially under asymmetric heating condition. In the symmetric heating case the distortion disappeared and the velocity profile became fully developed with a parabolic shape at some distance from the channel entrance. Quantitative results for the Nusselt number and bulk temperature indicated that the buoyancy force and asymmetric heating have a profound influence on the heat transfer process. It was also shown that buoyancy dramatically increases the hydrodynamic entrance length but diminishes the thermal development distance.

Aung and Worku (1986b) analytically analysed the fully developed laminar mixed convection including flow reversal in a vertical parallel plate channel in which the two walls were maintained at uniform, but not necessarily equal, temperatures. The authors obtained an exact solution for velocity and temperature and presented a criterion for the occurrence of the flow reversal. The said criterion implied that for asymmetric heating, reverse flow occurs if the parameter  $Gr/Re$  exceeds a certain threshold value.

A numerical study dealing with developing laminar mixed convection between asymmetrically heated vertical parallel plate channels was carried out by Aung and Worku (1987). In this study, the channel walls were maintained at uniform but unequal heat fluxes. The governing equations, inflow boundary conditions and numerical solution technique employed in this investigation were similar to those used in their previous study (Aung and Worku, 1986a). The velocity and temperature profiles were presented for a wide range of buoyancy and asymmetric heating parameters. From the comparison between the uniform wall temperature and uniform heat flux cases, it became evident that there are significant differences between the corresponding velocity and temperature profiles in mixed convection between asymmetrically heated plates. It was shown that for a uniform heat flux heating condition, buoyancy introduces a lesser degree of skewness in the velocity distribution, and so flow reversal is more prone to occur in uniform wall temperature sit-

uation. In particular, no flow reversal was observed for  $Gr/Re$  up to 500.

Steady laminar mixed convection of air in a vertical parallel plate channel including flow reversal was numerically investigated by Ingham et al. (1988a). The channel walls were subjected to equal constant temperature and both heating as well as cooling conditions were considered. Neglecting axial diffusion, the parabolic governing equations in the stream function and vorticity formulation were solved using a fully implicit finite difference scheme and a marching procedure. Emphasis was placed on flow reversal near the centre of the channel or adjacent to the plates. Numerical results in the form of velocity and temperature profiles, Nusselt numbers and friction factors were presented for  $Gr/Re$  values ranging from -300 to 70. For large magnitudes of  $Gr/Re$ , reverse flow was observed; and heat transfer was greatly enhanced over the section containing reverse flow.

Ingham et al. (1988b) numerically studied the steady laminar mixed convection in a vertical parallel plate channel subjected to unequal constant temperature walls. Both cases of heating and cooling were analysed. Unlike Ingham et al. (1988a), emphasis was placed on flow reversals that were adjacent to the colder wall. Assuming the stream wise diffusion to be negligible the solution of the boundary layer type equations were obtained by the numerical technique used in the previous study (Ingham et al., 1988a). The results showed good agreement with existing literature. A significant improvement in the heat transfer in the section of the channel with reverse flow was observed. As expected, buoyancy aiding flow enhanced the heat transfer, whereas buoyancy opposing flow inhibited it.

The Reynolds number dependence of laminar mixed convective flow between asymmetrically heated vertical parallel plates, with and without flow reversal, was numerically examined by Jeng et al. (1992). Uniform wall temperature heating conditions were considered. The full Navier-Stokes and energy equations in the primitive variables were solved using the SIMPLER algorithm on a staggered grid. The classical second-order upwind scheme was adopted to model the convective terms. While uniform velocity and temperature profiles were assumed at the inlet of the channel, first-order extrapolation was invoked at the exit of the channel. Results were presented for a wide range of asymmetry parameters, Reynolds numbers and the buoyancy parameter,  $Gr/Re$ . The authors found that for  $Re \geq 50$ , both flow

and thermal characteristics are independent of  $Re$  for fixed asymmetry and buoyancy parameters.

A numerical study of laminar steady state buoyancy aided mixed convection between a series of vertical equal-spaced parallel plates including wall conduction was carried out by Wastson et al. (1996). While one surface of each plate was subjected to a planar heat source, the opposite surface was exposed to the flowing fluid in the adjacent channel. Invoking Boussinesq approximations, the full elliptic Navier-Stokes and energy equations in primitive variables were solved using a finite volume technique. The outflow region above the channel exit was included in the computational domain. While uniform velocity and temperature profiles were imposed at the inflow boundary of the computational domain, the natural condition was used at the outflow boundary. Results in the form of velocity and temperature profiles as well as flow structure downstream of the plate was presented for a range of Grashof numbers, Reynolds numbers, plate to fluid thermal conductivity and plate to channel width ratios, keeping the channel length to width ratio and the fluid Prandtl number fixed. It was shown that the velocity profiles within the channel are skewed substantially to the hot wall as  $Gr/Re$  increases and thermal conductivity ratio decreases. The interface temperatures both at the hot and cold surfaces of the plate were found to decrease with increasing  $Gr/Re$ .

### 1.4.3 Studies on Optimum Spacing

Determination of the optimum spacing between heated parallel plates is a fundamental problem in the thermal design of finned heat transfer surfaces and electronic packaging. This problem has received considerable attention in the past and promises to gain in importance in the foreseeable future mainly due to the increasing power densities in electronic components. Analytical, experimental and numerical studies on optimum spacing between a pair of heated parallel plates (single channel) and a series of heated parallel plates (multiple channels) dealing with different thermal configurations (symmetrical or asymmetrical, uniform wall temperature or uniform wall heat flux), modes of cooling (natural or forced convection) and varying treatments of inlet and exit conditions can be found in the literature. In this section, a comprehensive review of the literature on optimum spacing between heated

parallel plates is presented, classified as natural convection and forced convection investigations. There has been no investigation reported for the corresponding mixed convection problem.

### Natural Convection Investigations

The problem of optimum spacing between heated vertical parallel plates cooled by natural convection has been the subject of many investigations. The earliest and the most widely quoted experimental study of natural convection in a vertical channel is that of Elenbaas (1942). He considered symmetrically heated square plates subjected to uniform wall temperature conditions and recommended an expression for the optimum spacing for which the heat dissipation from the plate surfaces is maximum. Two decades later, the steady laminar natural convection between two vertical plates maintained at the same uniform temperature was first numerically investigated by Bodoia and Osterle (1962). Assuming uniform velocity and temperature profiles, and ambient pressure at the inlet of the channel, solutions of the boundary layer type governing equations were obtained using a finite difference scheme. From their numerical solutions these authors also derived a criterion for the optimum spacing based on maximum heat dissipation. Their overall heat transfer results and the optimum spacing criterion were in good agreement with the experimental observations of Elenbaas (1942).

Using a somewhat different approach, Levy (1971) analytically derived a criterion for optimum spacing between heated vertical parallel plates dissipating heat by natural convection to the ambient air. Consideration was given to symmetrically heated plates subjected to uniform wall temperatures. The criterion obtained was based on minimizing the temperature difference between the plate and the inlet air with respect to the inter-plate spacing. For a given average heat transfer rate the optimisation function was obtained by making a lumped system heat balance and using the Nusselt number correlation developed by Bodoia and Osterle (1962). He argued that for the condition of minimum temperature difference to occur, the boundary layers on the plates must not merge. In another study, Levy, et al (1975) experimentally verified the criterion for optimum spacing obtained by Levy (1971).

Bar-Cohen and Rohsenow (1984) proposed an analytic optimisation tech-



nique for predicting the optimum plate-to-plate spacing in an array of heated vertical parallel plates cooled by natural convection. Consideration was given to plates subjected to both uniform wall temperature and uniform wall heat flux conditions. Also, both symmetric and asymmetric heating conditions were considered. The authors derived a composite expression for the convective heat transfer coefficient by blending two asymptotes, one for the fully developed limit and the other for the single plate limit. An optimisation function was then obtained using a lumped system energy balance. Finally, optimum plate-to-plate spacing for each thermal configuration was obtained by maximizing the total heat dissipation per unit volume of the stack.

Anand et al. (1992) have numerically studied the optimum spacing for free convection between a pair of heated vertical parallel plates by solving boundary layer type equations using an implicit finite difference scheme. Considering symmetrically as well as asymmetrically heated plates for both uniform wall temperature and uniform heat flux heating conditions, the results were presented for asymmetric heating parameters ranging from 0 to 1 and Grashof numbers ranging from 10 to  $10^5$ . Like Bar-Cohen and Rohsenow (1984), the criterion used for the optimum spacing corresponds to the maximum average Nusselt number based on the channel height. However, the results of optimum spacing obtained by them were not in good agreement with those of Bar-Cohen and Rohsenow (1984). The differences between the two results was attributed to the differences in approach.

Recently, Morrone et al. (1997) addressed the problem of optimum inter-plate spacing associated with a single heated vertical parallel plate channel cooled by the upflow natural convection of air. The authors considered the plates to be symmetrically heated with a uniform heat flux. In contrast to Anand et al. (1992), the authors included the effect of momentum and energy diffusion outside of the channel by using the full elliptic conservation equations with an I-shaped enlarged computational domain consisting of the actual region between the plates and two relatively large domains placed upstream of the entrance and downstream of the channel exit. Following the stream function-vorticity formulation, the system of conservation equations were solved by a control volume based finite difference method. The results pertaining to optimum spacing and induced mass flow rate were obtained for air ( $Pr = 0.71$ ) and for a range of Grashof numbers between  $10^2$  and  $10^5$ . The authors also proposed correlations relating the induced mass flow rate and

the optimum plate spacing to the thermo-geometrical parameters involved in the study. They concluded that, for all  $Gr_H$ , the optimum spacing obtained by Anand et al. (1992) over-predicted their results with relative differences ranging from 12.6% at  $Gr_H = 10^2$  to 6% at  $Gr_H = 10^5$ .

Quite recently, Ledezma and Bejan (1997) have presented both numerical and experimental results pertaining to the geometric optimisation of an assembly of staggered vertical plates installed in a given volume and cooled by laminar natural convection. The plates were assumed to be symmetrically heated and maintained at a uniform temperature. With the computational domain extended both at the upstream and downstream sections, the coupled governing equations were solved by the Galerkin finite element method. Considering the maximization of the overall thermal conductance between the plates and the quiescent surrounding fluid as the basis of the optimum, results were reported for a wide range of geometric parameters such as the horizontal spacing between adjacent columns of plates and the number of plates mounted in each vertical column. With the Prandtl number kept constant at 0.72, the Rayleigh number based on the vertical dimension of the assembly was varied in the range  $10^3$  to  $10^6$ . The authors showed that overall thermal conductance has a distinct maximum with respect to inter-plate spacing and the optimum spacing decreases as the Rayleigh number increases. The authors also concluded that the arrangement with no stagger is the best.

### Forced Convection Investigations

Due to increasing technological demand on heat transfer enhancement, the problem of obtaining the optimum spacing between heated parallel plates cooled by forced convection has been studied extensively in the recent past. The first study dealing with the problem is that of Bejan and Sciubba (1992). Considering a stack of smooth and negligibly thin equal-spaced heat generating boards and using order of magnitude analysis the authors obtained correlations for optimum spacing between the boards such that the total heat transfer rate from the stack to the coolant is maximum. The imposed pressure difference across the stack was fixed and boards with two different thermal configurations were considered: with one surface either isothermal or with uniform heat flux, while the other surface was always taken as insulated. The accuracy of these correlations were assessed by an analysis of

the developing flow and heat transfer in each board-to-board channel. It was shown that the type of thermal boundary condition has only a minor effect on the optimal board-to-board spacing and the maximum heat transfer rate.

Bejan et al. (1993) addressed the fundamental thermal design problem associated with positioning of a heat generating board cooled by laminar forced convection in an insulated parallel plate channel so that the board operating temperature is minimum. Results were presented for both relatively good and bad thermal conductance of the board substrate. The optimum spacing between a heat generating board, maintained at either a uniform temperature or with uniform heat flux, and an insulated plate was reported. For a fixed rate of heat generation and also fixed spacing between the insulated parallel plates, the advantageous conditions of dividing a heat generating board into two or more equal-spaced boards inside the same channel were established.

Mereu et al. (1993) developed, both analytically and numerically, a series of correlations for estimating the optimum spacing of heat generating boards mounted in a stack cooled by single phase laminar forced convection. The authors took the board thickness into account in the calculation of the optimum board-to-board spacing and maximum heat transfer from the stack. Three different flow configurations were considered for the stack: with fixed pressure drop, fixed mass flow rate, and fixed pumping power. Theoretical results for optimum spacing and maximum overall thermal conductance between the stack and the coolant were validated by means of numerical simulations of the complete flow and temperature fields.

Morega and Bejan (1994) addressed the fundamental thermal design problem of optimum spacing between parallel heat generating boards mounted equidistantly in a stack of specified volume and cooled by laminar forced convection. The optimum board-to-board spacing based on the maximization of the overall thermal conductance between the stack and the coolant was obtained by simulating the complete flow and temperature field numerically in one of many identical channels. While one of the two surfaces of the channels was modelled as adiabatic, three different thermal configurations for the other surface were considered: with uniform heat flux, flush-mounted discrete heat sources, and protruding type discrete heat sources. Keeping the imposed pressure difference across the stack fixed, the results were presented for different board geometries and thermal configurations. Finally, the opti-

imum board-to-board spacing was correlated by a simple general expression that could apply to other packages with discrete heat sources.

Morega et al. (1995) investigated the optimum geometric arrangement of a stack of parallel plates under forced free stream flow conditions by numerically solving the flow and temperature fields. Considering uniform heat flux at the plates, the conservation equations of mass, momentum, and energy for steady, laminar, incompressible, two-dimensional flow of a Newtonian fluid were solved using a finite element software package. Optimum plate-to-plate spacing and the number of plates that could be installed in the fixed volume were obtained on the basis of minimizing the hot-spot temperature registered inside the stack. Choosing a stack with square cross-section and fixing the dimensionless plate thickness at 0.05, the numerical results were presented for  $Pr = 0.72$  and Reynolds numbers in the range of  $10^2$  to  $10^4$ . It was shown that the best way of positioning the plates relative to one another is by spacing them equidistantly, and that for a specified overall dimension of the stack, there is an optimal number of plates for which the hot-spot temperature is minimum. The authors also observed that as the Reynolds number increases, the hot-spot temperature and plate-to-plate spacing decrease.

Fowler et al. (1997) have studied, both experimentally and numerically, the geometric optimisation of staggered parallel plates in a fixed volume with forced convection. Given that the maximum temperature inside the volume is within a certain allowable level, the geometric optimisation was based on the maximization of the overall thermal conductance between the given volume and the given external flow. While the sole aim of the experimental study was to demonstrate the existence of an optimal spacing between two adjacent row of plates, the objective of the numerical study was to investigate the effect of four different geometric parameters — the spacing between the plates, the number of plates installed in one row, the plate swept length, and the degree to which the plates can be staggered — on the heat and fluid flow performance of the assembly. The numerical results were obtained for  $Pr = 0.72$  and a wide range of Reynolds numbers using a computational domain comprising an elemental channel with an upstream and a downstream section. These numerical results show the existence of an optimum spacing between two adjacent row of plates. It was observed that the optimum spacing decreases as Reynolds number increases and interestingly, that there is little benefit in dividing a fixed heat transfer area into smaller plates.

## 1.5 Objective of the Present Investigation

The literature review presented in Section 1.4.3 reveals that very few investigators to date have attempted to optimise the spacing between heated vertical parallel plates cooled by laminar free convection, while no study addressing the problem for mixed convection cooling has been reported so far. With the exception of Anand et al. (1992), Ledezma and Bejan (1997), and Morrone et al. (1997), most of the other investigators obtained the optimisation functions employing lumped system type heat balance with the natural heat transfer coefficient known *a priori*. Anand et al. (1992) numerically predicted the optimum plate-to-plate spacing for single channel by solving the boundary layer type of conservation equations in a computational domain that coincided with the actual physical domain between the plates. Therefore, momentum and energy diffusion that occur outside of the channel were excluded. Moreover, the authors assumed zero pressure defect at the inlet of the channel, which causes an over-prediction of the average Nusselt number, particularly for high Grashof number flows, as observed by Chappidi and Eno (1990).

Ledezma and Bejan (1997) focussed their attention on the volume constrained geometric optimisation of an assembly of staggered, heated vertical parallel plates cooled by natural convection. Morrone et al. (1997) were the first to include entrance and exit effects when studying the problem of optimum spacing between symmetrically heated vertical parallel plates cooled by laminar natural convection. However, they used only a uniform heat flux condition on the plates. While they solved the full elliptic Navier-Stokes and energy equations, and used upstream and downstream sections to more realistically resolve inflow and outflow boundary conditions at the inlet and exit of the channel, the applicability of their numerical simulations seems to be restricted to the single channel, and cannot be extended even to volume unconstrained optimisation of the inter-plate spacing of a series of heated vertical parallel plates, which is the common configuration in electronic cooling. Like Anand et al. (1992), the authors too have not attempted to optimise the spacing between a series of equal-spaced parallel plates stacked in a fixed volume.

From a historical point of view, the first investigation of natural convection flow through a series of heated vertical parallel plates are those of Kim et al. (1991) and Martin et al. (1991). Subsequently, Fujii et al. (1994), Floryan and Novak (1995), and Shahin and Floryan (1999) for natural convection and Waston et al. (1996) for mixed convection, numerically analysed the physics of heat and fluid flow for more or less similar thermo-geometric configurations. Among these, only Martin et al. (1991), Floryan and Novak (1995), and Shahin and Floryan (1999) solved the full elliptic conservation equations, including entrance effects. Their computational domain comprised the actual physical domain between the plates, together with a plenum upstream of the channel having a width equal to the inter-plate spacing. These investigations stressed the importance of the realistic elliptic model, and an extended computational domain, over the idealistic parabolic boundary-layer type equations. However, they left unexamined the aspects associated with the optimisation of the inter-plate spacing.

The primary objective of the present investigations is to numerically study the optimum plate-to-plate distance between an equal-spaced series of heated vertical thin parallel plates subjected to natural and mixed convection modes of cooling. It is assumed that the plates are symmetrically heated and maintained at a uniform temperature. The optimum spacing investigations for natural and mixed convection are presented as two separate case-studies. Emphasis is placed on volume unconstrained as well as volume constrained optimisation of inter-plate spacing. Accordingly, invoking the Boussinesq approximation, the steady state velocity and temperature fields are obtained by solving the pseudo-transient form of the full elliptic conservation equations in the stream function-vorticity formulation using the spectral element method as a solution strategy. The physical domain between a pair of thin plates combined with the upstream plenum, of width equal to the inter-plate spacing, is taken as the computational domain in order to more realistically resolve the inflow boundary conditions. So as to determine the optimum plate-to-plate spacing, for each case considered extensive numerical simulations are carried out for a Prandtl number of 0.70 and a wide range of aspect ratios, Grashof numbers, and buoyancy parameters (for mixed convection).

The mathematical formulations are presented in the next chapter. The spectral element method is elaborated upon in Chapter 3. The results are presented and discussed in Chapter 4. Chapter 5 summarises the major conclusions of the study, and ends with a discussion of the scope of future work.



# Chapter 2

## Mathematical Formulation

### 2.1 Introduction

Mathematical modelling is usually central to the analysis of engineering systems, which are often very complicated. For a typical thermo-fluids system, this complexity arises mainly due to the time-dependent, multidimensional nature of the fluid flow and heat transfer and the complex supplementary conditions that govern these systems. In addition, the non-linearity of the flow equations, the variation of thermophysical properties and, sometimes, the contribution of radiative heat transfer makes the analysis all the more complicated. Consequently, a real system is often simplified to a stylised model resembling the original in shape, geometry and other physical characteristics in the gross features, but not in every detail. Thus, by the application of fundamental physical laws, and by incorporating approximations and idealisations, a mathematical model representing the physical situation is obtained. Such a mathematical model is generally amenable to numerical simulations, which — hopefully, without involving exorbitant time and effort in computation. — give an adequate picture of the physics of the system.

In this chapter, the formulation of the problem of natural and mixed convective flows through a symmetrically heated vertical parallel-plate channel is presented, with the view of determining the optimum spacing between the plates. The approximations and idealisations made, and their validity, are discussed. The mathematical model in terms of both the primitive variables as well as stream-function and vorticity formulations are presented below for



the sake of completeness, although only the latter formulation is used in the numerical simulations. The use of the simulations results in determining the optimum spacing is discussed.

## 2.2 Physical Model

### 2.2.1 The Problem of Many Channels

Recall from the first chapter that the problem being analysed in this thesis concerns the optimum spacing of vertical plates (say, printed circuit boards [PCBs] in electronic equipment) in order to maximise heat-transfer. In other words, if we had a set of PCBs how would we space them so as to maximise the over-all heat transfer rate for a given volume?

To study such a general problem a number of idealisation have to be made. The immediate ones we assume are that

1. the vertical plates are identical
2. the (electronic) components actually dissipating the heat are small compared to the dimensions of the channel
3. the transverse dimension of the plates are large enough that the flow may be treated as two-dimensional(2-D).

Thus the problem actually analysed in this thesis is that of 2-D flow in a set of identical and parallel channels, in which the plates are treated as flat, and the electronic heating is replaced by a condition of uniform wall temperature.

As the channels are identical, there is no need to study more than one channel, for the effect of the others is obtained by the use of symmetry boundary conditions. Such an approach, of course, implicitly assumes that the number of plates are large, indeed infinite. But this assumption is justified by the very great difficulties that would be introduced were we to assume otherwise, and by the loss of generality that would also follow were we to assume any other specific case.

Thus, now we present the problem for a single channel, which is the basic component of our analysis. Knowing the heat transfer rate in this single channel, we merely multiply by the number of channels in a given space to obtain the total heat transfer rate in that space.

### 2.2.2 The Problem in a Single Channel

The geometric configuration and the co-ordinate system of the vertical parallel-plate channel is schematically depicted in Figure 2.1. The height of the channel is  $H$  and the spacing between the plates forming the channel is  $L$ . The thickness of the plates is taken as negligible compared to the inter-plate spacing. The origin of the co-ordinate system is affixed at the top of the left plate, with  $x$  as the downward vertical co-ordinate and  $y$  as the horizontal co-ordinate extending transversely across the channel. The force of gravity thus acts along the positive  $x$ -direction. The dimension of the channel normal to the  $x - y$  plane is taken as large in comparison with its other dimensions, so the flow is treated as two-dimensional. Both the plates of the channel are symmetrically heated and are maintained at a constant temperature,  $T_w$ , that is higher than the ambient temperature,  $T_\infty$ . The bottom and the top of the channel are exposed to the ambient air.

The temperature gradient resulting from the heating of air within the channel causes a density gradient, which in turn gives rise to buoyancy forces. In the absence of an externally imposed pressure difference, the flow is induced entirely by this buoyancy force. As a result, the heated air in the channel is continuously driven upward by buoyancy and is finally discharged into the ambient air through the upper end of the channel. Meanwhile, the air from below is drawn into the channel through the lower end by the pressure defect created by the lower density of hot air within the channel. When the flow is entirely due to the buoyancy effect, the heat transfer is due to *natural* or *free* convection. However, in the presence of a fan blowing air upwards into the channel, the flow in the channel may be both due to the forced flow and the buoyancy effect. In this case, it is called *mixed* convection. When the buoyancy effect is negligible compared to the forced flow, the flow condition is called *forced* convection.

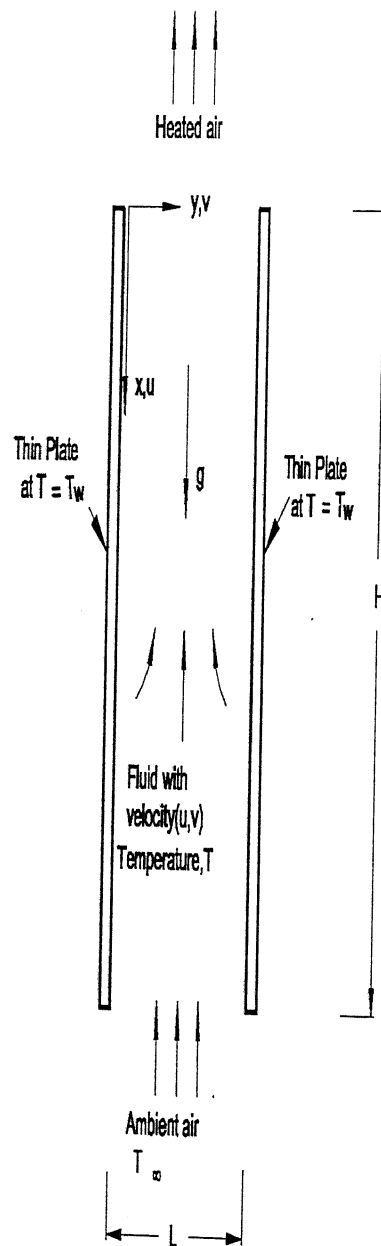


Figure 2.1: The Physical Model and the Coordinate System

## 2.3 Approximations and Idealisations

The physical model described in the preceding section is a simplified model, with respect to the surface geometry and heating condition of the parallel plates, when compared with a typical channel with electronic components actually encountered in applications. The further approximations and idealisations made for the present investigations are that:

1. The fluid is Newtonian, viscous, with constant thermo-physical properties.
2. The flow is steady, laminar and two-dimensional.
3. The Boussinesq approximation is valid.
4. Viscous dissipation and compression work are negligibly small.
5. Radiative heat transfer is insignificant.

### 2.3.1 Boussinesq Approximation

In most of the analytical as well as numerical studies of natural/mixed convective flows, the classical Boussinesq approximation is customarily invoked. This approximation has the advantage that it bypasses the calculation of the density field. While all other thermophysical properties of the fluid are assumed to remain constant, the density, associated with the buoyancy force, is assumed to vary linearly with temperature as per the following relation:

$$\rho_\infty = \rho[1 + \beta(T - T_\infty)] \quad (2.1)$$

where  $\beta$  is the coefficient of volumetric expansion at constant pressure,  $T_\infty$  is the temperature of the ambient fluid and  $\rho_\infty$  is the corresponding density.

The use of the Boussinesq approximation is only valid when the overall temperature difference within the physical domain is sufficiently small. Zhong et al. (1985) performed a quantitative assessment of this requirement for natural convection in a differentially heated square cavity. They concluded that when the non-dimensional temperature difference,  $\delta \equiv \left( \frac{T_w - T_\infty}{T_\infty} \right)$ ,

is less than 0.1, the Boussinesq approximation yields an accurate prediction of the flow and thermal fields. They also suggested that reasonably accurate values of average heat transfer rates could be obtained by using the Boussinesq approximation for  $\delta$  values up to 0.2.

With these limits of validity, the Boussinesq approximation is probably valid for many applications of electronic cooling. Typically, in most modern electronic equipment, the maximum temperature rise should not exceed  $50^\circ$  K. Therefore, for flow through channels of circuit boards, the overall temperature difference, for an ambient temperature  $T_\infty \cong 300$  K,  $\delta$  will be within 0.2. Most investigators in their studies of natural convection between vertical parallel-plates have invoked the Boussinesq approximation.

## 2.4 Mathematical Model

A mathematical model comprises quantitative statements of the relationships among the dependent and independent variables and the relevant parameters that describe some physical phenomena (Middleman, 1998). Typically, a mathematical model consists of equations that govern the behaviour of the physical system, and the associated boundary conditions.

Employing the approximations and the idealisations listed in Section 2.3, the physical model described in Section 2.2 is simulated by an equivalent mathematical model involving the conservation of mass, momentum, and energy, with appropriate boundary conditions. The mathematical model comprising these partial differential equations, along with their boundary conditions, is presented in the following sections.

### 2.4.1 Governing Equations

The governing equations describing buoyancy-driven flows and transport have been reviewed by Jaluria (1980), Gebhart et al. (1988) and Bejan (1995). For the steady, laminar, two-dimensional natural/mixed convective flows of a Newtonian fluid, using the Boussinesq approximation, the governing equations of mass, momentum and energy conservation are (Ledezma

and Bejan, 1997):

mass:

$$\frac{\partial u}{\partial x} + \frac{\partial v}{\partial y} = 0 \quad (2.2)$$

$x$ -momentum:

$$u \frac{\partial u}{\partial x} + v \frac{\partial u}{\partial y} = -\frac{1}{\rho} \frac{\partial p}{\partial x} + \nu \left( \frac{\partial^2 u}{\partial x^2} + \frac{\partial^2 u}{\partial y^2} \right) - g\beta(T - T_\infty) \quad (2.3)$$

$y$ -momentum:

$$u \frac{\partial v}{\partial x} + v \frac{\partial v}{\partial y} = -\frac{1}{\rho} \frac{\partial p}{\partial y} + \nu \left( \frac{\partial^2 v}{\partial x^2} + \frac{\partial^2 v}{\partial y^2} \right) \quad (2.4)$$

energy:

$$u \frac{\partial T}{\partial x} + v \frac{\partial T}{\partial y} = \alpha \left( \frac{\partial^2 T}{\partial x^2} + \frac{\partial^2 T}{\partial y^2} \right) \quad (2.5)$$

where  $(u, v)$  are the velocity components in the  $x$  and  $y$  directions, and  $\rho$  and  $T$  are the density and temperature, while  $\nu$  and  $\alpha$  are the kinematic viscosity and thermal diffusivity of the fluid. The quantity  $p$  is the *modified* pressure ( $= p_{thermodynamic} - \rho_\infty g x$ ) which accounts for the hydrostatic pressure, so that its value at the far field is always constant ( $p_\infty$ ), independent of  $x$ . It is to be noted that the gravitational acceleration,  $g$ , acts in the  $x$  direction, in our chosen convention.

The model equations (2.2) to (2.5) form a set of coupled partial differential equations that are elliptic in nature and require that boundary conditions to be imposed all around the domain boundary.

### 2.4.2 Boundary Conditions

The mathematical formulation of the problem is incomplete without prescribing a specific number of appropriate boundary conditions that allow only unique solutions of the governing equations to exist. The specification of mathematically correct boundary conditions that ensure the uniqueness of

the solution, while being compatible with the physics at the boundaries, is not always straightforward. In this section, the computational domain and the corresponding boundary conditions to be specified for the primitive variables formulation of the physical model described in Section 2.2 are discussed.

Before arriving at the boundary conditions at various boundaries, we have to first identify the solution/computational domain of the problem. The physical domain and the corresponding computational domain of the problem usually differ in one respect or the other. While the computational domain largely depends on the geometry of the physical domain, it may be extended beyond it to facilitate the specification of physically and mathematically correct boundary conditions.

Figure 2.2 depicts the computational domain pertaining to natural/mixed convective flows through a symmetrically heated parallel plate channel showing all the boundaries of interest. It consists of two impermeable and ‘no-slip’ solid boundaries represented by the lines AB and EF and four ‘free’, i.e., open, boundaries represented by dotted lines BC, CD, DE and AF. While the open boundaries CD and AF pertain to inflow and outflow respectively, the open boundaries BC and DE correspond to planes of symmetry which exist in the plenum upstream of the channel due to presence of neighbouring plates, as in the case of a series of parallel plate channels. Recall that the solution domain is symmetrical about these axes with regards to both heat and fluid flow. Therefore, the axes of symmetry may be used as boundaries.

Note that the computational domain has been extended downwards to include the plenum upstream of the channel. This has been done mainly to impose realistic inflow conditions. The extended domain has the same width as the channel — which appears to be appropriate for natural/mixed convection flows through a series of parallel plate channels. A similar approach was adopted by Martin et al. (1991) and Floryan and Novak (1995), and more recently by Shahin and Floryan (1999) in their study of natural convection through vertical plates. In contrast to this, Kettleborough (1972), Naylor et al. (1991) and, more recently, Morrone et al. (1997) have taken an enlarged domain near the inlet of the channel which seems to be more appropriate for prescribing the inflow boundary conditions for a single parallel plate channel. The appropriate height of the extended region was determined by numerical experimentation, in this study, to be 10% of the channel height. Extending

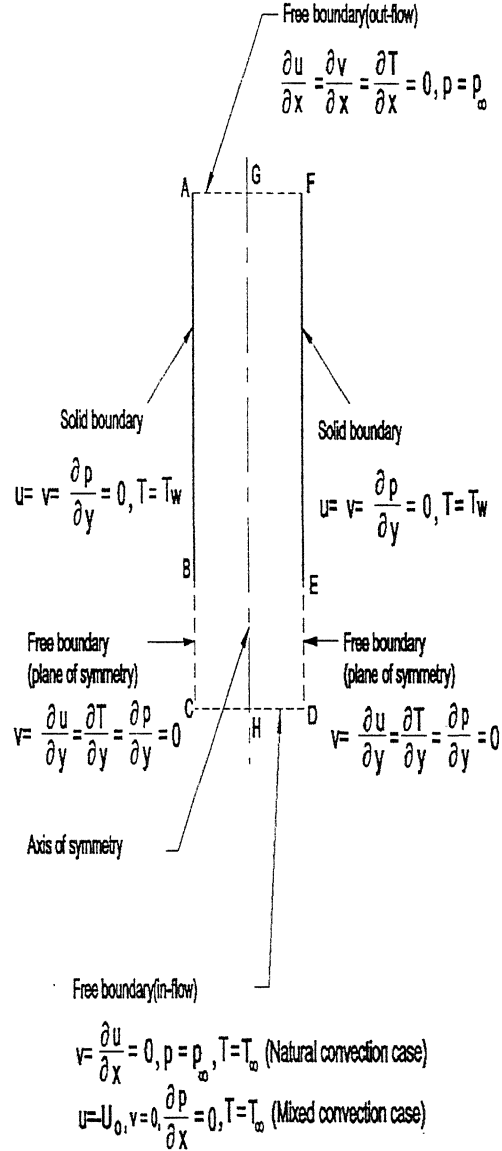


Figure 2.2: The Computational Domain and Boundary Conditions



the region beyond this figure does not have any further affect on the flow physics, for the chosen boundary conditions. The downstream region beyond the exit end of the channel has been excluded from the solution domain mainly due to computational economy and simplicity.

The velocity and temperature boundary conditions at the inflow and outflow boundaries are not obvious. The literature reveals that researchers have resorted to various idealised conditions on these boundaries. As seen below, the boundary conditions on all except the inflow boundary are the same for both natural and mixed convective flows. The inflow boundary conditions, however, differ with the type of flow.

Since the solid boundaries AB and EF represent the impermeable, no-slip and isothermal walls of the parallel plate channel, the components of velocity are set to zero and the temperature is fixed at  $T_w$  at these boundaries. The normal gradient of pressure at the solid boundary is assumed to be zero, in keeping with boundary layer theory.

The boundaries BC and DE correspond to lines of symmetry. As the flow across a symmetry line is zero, the component of velocity normal to the boundary is set to zero. Also, due to symmetry, the shear stress and the normal gradient of temperature and pressure on these boundaries are taken to be zero. At the outflow boundary, AF, the two components of velocity and the temperature are not known. Therefore, the flow is assumed to be fully-developed here and the normal gradients of the components of velocity and the temperature are taken to be zero. The pressure at the outflow boundary is taken equal to that of ambient fluid. Although these outflow conditions, which could affect the computed flow in the channel, are somewhat adhoc, they are similar to the idealisations made by previous researchers.

The conditions on the inflow boundary CD are specified differently depending on the type of flow. For natural convection flows, the  $v$  component of velocity and the normal gradient of the  $u$  component of velocity are set to zero. The flow is assumed to enter the inflow boundary at ambient temperature and pressure. For mixed convective flows, the fluid is assumed to cross the inflow boundary at ambient temperature and with  $v=0$ , but the  $u$  component of velocity is taken to be  $u = -U_0$  (recall  $u$  is positive downwards, in our convention). The normal gradient of pressure is assumed to be zero.

### An Alternate Computational Domain

Figure 2.3 illustrates an alternate computational domain along with the appropriate boundary conditions. Note that the computational domain shown in Figure 2.3 is exactly a symmetric one-half of the solution domain shown in Figure 2.2. Here the fact that the flow domain is perfectly symmetrical has been used to reduce the computational domain — and the computations needed for solutions— by one-half. By symmetry, the y-derivatives of  $u$ ,  $v$ , and  $T$ , and the y-component of velocity ( $v$ ) at the physical centre-line, shown here as the GH boundary, will be zero. This fact is used to prescribe the boundary conditions shown in the figure.

However, a danger inherent in the use of symmetry conditions is that symmetry may be violated by the flow, even if the domain is symmetric. This generally occurs when the flow becomes unsteady, as happens at high Grashof numbers. The unsteady flow-field generally is not symmetric. Too many symmetry boundary conditions and the use of a steady-state solver may thus result in pseudo steady-state solutions in cases when the flow should have physically become unsteady. This possibility can be guarded against by (a) doing simulations on the full physical domain, and (b) using a pseudo transient algorithm that would alert us about the onset of unsteadiness. Thus the computations in this thesis were done with a pseudo-transient method (see below), and the computational domain used was the full one shown in Figure 2.2 rather than the truncated one in Figure 2.3.

## 2.5 Dimensionless Representation

The mathematical model is generally cast in dimensionless form, and the flow variables are normalised so that their values are of the order of unity. The nondimensionalisation reduces the number of independent parameters and gives rise to non-dimensional parameters of physical significance such as the Reynolds number, Grashof number and Prandtl number, etc. which can be varied independently to characterise the results.

The nondimensionalisation of the governing equations and the corre-

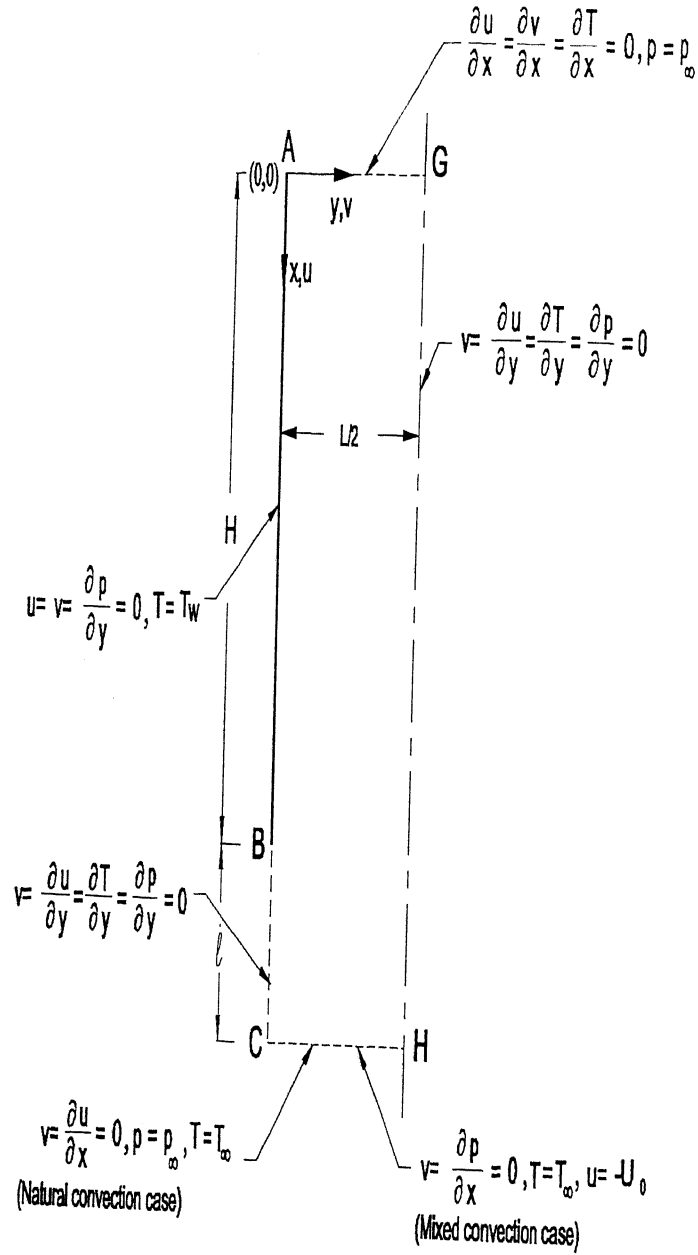


Figure 2.3: An alternate computational domain and boundary conditions

sponding boundary conditions is achieved by introducing dimensionless independent and dependent variables. The definition of these dimensionless variables are based on a choice of a characteristic dimension and other characteristic quantities that depend on the geometry of the physical domain and the physical flow and heat transfer properties of the fluid. There is a freedom to select these quantities, and the proper nondimensionlisation is problem dependent. There may be many possible non-dimensional forms, of which some may be more natural and sensible than the others. In this section, the dimensionless variables, the dimensionless governing equations and the dimensionless boundary conditions, both for natural and mixed convection flows, are presented.

### 2.5.1 Dimensionless Variables

The nondimensionlisation of the governing equations and the boundary conditions is done here by introducing dimensionless variables defined as follows:

$$\begin{aligned} X &= \frac{x}{H} & Y &= \frac{y}{H} \\ U &= \frac{u}{U_c} & V &= \frac{v}{U_c} \\ \theta &= \frac{T - T_\infty}{T_w - T_\infty} & P &= \frac{p_\infty - p}{\rho U_c^2} \end{aligned}$$

where the characteristic velocity,  $U_c$  is given for natural convection flows by

$$U_c = [g\beta H(T_w - T_\infty)]^{\frac{1}{2}}, \quad (2.6)$$

and for mixed convection flow by

$$U_c = U_0, \quad (2.7)$$

where  $U_0$  is the uniform inflow velocity.

In the definition of dimensionless variables presented above, the height of the channel,  $H$ , is employed as the characteristic length dimension,  $(T_w - T_\infty)$

as the characteristic temperature difference and  $\rho U_c^2$  is the characteristic pressure. The nondimensional velocities are differently interpreted for natural and mixed convection according to the different definitions of characteristic velocity given in equations (2.6) and (2.7).

### 2.5.2 Dimensionless Governing Equations

With these dimensionless variables, the dimensionless equations of mass, momentum and energy transport for natural convection and mixed convection can be written separately as follows:

Natural Convection:

mass:

$$U \frac{\partial U}{\partial X} + V \frac{\partial V}{\partial Y} = 0, \quad (2.8)$$

X-momentum:

$$U \frac{\partial U}{\partial X} + V \frac{\partial U}{\partial Y} = \frac{\partial P}{\partial X} + \frac{1}{\sqrt{Gr_H}} \left[ \frac{\partial^2 U}{\partial X^2} + \frac{\partial^2 U}{\partial Y^2} \right] - \theta \quad (2.9)$$

Y-momentum:

$$U \frac{\partial V}{\partial X} + V \frac{\partial V}{\partial Y} = \frac{\partial P}{\partial Y} + \frac{1}{\sqrt{Gr_H}} \left[ \frac{\partial^2 V}{\partial X^2} + \frac{\partial^2 V}{\partial Y^2} \right] \quad (2.10)$$

energy:

$$U \frac{\partial \theta}{\partial X} + V \frac{\partial \theta}{\partial Y} = \frac{1}{Pr \sqrt{Gr_H}} \left[ \frac{\partial^2 \theta}{\partial X^2} + \frac{\partial^2 \theta}{\partial Y^2} \right] \quad (2.11)$$

where  $Gr_H$  and  $Pr$  are the Grashof number and Prandtl number, respectively, given by

$$Gr_H \equiv \frac{g \beta (T_W - T_\infty) H^3}{\nu^2} \quad (2.12)$$

and

$$Pr \equiv \frac{\nu}{\alpha} \quad (2.13)$$

The corresponding equations for mixed convection are :  
mass:

$$\frac{\partial U}{\partial X} + \frac{\partial V}{\partial Y} = 0 \quad (2.14)$$

X-momentum:

$$U \frac{\partial U}{\partial X} + V \frac{\partial U}{\partial Y} = \frac{\partial P}{\partial X} + \frac{1}{Re_H} \left[ \frac{\partial^2 U}{\partial X^2} + \frac{\partial^2 U}{\partial Y^2} \right] - \frac{Gr_H}{Re_H^2} \theta \quad (2.15)$$

Y-momentum:

$$U \frac{\partial V}{\partial X} + V \frac{\partial V}{\partial Y} = \frac{\partial P}{\partial Y} + \frac{1}{Re_H} \left[ \frac{\partial^2 V}{\partial X^2} + \frac{\partial^2 V}{\partial Y^2} \right] \quad (2.16)$$

energy:

$$U \frac{\partial \theta}{\partial X} + V \frac{\partial \theta}{\partial Y} = \frac{1}{Pr Re_H} \left[ \frac{\partial^2 \theta}{\partial X^2} + \frac{\partial^2 \theta}{\partial Y^2} \right] \quad (2.17)$$

where  $Re_H$  is the Reynolds number given by

$$Re_H \equiv \frac{U_0 H}{\nu} \quad (2.18)$$

The dimensionless equations are seemingly different for natural and mixed convection flows. However, although the nondimensionalisation has changed the appearance of the equations, the fundamental governing equations are the same in both cases. It is merely more appropriate to use different nondimensionalisation for the natural and mixed convection cases, because of the different physics involved.

### 2.5.3 Dimensionless Boundary Conditions

If the aspect ratio of the channel and the dimensionless length of the extended domain are, respectively, defined by

$$A_r \equiv \frac{H}{L} \quad (2.19)$$

and

$$\epsilon_l \equiv \frac{l}{H} \quad (2.20)$$

the dimensionless boundary conditions can be expressed as follows:

$$\text{at } X = 0, \quad 0 < Y < \frac{1}{A_r} : \quad \frac{\partial U}{\partial X} = 0, \frac{\partial V}{\partial X} = 0, \frac{\partial \theta}{\partial X} = 0, P = 0$$

$$\text{at } Y = 0, \frac{1}{A_r} \leq X \leq 1 : \quad U = 0, V = 0, \theta = 1, \frac{\partial P}{\partial Y} = 0$$

$$\text{at } Y = 0, \frac{1}{A_r} < X \leq 1 + \epsilon_l : \quad \frac{\partial U}{\partial Y} = 0, V = 0, \frac{\partial \theta}{\partial Y} = 0, \frac{\partial P}{\partial Y} = 0$$

$$\begin{aligned} \text{at } X = 1 + \epsilon_l, \quad 0 < Y < \frac{1}{A_r} : \\ \frac{\partial U}{\partial X} = 0, V = 0, \theta = 0, P = 0 \quad \text{for natural convection} \\ U = -1, V = 0, \theta = 0, \frac{\partial P}{\partial Y} = 0 \quad \text{for mixed convection} \end{aligned}$$

## 2.6 Stream Function-Vorticity Formulation

The dimensionless governing equations in the primitive variables for two-dimensional flows have two components of velocity, the pressure and the temperature as dependent variables. For incompressible flows, it is a crucial fact that there is no *direct* equation for the pressure — the pressure is merely a link between the continuity and momentum equations. Primitive variable solution procedures usually employ the continuity equation as a constraint to derive the correct pressure field through a cumbersome iterative method. Keeping this in view, the present problem has been formulated using the stream-function vorticity approach, which is presented below.

The stream function-vorticity formulation is a commonly used approach for the numerical simulation of steady two-dimensional or axisymmetric incompressible flows. This formulation has the advantage that it eliminates

the pressure from the governing equations, and the stream function automatically satisfies the continuity equation. Thus, this method has the advantage of dealing with only two equations, while the primitive variable formulation requires that the continuity equation also be solved along with two momentum equations.

In addition, Dirichlet conditions are often given for the stream function, instead of the Neumann conditions generally needed for the pressure. On the other hand, there is no direct boundary condition for surface vorticity, which has to be specified in terms of the stream function field. The accuracy of the overall solution critically depends on how this boundary condition is handled. In the rest of this section, the stream function - vorticity formulation is presented along with the boundary conditions.

### 2.6.1 Vorticity Transport and Stream Function Equations

The vorticity transport and stream function equations can be obtained by introducing the dimensionless stream function,  $\Psi$ , and vorticity,  $\Omega$ , in terms of their dimensional forms  $\psi$  and  $\omega$ :

$$\Psi = \frac{\psi}{U_c H} \qquad \Omega = \frac{\omega H}{U_c}$$

These can be related to the non-dimensional velocity field by:

$$U = \frac{\partial \Psi}{\partial Y}; \quad V = -\frac{\partial \Psi}{\partial X} \qquad (2.21)$$

and

$$\Omega = \frac{\partial V}{\partial X} - \frac{\partial U}{\partial Y} \qquad (2.22)$$

We can readily see that Equation (2.21) satisfies the continuity equation (2.8) and (2.14). Thus, if we substitute the dependent  $U, V$  variables with the stream function we need not be concerned with the continuity equation



anymore. Invoking equations (2.21) into (2.22) we obtain a Poisson equation for the stream function as

$$\frac{\partial^2 \Psi}{\partial X^2} + \frac{\partial^2 \Psi}{\partial Y^2} = -\Omega \quad (2.23)$$

This equation is applicable irrespective of type of flow (natural, mixed or forced).

By differentiating the X and Y momentum equations, (2.9) and (2.10) with respect to Y and X, respectively, subtracting the resulting equations from each other and rearranging, we obtain the vorticity transport equation for natural convective flows as

$$U \frac{\partial \Omega}{\partial X} + V \frac{\partial \Omega}{\partial Y} = \frac{1}{\sqrt{Gr_H}} \left( \frac{\partial^2 \Omega}{\partial X^2} + \frac{\partial^2 \Omega}{\partial Y^2} \right) + \frac{\partial \theta}{\partial Y} \quad (2.24)$$

Similarly, the vorticity transport equation for mixed convective flows can be obtained as

$$U \frac{\partial \Omega}{\partial X} + V \frac{\partial \Omega}{\partial Y} = \frac{1}{Re_H} \left( \frac{\partial^2 \Omega}{\partial X^2} + \frac{\partial^2 \Omega}{\partial Y^2} \right) + \frac{Gr_H}{Re_H^2} \frac{\partial \theta}{\partial Y} \quad (2.25)$$

### 2.6.2 The Pseudo-Transient Forms

Instead of directly solving the stream function, vorticity and energy equations (2.23, 2.24 or 2.25, and 2.11 or 2.17), we solve the pseudo-transient forms of these equations as a solution strategy. The stream-function equation is written in the Cauchy-Kowaleska form :

$$\frac{\partial \Psi}{\partial \tau} = \frac{\partial^2 \Psi}{\partial X^2} + \frac{\partial^2 \Psi}{\partial Y^2} + \Omega \quad (2.26)$$

which is solved along with the following equations:

for natural convective flow:

$$\frac{\partial \Omega}{\partial \tau} + \frac{\partial U \Omega}{\partial X} + \frac{\partial V \Omega}{\partial Y} = \frac{1}{\sqrt{Gr_H}} \left[ \frac{\partial^2 \Omega}{\partial X^2} + \frac{\partial^2 \Omega}{\partial Y^2} \right] + \frac{\partial \theta}{\partial Y} \quad (2.27)$$

$$\frac{\partial \theta}{\partial \tau} + \frac{\partial U \theta}{\partial X} + \frac{\partial V \theta}{\partial Y} = \frac{1}{Pr \sqrt{Gr_H}} \left( \frac{\partial^2 \theta}{\partial X^2} + \frac{\partial^2 \theta}{\partial Y^2} \right) \quad (2.28)$$

or, for mixed convective flows:

$$\frac{\partial \Omega}{\partial \tau} + \frac{\partial U \Omega}{\partial X} + \frac{\partial V \Omega}{\partial Y} = \frac{1}{Re_H} \left[ \frac{\partial^2 \Omega}{\partial X^2} + \frac{\partial^2 \Omega}{\partial Y^2} \right] + \frac{Gr_H}{Re_H^2} \frac{\partial \theta}{\partial Y} \quad (2.29)$$

$$\frac{\partial \theta}{\partial \tau} + \frac{\partial U \theta}{\partial X} + \frac{\partial V \theta}{\partial Y} = \frac{1}{Re_H Pr} \left[ \frac{\partial^2 \theta}{\partial X^2} + \frac{\partial^2 \theta}{\partial Y^2} \right] \quad (2.30)$$

Note that the governing equations have now been put in the conservative form. In these equations  $\tau$  is a pseudo-time-like variable. The equations are solved to obtain ‘unsteady’ solutions which converge to the final steady-state. The transient terms involving  $\tau$  reduce to zero at the steady state, leaving solutions of the original steady-state equations. The use of these pseudo-transient forms of the equations allows us to obtain the steady state solutions easily and naturally by time-stepping from arbitrary initial conditions. Other iterative methods may be more efficient in obtaining the steady state solution, but would probably be more uncertain, given that three coupled partial differential equations are involved. Furthermore, tailoring these other iterative schemes to the special, full-matrix, spectral element formulation is likely to prove cumbersome.

### 2.6.3 Boundary Conditions

The vorticity transport and the stream function equations require boundary conditions to be specified on all the boundaries of the solution domain. The boundary conditions for the primitive variables formulation have already been discussed in Section 2.4.2. In this section, the boundary conditions for

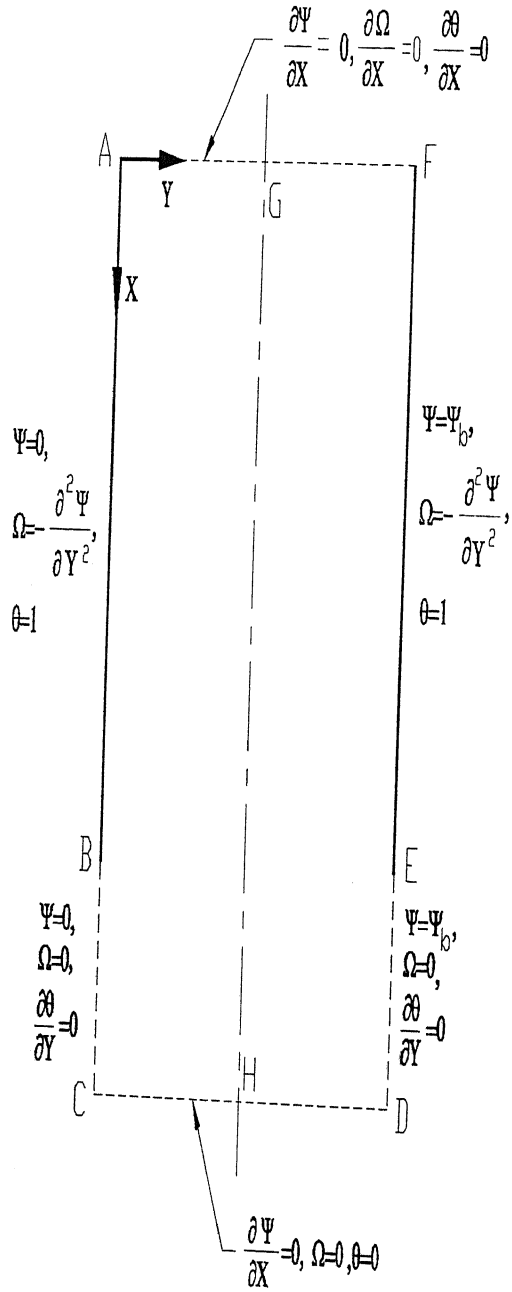


Figure 2.4: Boundary conditions for the Vorticity & Stream-function formulation

the stream function and vorticity are presented. Figure 2.4 depicts the computational domain, with the boundary conditions used.

The impermeability condition at the wall AB implies that there is no fluid flow across this boundary and that the solid boundary itself can be considered a stream line. Obviously, the stream function  $\Psi$  is constant along this boundary, and as *one* value of the stream-function can be assigned arbitrarily,  $\Psi = 0$  is conveniently specified along this boundary. It also follows that on this boundary  $\frac{\partial^2 \Psi}{\partial X^2} = 0$ . This can be used to obtain the boundary condition of vorticity (see, e.g., Comini et al., 1997) by substituting into Equation (2.23) to get  $\Omega = -\frac{\partial^2 \Psi}{\partial Y^2}$  at the solid boundary AB. A similar boundary condition for vorticity is used on the other wall EF.

The boundary EF corresponds to a solid boundary and, therefore, the stream function is constant along this boundary due to the reason already mentioned above. Therefore, a general condition  $\Psi = \Psi_b$  is specified along this boundary. The value of  $\Psi_b$  is intimately related to the upward volume flow rate per unit depth,  $\dot{v}$ , in the channel which is equal to the difference  $\Delta\Psi (= 0 - \Psi_b)$  between the stream function values at the two plates. For mixed convection flows, the volume flow rate is *imposed* and known, and the value of  $\Psi_b$  can be specified in advance. However, for natural convection flows, the volume flow rate is *induced* and not known *a priori*, and  $\Psi_b$  has to be determined iteratively as part of the numerical solution procedure.

The symmetry across BC allows no flow to cross this boundary which, therefore, is a stream line. It is clear from Figure 2.4 that the stream lines corresponding to boundaries AB and BC are the same. Thus, the value of the stream function along the boundary BC is also specified as zero. The value of the vorticity  $\Omega$  is equal to zero on this boundary because of symmetry. The symmetry boundary DE is similar to BC except that the stream function value is  $\Psi_b$ , the same as on EF.

At the inlet boundary CD, the flow is assumed to enter at the ambient temperature ( $\theta=0$ ) and with zero vorticity, as the flow is as yet away from the walls which create vorticity. The stream-function boundary condition is obtained by assuming that the inflow is vertical (i.e.,  $V=0$ ), yielding the

Neumann condition  $\frac{\partial \Psi}{\partial X} = 0$  along this boundary.

At the outflow boundary AF it is again assumed that the flow is vertical, so  $\frac{\partial \Psi}{\partial X} = 0$ . It is also assumed that the flow is fully-developed and the normal gradient of the temperature and vorticity are thus taken as zero. These boundary conditions frequently appear in the literature. Even though fully developed flow may not be achieved at the exit of the channel, the zero gradient boundary conditions generally allow the flow distribution to be obtained quite accurately (Huang and Vafai 1994).

To implement the vorticity boundary condition at the solid walls we do the following. Using a Taylor series expansion of the stream function  $\Psi$  on the solid boundary and incorporating the additional condition  $\frac{\partial \Psi}{\partial Y} = 0$ , the vorticity at the solid boundary is evaluated by

$$\Omega_w = -\frac{2(\Psi_{nb} - \Psi_w)}{\Delta Y^2} \quad \text{at } Y = 0, 1$$

where  $\Delta Y$  is the grid spacing at the solid boundary. The stream function value at the wall  $\Psi_w$  is 0 or  $\Psi_b$ , on the left and right walls, respectively, and  $\Psi_{nb}$  is the value at the corresponding neighbouring interior point.

### Mass Flow for Natural Convection

As mentioned above, the volume flow rate, hence  $\Psi_b$ , in natural convective flows is not known in advance, and needs to emerge as part of the solution. This can be done by ensuring that the momentum change along the vertical channel is exactly balanced by the combined viscous shear forces at the walls and the buoyancy forces on the fluid in the channel. A straight-forward application of the integral momentum equation at the inlet and outlet of the channel yields the following equation for the pressure drop:

$$\begin{aligned} \Delta P_{av} = & \left[ \int_0^{\frac{1}{Ar}} U^2 \big|_{X=1+\epsilon_l} dY - \int_0^{\frac{1}{Ar}} U^2 \big|_{X=0} dY \right] + \left[ \int_0^{1+\epsilon_l} \int_0^{\frac{1}{Ar}} \theta dX dY \right] \\ & + \frac{1}{\sqrt{Gr_H}} \left[ \int_0^{1+\epsilon_l} \frac{\partial U}{\partial Y} \big|_{Y=0} dX - \int_0^{1+\epsilon_l} \frac{\partial U}{\partial Y} \big|_{Y=\frac{1}{Ar}} dX \right] \end{aligned} \quad (2.31)$$

where  $\Delta P_{av}$  is the difference of the average pressure at the inflow and outflow boundaries, which should be zero for natural convection.

The flow rate, and hence  $\Psi_b$ , clearly depends on the Grashof number,  $Gr_H$ , and the aspect ratio,  $A_r$ , through an unknown relation. For the correct value of  $\Psi_b$ , buoyancy and shear forces will be exactly balanced by the momentum change in the channel, and  $\Delta P_{av}$  will be zero. In the iterative procedure for natural convection, the value of  $\Psi_b$  is guessed and the steady state solution is obtained. By using the steady state solution in Equation (2.31) it is determined from if  $\Delta P_{av} = 0$ . If not,  $\Psi_b$  is changed accordingly and a new steady state solution is obtained, and so on till  $\Delta P_{av} = 0$  (to six decimal places).

It is clear that the natural convection case is very computer-intensive, as it involves obtaining many steady state solutions for each case, while mixed convection requires only one solution for each case.

## 2.7 Criteria for Optimum Spacing

In this section, the use of the numerical solutions in obtaining the optimal spacing (for maximum heat transfer) for the multi-channel problem discussed in Section 2.2.1 is elaborated upon.

For multiple channels formed by symmetrically heated equal-spaced parallel plates maintained at the same constant temperature, the flow and heat transfer characteristics of each channel would be the same. Therefore, it is sufficient to analyse only one channel to obtain results pertinent to a series of identical vertical parallel-plate channels. From the numerical solution of the problem depicted in Figure 2.4, whether for natural or for mixed convection, we obtain the steady state velocity and temperature fields in the solution domain. From the temperature field we can obtain the heat transfer from the plates in the following way.

We define the heat transfer coefficient at the walls with reference to the temperature difference ( $T_w - T_\infty$ ). The local heat transfer coefficient is defined as:

$$h \equiv \frac{q_w}{(T_w - T_\infty)}. \quad (2.32)$$

where the local heat flux at the wall,  $q_w$ , can be obtained from the temperature field by

$$q_w = -k \left( \frac{\partial T}{\partial y} \right)_w, \quad (2.33)$$

where  $k$  is the thermal conductivity of the fluid.

By non-dimensionalising this equation, we obtain

$$q_w = -k \frac{(T_w - T_\infty)}{H} \left( \frac{\partial \theta}{\partial Y} \right)_w \quad (2.34)$$

from which the local wall Nusselt number,

$$Nu \equiv \frac{hH}{k} = - \left( \frac{\partial \theta}{\partial Y} \right)_w \quad (2.35)$$

can be obtained, using the numerical solution for  $\theta$ .

The average wall Nusselt number can then be obtained as

$$Nu_{av} = \frac{1}{H} \int_0^H Nu \, dx = \int_0^1 Nu \, dX, \quad (2.36)$$

which can again be evaluated from the numerical solution. The total heat transfer (per unit depth) can then be obtained by

$$Q_w \equiv h_{av} H (T_w - T_\infty) = k Nu_{av} (T_w - T_\infty). \quad (2.37)$$

where  $h_{av}$  is the average heat transfer coefficient.

When there are multiple channels, the number of such channels that can be fitted into a span  $W$  is  $\frac{W}{L}$ . We thus see that the total heat transfer in that span will be

$$Q_{total} = 2 Q_w \frac{W}{L} = 2 Nu_{av} A_r \frac{Wk}{H} (T_w - T_\infty) \quad (2.38)$$

where  $A_r$  ( $\equiv H/L$ ) is the aspect ratio of each channel, and the factor of 2. arises because there are two heat transfer surfaces per channel.

We now see that, for fixed  $W$ ,  $H$ ,  $(T_w - T_\infty)$ , and  $k$ ,

$$Q_{total} \propto Nu_{av} A_r \quad (2.39)$$

which provides us the objective function ( $=Nu_{av} A_r$ ) for our optimisation problem of finding the maximum heat transfer for the case of multiple channels.

Thus, for fixed Grashof number  $Gr_H$  (for natural convection) or fixed  $Gr_H$  and  $Re_H$  (for mixed convection), the numerical solutions are computed for a variety of aspect ratios to determine the value of  $A_r$  that yields the maximum value of  $Nu_{av} A_r$ . This aspect ratio is then taken to correspond to the optimum spacing between the plates, for the multiple channel case. In contrast, for the single channel case the optimum  $A_r$  is simply the one that gives the highest  $Nu_{av}$ , which also maximises the heat-transfer for that single channel. The interpretation of the numerical results is thus quite simple.





# Chapter 3

## Numerical Formulation

### 3.1 Introduction

The fundamental laws of fluid flow and heat transfer are expressed as a set of coupled, non-linear partial differential equations, often with complex initial and boundary conditions. In most situations, analytical solutions of these equations either do not exist or are mathematically complex in form. As a consequence, one generally resorts to numerical solutions using a suitable discretization method. The discretization methods that are most commonly used are the finite difference method, the finite element method, and, more recently, the spectral method.

In the present thesis, the numerical solutions of the governing equations are obtained by the spectral element method of Patera (1984) implemented on the stream-function vorticity formulation by Prakash (1995). The spectral element method is basically a synthesis of the spectral and the finite element methods (Korczak and Patera, 1986). In this method of discretization, the computational domain is decomposed into a number of elements, and within each element the dependent variable is represented as a high-order Lagrangian interpolant in terms of Chebyshev polynomials, the coefficients of which are related to the function values at the Gauss-Lobatto Chebyshev collocation points. The governing equations are partially discretized using a finite difference scheme for the time derivative term leading to a second-order elliptic Helmholtz equation. While the convection and the source terms are

treated explicitly, the diffusion terms are treated implicitly. The Helmholtz equation is further discretized by spectral element method, using the variational principle, resulting in a system of linear algebraic equations. These systems of equations is efficiently solved by the LU decomposition method.

In this chapter, the discretization of a typical computational domain, and the temporal and spatial discretization of the conservative form of the governing equations are presented. The formation of elemental and global equations and the implementation of boundary condition are described in detail. The solution method of the system of algebraic equations and other relevant computational details are provided.

## 3.2 Discretization of the Domain

The first step towards the numerical solution of the mathematical model is to discretize the computational domain. In the spectral element method, the computational domain is divided into a number of rectangular elements spanning the  $X$  and  $Y$  directions. Each element of the computational domain is further subdivided into a set of grid points. Figure 3.1 illustrates a nominal 4-element discretized computational domain. Figure 3.2(a) depicts the typical  $i^{th}$  element of the computational domain showing  $(X, Y)$  coordinates of its corner points.

For the sake of convenience in using Chebyshev interpolating functions, a local coordinate system applicable to each individual element is introduced. Consequently, each rectangular element in the global coordinates  $(X, Y)$  is mapped onto a square element in the local coordinates  $(\bar{x}, \bar{y})$  spanning -1 to +1 in the  $\bar{x}$  and  $\bar{y}$  directions, as shown in Figure 3.2b. Thus, the local  $i^{th}$  element coordinate system in terms of global coordinates system can be defined as

$$\bar{x}^i = \frac{2}{L_x^i}(X - a_x^i) - 1 \quad (3.1)$$

$$\bar{y}^i = \frac{2}{L_y^i}(Y - a_y^i) - 1 \quad (3.2)$$

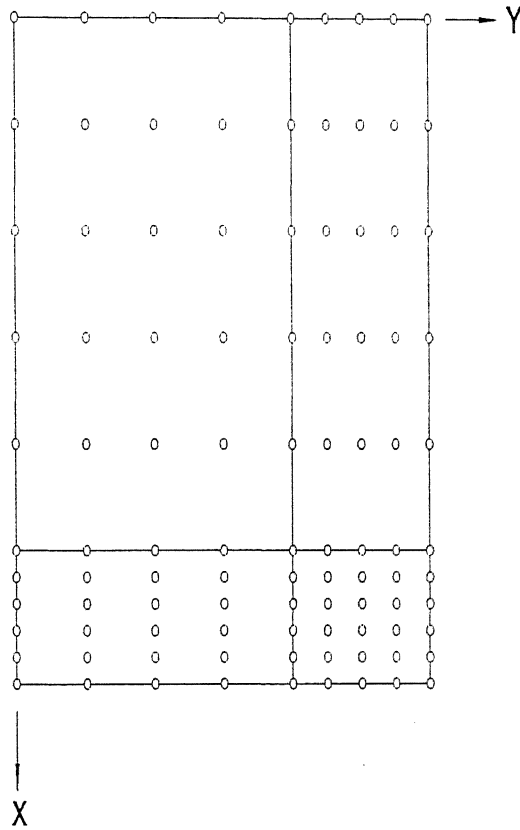


Figure 3.1: A nominal discretized computational domain

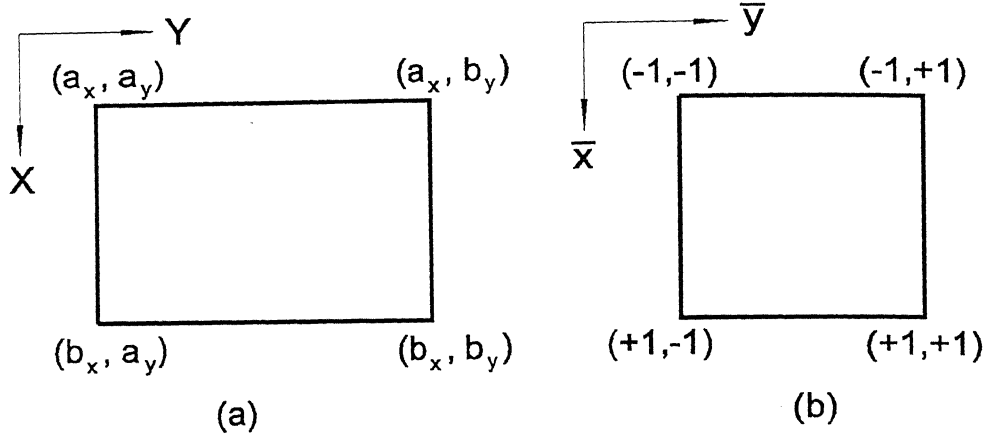


Figure 3.2: A typical element in (a) the original coordinates, and (b) transformed local coordinates.

where  $(a_x^i, a_y^i)$  and  $(b_x^i, b_y^i)$  are the coordinates of the top left and the bottom right corners of the element, and  $L_x^i (= b_x^i - a_x^i)$  and  $L_y^i (= b_y^i - a_y^i)$  are the lengths of the element in the  $X$  and  $Y$  directions respectively. It is to be noted that the global coordinates  $(X, Y)$  used in the mathematical formulation of the problem can be easily retrieved from the local elemental coordinate just by inverting the linear transformation given by equations (3.1) and (3.2).

Figure 3.3 shows the  $i^{th}$  element in the local coordinate system  $(\bar{x}, \bar{y})$  having  $N_x^i + 1$  and  $N_y^i + 1$  number of grid points in  $\bar{x}$  and  $\bar{y}$  directions, respectively. The position of any grid point within the element is identified by a set of two indices, say  $(j, k)$ , the top left corner of the  $i^{th}$  element being  $(0, 0)$ , and the bottom right corner  $(N_x^i, N_y^i)$ . The local coordinates  $(\bar{x}_j^i, \bar{y}_k^i)$  of the  $(j, k)$  grid point are generated by the Gauss-Lobatto Chebyshev formula as follows:

$$\bar{x}_j^i = \cos\left(\frac{\pi j}{N_x^i}\right) \quad j = 0, 1, 2, \dots, N_x^i \quad (3.3)$$

$$\bar{y}_k^i = \cos\left(\frac{\pi k}{N_y^i}\right) \quad k = 0, 1, 2, \dots, N_y^i \quad (3.4)$$

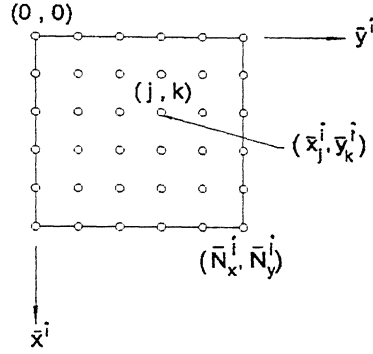


Figure 3.3: The grid-points and local two-index numbering in a typical element.

### 3.2.1 Grid Point Numbering

#### Local Numbering

For the sake of convenience in writing the discretized elemental equations in the conventional matrix form, the grid points identified by two indices, say  $(j, k)$ , are also specified by a single index, say  $p$ , using the transformation given by

$$p = (N_y + 1) \cdot j + k \quad j = 0, 1, \dots, N_x, \quad k = 0, 1, \dots, N_y \quad (3.5)$$

where,  $N_x+1$  and  $N_y+1$  are the number of grid points in X and Y directions respectively.

Figure 3.4a illustrates a typical element of the computational domain having 4 grid points in the X direction and 5 grid points in the Y direction: in this figure, every grid point is identified by two indices, i.e.,  $(j, k)$ . Beginning from  $(0, 0)$  at the top left corner, the successive neighbouring grid point is marked by incrementing either  $j$  or  $k$  by 1 in accordance with its location

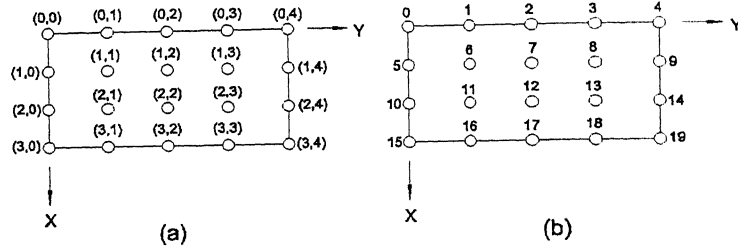


Figure 3.4: The (a) two-index and (b) one-index local numbering of grid-points in a typical element.

with respect to its neighbour. The corresponding single index numbering of the grid points at element level is shown in Figure 3.4b. Starting from 0 at the top left corner of the element, the grid points at the element level are numbered in serial order along the  $Y$  direction by advancing line by line in the  $X$  direction.

### Global Numbering

The numbering systems above are *local* to each element, as every element will have the same set of numbers  $[(0, 0), \dots, (N_x, N_y)]$  or  $0, 1, \dots, (N_x + 1)(N_y + 1) - 1$  describing its grid-points. Apart from the local two- and one-index numbering, the domain also has a global numbering system in which each grid point has a unique number across all elements. This facilitates the formation of a global equation set by combining the elemental equations. Thus every grid point has two numbering systems associated with it. The local numbering corresponds to its position within an element, and the global numbering to its position in the computational domain as a whole.

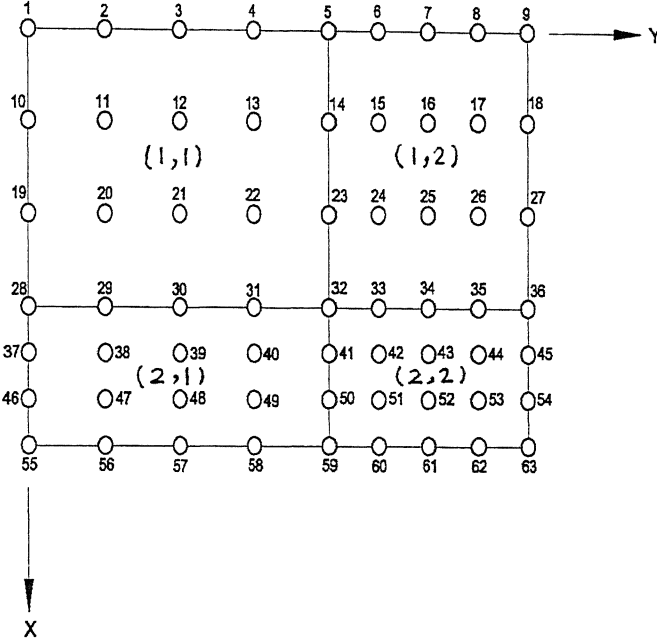


Figure 3.5: The global numbering of grid points in the computational domain.

Figure 3.5 depicts the global grid point numbering system of the computational domain consisting of 2 elements in the  $X$  direction and 2 elements in the  $Y$  direction. Each element of the computational domain is assumed to have 4 grid points in the  $X$  direction and 5 grid points in the  $Y$  direction. The elements are identified by two indices, say  $(i_e, j_e)$ , marked at the centre of each element and the grid points by single global number. Starting from 1 at the top left corner of the computational domain, the grid points at the global level are numbered serially along the  $Y$  direction by advancing line by line along the  $X$  direction.



### 3.3 Discretization of Governing Equations

Now that we have discretized the computational domain, the next step involves the equation discretization which approximates the governing differential equation by a system of linear/nonlinear algebraic equations in variables defined at the grid points of the computational domain. For transient/pseudo-transient problems, the equation discretization involves two components, the temporal discretization and the spatial discretization. In the succeeding two subsections the temporal and spatial discretization of the conservative form of the governing equations are presented.

#### 3.3.1 Temporal Discretization

In the spectral element method, the temporal derivative term is generally treated by a finite difference scheme. Both explicit as well as implicit schemes have been exploited in a variety of heat and fluid flow situations. The major disadvantage of the explicit schemes is the restriction imposed on the maximum time step by the numerical stability criterion. In contrast, the implicit schemes are usually free from these restrictions and, therefore, allow relatively larger time steps as compared to explicit schemes. However, with regards to the number of arithmetic operations required per time step, the implicit schemes are typically more expensive. Implicit formulations also often have greater algorithmic complexity.

Although, explicit schemes are only conditionally stable, this is not always bad. In fact, the standard stability criterion for explicit schemes applied to convective equations, the CFL (Courant-Friedrichs-Lewy) condition, conveys a clear physical meaning. It states that the time step should not be greater than the time taken for any fluid particle to cover a distance equal to one grid interval. It is observed that even for implicit schemes that are unconditionally stable the accuracy of numerical solution deteriorates if the CFL condition is not satisfied. Obviously, it is always safer to satisfy the CFL condition for strongly convective flows and, therefore, it is unnecessary to implement complex implicit schemes for the convective terms. On the contrary, for the diffusion terms it is usually more efficient to implement implicit schemes because of their better stability properties.

In situations when both convection and diffusion terms are present, it is often the practice to use an explicit representation for the convective terms and an implicit representation for the diffusion terms. For example, in the Adams-Bashforth-Crank-Nicolson scheme, the convective terms are treated by the explicit Adams-Bashforth scheme and the diffusion terms by the implicit Crank-Nicolson scheme. Both of these schemes are second order accurate, and the overall scheme also possesses second order accuracy in time. However, it is only conditionally stable as well as algorithmically involved.

Patera (1984) and Koczak and Patera (1986) adapted the Adams-Bashforth-Crank-Nicolson scheme for a spectral element temporal discretization. In their formulation, the implicit representation for the diffusion term is the keystone of the method — as it allows the basic governing equations to be expressed in terms of a Helmholtz equation which can be solved using the variational principle. Their scheme is second order accurate in time but is exponentially accurate in space because of its spectral spatial discretization.

In the present thesis, the pseudo-transient forms of the governing equations are discretized in time by treating the diffusion term implicitly and remaining terms explicitly. Although, the temporal discretization used is only first order accurate, this does not affect the steady state solution of the problems in which we are actually interested. The time discretized form of the general transport equation

$$\frac{\partial \phi}{\partial t} + \Lambda \left( \frac{\partial \phi U}{\partial X} + \frac{\partial \phi V}{\partial Y} \right) = \Gamma \left( \frac{\partial^2 \phi}{\partial X^2} + \frac{\partial^2 \phi}{\partial Y^2} \right) + S_\phi$$

is given by:

$$\frac{\phi^{n+1} - \phi^n}{\Delta \tau} + \Lambda \left[ \frac{\partial \phi U}{\partial X} + \frac{\partial \phi V}{\partial Y} \right]^n = \Gamma \left[ \frac{\partial^2 \phi}{\partial X^2} + \frac{\partial^2 \phi}{\partial Y^2} \right]^{n+1} + S_\phi^n \quad (3.6)$$

Equation (3.6) can be rearranged to obtain the following form:

$$\left( \frac{\partial^2 \phi}{\partial X^2} \right)^{n+1} + \left( \frac{\partial^2 \phi}{\partial Y^2} \right)^{n+1} - \frac{\phi^{n+1}}{\Gamma \Delta \tau} = -\frac{\phi^n}{\Gamma \Delta \tau} + \frac{\Lambda}{\Gamma} \left[ \frac{\partial \phi U}{\partial X} + \frac{\partial \phi V}{\partial Y} \right]^n - \frac{S_\phi^n}{\Gamma} \quad (3.7)$$

or

$$\phi_{XX} + \phi_{YY} - \lambda^2 \phi = f \quad (3.8)$$

Equation (3.8) is the well-known Helmholtz equation. The function  $\phi$  is the unknown to be computed and  $f$  is the known forcing function. In equation (3.6) and (3.7), the superscript  $n$  refers to the known values at current time  $\tau$ , and  $n+1$  to the unknown values at time  $\tau + \Delta\tau$ . The parameter  $\lambda^2 (\equiv \frac{1}{\Gamma \Delta\tau})$  can take different positive values. In the limiting case when  $\lambda^2 \rightarrow 0$ , equation (3.8) reduces to the Poisson equation which too can be solved using the Helmholtz solver.

### 3.3.2 Spatial Discretization

In the spectral element method, the solution of the Helmholtz equation is based on the variational formulation requiring the minimization of a corresponding functional.

### 3.3.3 Variational Formulation

The functional corresponding to the Helmholtz equation [Equation 3.8] satisfying homogeneous Neumann boundary conditions can be obtained as

$$I = \iint \left[ -\frac{1}{2} \{ (\phi_X)^2 + (\phi_Y)^2 \} - \frac{\lambda^2}{2} \phi^2 - \phi f \right] dX dY \quad (3.9)$$

where the integration spans over the entire computational domain.

When the computational domain is decomposed into  $M$  rectangular elements, the functional  $I$  can be simply expressed as the sum of the functional of the individual elements, ie.,

$$I = \sum_{i=1}^M I^i \quad (3.10)$$

where  $I^i$  is the functional corresponding to  $i^{th}$  element and can be expressed as

$$I^i = \int \int \left[ -\frac{1}{2} \{ (\phi_X^i)^2 + (\phi_Y^i)^2 \} - \frac{\lambda^2}{2} (\phi^i)^2 - \phi^i f^i \right] dX dY \quad (3.11)$$

the integration spanning over the area of the  $i^{th}$  element, defined as the rectangle between  $[a_x^i, a_y^i]$  and  $[b_x^i, b_y^i]$ .

If there are  $(N_x^i + 1)(N_y^i + 1)$  Gauss-Lobatto Chebyshev grid points within the  $i^{th}$  element, the dependent variable  $\phi(X, Y)$  and the forcing function,  $f(X, Y)$ , can be expressed as Lagrangian interpolants in Chebyshev polynomials of the local coordinates,  $-1 \leq \bar{x}^i, \bar{y}^i \leq +1$ , as

$$\phi^i(\bar{x}^i, \bar{y}^i) = \sum_{j=0}^{N_x^i} \sum_{k=0}^{N_y^i} \phi_{jk}^i h_j^i(\bar{x}^i) h_k^i(\bar{y}^i) \quad (3.12)$$

and

$$f^i(\bar{x}^i, \bar{y}^i) = \sum_{j=0}^{N_x^i} \sum_{k=0}^{N_y^i} f_{jk}^i h_j^i(\bar{x}^i) h_k^i(\bar{y}^i) \quad (3.13)$$

where  $\phi_{jk}^i$  and  $f_{jk}^i$  are the values of  $\phi$  and  $f$  at the grid point  $(\bar{x}_j^i, \bar{y}_k^i)$  respectively. The interpolation functions  $h_j^i(\bar{x}^i)$  and  $h_k^i(\bar{y}^i)$  are  $N_x^i - th$  and  $N_y^i - th$  order local Lagrangian interpolants satisfying

$$h_j^i(\bar{x}_l^i) = \delta_{jl} \quad (3.14)$$

and

$$h_k^i(\bar{y}_m^i) = \delta_{km} \quad (3.15)$$

at the local grid points within the  $i^{th}$  element, where  $\delta_{jl}$  and  $\delta_{km}$  are the Kronecker delta functions,  $\bar{x}_l^i$  is the coordinate of  $l$ th grid point in the  $\bar{x}^i$ -direction and  $\bar{y}_m^i$  is the coordinate of the  $m$ th grid point in the  $\bar{y}^i$ -direction.

The interpolation functions  $h_j^i(\bar{x}^i)$  and  $h_k^i(\bar{y}^i)$  can be expressed in terms of Chebyshev polynomials as

or

$$\phi_{XX} + \phi_{YY} - \lambda^2 \phi = f \quad (3.8)$$

Equation (3.8) is the well-known Helmholtz equation. The function  $\phi$  is the unknown to be computed and  $f$  is the known forcing function. In equation (3.6) and (3.7), the superscript  $n$  refers to the known values at current time  $\tau$ , and  $n+1$  to the unknown values at time  $\tau + \Delta\tau$ . The parameter  $\lambda^2 (\equiv \frac{1}{\Gamma \Delta\tau})$  can take different positive values. In the limiting case when  $\lambda^2 \rightarrow 0$ , equation (3.8) reduces to the Poisson equation which too can be solved using the Helmholtz solver.

### 3.3.2 Spatial Discretization

In the spectral element method, the solution of the Helmholtz equation is based on the variational formulation requiring the minimization of a corresponding functional.

### 3.3.3 Variational Formulation

The functional corresponding to the Helmholtz equation [Equation 3.8] satisfying homogeneous Neumann boundary conditions can be obtained as

$$I = \iint \left[ -\frac{1}{2} \{ (\phi_X)^2 + (\phi_Y)^2 \} - \frac{\lambda^2}{2} \phi^2 - \phi f \right] dX dY \quad (3.9)$$

where the integration spans over the entire computational domain.

When the computational domain is decomposed into  $M$  rectangular elements, the functional  $I$  can be simply expressed as the sum of the functional of the individual elements, ie.,

$$I = \sum_{i=1}^M I^i \quad (3.10)$$

where  $I^i$  is the functional corresponding to  $i^{th}$  element and can be expressed as

$$I^i = \int \int \left[ -\frac{1}{2} \{ (\phi_X^i)^2 + (\phi_Y^i)^2 \} - \frac{\lambda^2}{2} (\phi^i)^2 - \phi^i f^i \right] dX dY \quad (3.11)$$

the integration spanning over the area of the  $i^{th}$  element, defined as the rectangle between  $[a_x^i, a_y^i]$  and  $[b_x^i, b_y^i]$ .

If there are  $(N_x^i + 1)$   $(N_y^i + 1)$  Gauss-Lobatto Chebyshev grid points within the  $i^{th}$  element, the dependent variable  $\phi(X, Y)$  and the forcing function,  $f(X, Y)$ , can be expressed as Lagrangian interpolants in Chebyshev polynomials of the local coordinates,  $-1 \leq \bar{x}^i, \bar{y}^i \leq +1$ , as

$$\phi^i(\bar{x}^i, \bar{y}^i) = \sum_{j=0}^{N_x^i} \sum_{k=0}^{N_y^i} \phi_{jk}^i h_j^i(\bar{x}^i) h_k^i(\bar{y}^i) \quad (3.12)$$

and

$$f^i(\bar{x}^i, \bar{y}^i) = \sum_{j=0}^{N_x^i} \sum_{k=0}^{N_y^i} f_{jk}^i h_j^i(\bar{x}^i) h_k^i(\bar{y}^i) \quad (3.13)$$

where  $\phi_{jk}^i$  and  $f_{jk}^i$  are the values of  $\phi$  and  $f$  at the grid point  $(\bar{x}_j^i, \bar{y}_k^i)$  respectively. The interpolation functions  $h_j^i(\bar{x}^i)$  and  $h_k^i(\bar{y}^i)$  are  $N_x^i - th$  and  $N_y^i - th$  order local Lagrangian interpolants satisfying

$$h_j^i(\bar{x}_l^i) = \delta_{jl} \quad (3.14)$$

and

$$h_k^i(\bar{y}_m^i) = \delta_{km} \quad (3.15)$$

at the local grid points within the  $i^{th}$  element, where  $\delta_{jl}$  and  $\delta_{km}$  are the Kronecker delta functions,  $\bar{x}_l^i$  is the coordinate of  $l$ th grid point in the  $\bar{x}^i$ -direction and  $\bar{y}_m^i$  is the coordinate of the  $m$ th grid point in the  $\bar{y}^i$ -direction.

The interpolation functions  $h_j^i(\bar{x}^i)$  and  $h_k^i(\bar{y}^i)$  can be expressed in terms of Chebyshev polynomials as

$$h_j^i(\bar{x}^i) = \frac{2}{N_x^i} \sum_{n=0}^{N_x^i} \frac{1}{\bar{C}_j \bar{C}_n} T_n(\bar{x}_j^i) T_n(\bar{x}^i) \quad (3.16)$$

and

$$h_k^i(\bar{y}^i) = \frac{2}{N_y^i} \sum_{m=0}^{N_y^i} \frac{1}{\bar{C}_k \bar{C}_m} T_m(\bar{y}_k^i) T_m(\bar{y}^i) \quad (3.17)$$

where  $T_n$  are the  $n^{th}$  order Chebyshev polynomials given by

$$T_n(\bar{x}^i) = \cos(n \cos^{-1} \bar{x}^i) \quad (3.18)$$

Using Equation (3.3),

$$T_n(\bar{x}_j^i) = \cos\left(\frac{\pi n j}{N_x^i}\right) \quad (3.19)$$

and

$$T_m(\bar{y}_k^i) = \cos\left(\frac{\pi m k}{N_y^i}\right) \quad (3.20)$$

The  $\bar{C}$ 's in equations (3.16) and (3.17) are the integer functions given by

$$\bar{C}_j = 1, \quad \text{for } j \neq 0 \quad \text{or } N_x^i \quad (3.21)$$

$$= 2, \quad \text{for } j = 0 \quad \text{or } N_x^i \quad (3.22)$$

and

$$\bar{C}_k = 1, \quad \text{for } k \neq 0 \quad \text{or } N_y^i \quad (3.23)$$

$$= 2, \quad \text{for } k = 0 \quad \text{or } N_y^i \quad (3.24)$$

Now, the equations (3.12) and (3.13) can be rewritten as

$$\phi^i(\bar{x}^i, \bar{y}^i) = \frac{4}{N_x^i N_y^i} \sum_{j=0}^{N_x^i} \sum_{k=0}^{N_y^i} \sum_{n=0}^{N_x^i} \sum_{m=0}^{N_y^i} \phi_{jk}^i \frac{1}{\bar{C}_j \bar{C}_n \bar{C}_k \bar{C}_m} T_n(\bar{x}_j^i) T_n(\bar{x}^i) T_m(\bar{y}_k^i) T_m(\bar{y}^i) \quad (3.25)$$

and

$$f^i(\bar{x}^i, \bar{y}^i) = \frac{4}{N_x^i N_y^i} \sum_{j=0}^{N_x^i} \sum_{k=0}^{N_y^i} \sum_{n=0}^{N_x^i} \sum_{m=0}^{N_y^i} f_{jk}^i \frac{1}{\bar{C}_j \bar{C}_n \bar{C}_k \bar{C}_m} T_n(\bar{x}_j^i) T_m(\bar{x}^i) T_m(\bar{y}_k^i) T_m(\bar{y}^i) \quad (3.26)$$

As the physical rectangular elements are mapped into square elements using the linear transformation given by equations (3.1) and (3.2), the differentiation or integration performed in the transformed coordinates  $(\bar{x}^i, \bar{y}^i)$  must be properly scaled. As a result, the corresponding derivatives in the two coordinate systems are related by

$$\frac{\partial \phi}{\partial X} = \frac{2}{L_x^i} \frac{\partial \phi}{\partial \bar{x}^i} \quad (3.27)$$

and

$$\frac{\partial \phi}{\partial Y} = \frac{2}{L_y^i} \frac{\partial \phi}{\partial \bar{y}^i} \quad (3.28)$$

where,  $\frac{2}{L_x^i}$  and  $\frac{2}{L_y^i}$  are the scale factors. Therefore, the derivative terms consisting of  $\phi_X^i$  and  $\phi_Y^i$  in equation (3.11) can be easily obtained as

$$\phi_X^i = \frac{2}{L_x^i} \frac{4}{N_x^i N_y^i} \sum_{j=0}^{N_x^i} \sum_{k=0}^{N_y^i} \sum_{n=0}^{N_x^i} \sum_{m=0}^{N_y^i} \phi_{jk}^i \frac{1}{\bar{C}_j \bar{C}_n \bar{C}_k \bar{C}_m} T_n(\bar{x}_j^i) T_m(\bar{y}_k^i) \frac{dT_n(\bar{x}^i)}{d\bar{x}^i} T_m(\bar{y}^i) \quad (3.29)$$

and

$$\phi_Y^i = \frac{2}{L_y^i} \frac{4}{N_x^i N_y^i} \sum_{j=0}^{N_x^i} \sum_{k=0}^{N_y^i} \sum_{n=0}^{N_x^i} \sum_{m=0}^{N_y^i} \phi_{jk}^i \frac{1}{\bar{C}_j \bar{C}_n \bar{C}_k \bar{C}_m} T_n(\bar{x}_j^i) T_m(\bar{y}_k^i) T_n(\bar{x}^i) \frac{dT_m(\bar{y}^i)}{d\bar{y}^i} \quad (3.30)$$



### 3.3.4 Formation of Elemental Equations

The elemental algebraic system of equations are obtained by minimizing the functional given by equation (3.11) which requires that the variation of  $I^i$  with respect to the nodal values  $\phi_{jk}^i$  vanish, i.e.,

$$\frac{\delta I^i}{\delta \phi_{jk}^i} = 0 \quad (3.31)$$

At this point, it is important to note that it follows from Equation (3.25) and the following two discrete orthogonality properties of Chebyshev polynomials on a Gauss-Labatto grid:

$$\frac{2}{N_x^i} \sum_{n=0}^{N_x^i} T_n(\bar{x}_j^i) T_n(\bar{x}_p^i) = \bar{C}_n \bar{C}_j \delta_{pj}$$

and

$$\frac{2}{N_y^i} \sum_{m=0}^{N_y^i} T_m(\bar{y}_k^i) T_m(\bar{y}_q^i) = \bar{C}_m \bar{C}_k \delta_{qk},$$

that

$$\frac{\partial}{\partial \phi_{jk}^i} (\phi_{pq}^i) = \delta_{pj} \delta_{qk} \quad (3.32)$$

Inserting the  $\phi^i$  and  $f^i$  from Equations (3.25) and (3.26) and the derivatives  $\phi_X^i$  and  $\phi_Y^i$  from Equations (3.29) and (3.30) into the functional given by Equation (3.11), performing the resulting integrals and finally applying the Equations (3.31) and (3.32), the elemental algebraic system of equations will simply be (henceforth the Einsteinian repeated index convection will be used):

$$C_{jklm}^i \phi_{lm}^i = e_{jk}^i \quad (3.33)$$

where,

$$e_{jk}^i = B_{jklm}^i f_{lm}^i \quad (3.34)$$

$$C_{jklm}^i = A_{jklm}^i - \lambda^2 B_{jklm}^i \quad (3.35)$$

Here,

$$A_{jklm}^i = -\frac{L_y^i}{L_x^i} \frac{1}{(N_x^i N_y^i)^2} \tilde{A}_{jl}^x \tilde{B}_{km}^y - \frac{L_x^i}{L_y^i} \frac{1}{(N_x^i N_y^i)^2} \tilde{A}_{km}^y \tilde{B}_{jl}^x \quad (3.36)$$

$$B_{jklm}^i = \frac{L_x^i L_y^i}{4} \frac{1}{(N_x^i N_y^i)^2} \tilde{B}_{jl}^x \tilde{B}_{km}^y \quad (3.37)$$

$$\tilde{A}_{jl}^x = \frac{4}{\bar{C}_j \bar{C}_l} \sum_{n=0}^{N_x^i} \sum_{m=0}^{N_y^i} \frac{1}{\bar{C}_n \bar{C}_m} T_n(\bar{x}_j^i) T_m(\bar{x}_l^i) a_{nm} \quad (3.38)$$

$$\tilde{B}_{jl}^x = \frac{4}{\bar{C}_j \bar{C}_l} \sum_{n=0}^{N_x^i} \sum_{m=0}^{N_y^i} \frac{1}{\bar{C}_n \bar{C}_m} T_n(\bar{x}_j^i) T_m(\bar{x}_l^i) b_{nm} \quad (3.39)$$

and

$$\begin{aligned} a_{nm} &= \int_{-1}^1 \frac{dT_n}{d\bar{x}^i} \frac{dT_m}{d\bar{x}^i} d\bar{x}^i \\ &= 0, & n+m & \text{ odd} \\ &= \frac{nm}{2} [J_{|(n-m)/2|} - J_{|(n+m)/2|}], & n+m & \text{ even} \end{aligned} \quad (3.40)$$

where,

$$\begin{aligned} J_k &= -4 \sum_{p=1}^k \frac{1}{2p-1}, & k &\geq 1 \\ &= 0, & k &= 0 \end{aligned} \quad (3.41)$$

and

$$\begin{aligned} b_{nm} &= \int_{-1}^1 T_n T_m d\bar{x}^i \\ &= 0, & n+m & \text{ odd} \\ &= \frac{1}{1-(n+m)^2} + \frac{1}{1-(n-m)^2}, & n+m & \text{ even} \end{aligned} \quad (3.42)$$

Note that the matrices  $\tilde{A}_{jl}^x$  and  $\tilde{B}_{jl}^x$  are independent of the elemental length  $L_x^i, L_y^i$  and are the same for all the elements, which have the same  $N_x^i$  and  $N_y^i$ . Thus, these universal matrices  $\tilde{A}_{jl}^x$  and  $\tilde{B}_{jl}^x$  can be computed first and then the individual elemental matrices  $A_{jklm}^i$  and  $B_{jklm}^i$  can be computed for every individual element.

Equation (3.33), with four-dimensional arrays B and C, is not convenient for direct numerical solution. Consequently, this elemental equation is transformed into more conventional form by combining the two indices  $j$  and  $k$  to give a single index  $p$ , as in Equation (3.5). Similarly, the other two indices  $l$  and  $m$  are combined to give another single index  $q$ . As a result, the equation (3.33) is transformed to conventional matrix form given by

$$C_{pq}^i \phi_q^i = B_{pq}^i f_q^i \quad (\equiv e_p^i) \quad (3.43)$$

For the element having  $(N_x+1)(N_y+1)$  grid points, the coefficient matrix [C] will be of the order of  $(N_x+1)(N_y+1) \times (N_x+1)(N_y+1)$ .

### 3.3.5 Formation of Global Equations

In the preceding section, we obtained the system of discrete equations for each element. Once the elemental equations for all the elements of the computational domain are obtained, these are combined to form the global system of equations by adding the stiffness contributions corresponding to common boundary nodes of the adjoining elements. The formation of global matrix,  $[C^{global}]$ , from elemental matrices, [C], and right side global vector,  $\{e^{global}\}$ , from elemental vectors,  $\{e\}$ , are accomplished as follows:

For every grid point that lies exclusively within an element, the coefficient of the elemental matrix [C] in a locally numbered row and column are transferred to the corresponding globally numbered row and column in the global matrix  $[C^{global}]$  as it is. On the other hand, the coefficient of the global matrix corresponding to a grid point at an elemental interface is obtained by adding the elemental coefficients corresponding to that grid point from all the elemental sets in which it appears. However, in doing so, the correspondence between the local and global number of the grid point in the computational domain is maintained. The same procedure is adopted for the formation of

global right side vector,  $\{e^{global}\}$ , from the elemental vectors,  $\{e\}$ .

The total number of grid points in the computational domain consisting of  $r_x$  elements in the  $x$  direction and  $r_y$  elements in the  $y$  direction, each element having  $N_x$  and  $N_y$  grid in  $x$  and  $y$  directions respectively, will be  $(N_x r_x + 1)(N_y r_y + 1)$  and the corresponding global coefficient matrix  $[C^{global}]$  will be of the order  $(N_x r_x + 1)(N_y r_y + 1) \times (N_x r_x + 1)(N_y r_y + 1)$ . The global equations then are

$$C_{p_g q_g}^{global} \phi_{q_g}^{global} = e_{p_g}^{global} \quad (3.44)$$

where, the  $\phi^{global}$  vector incorporates all the unknown  $\phi_{lm}$  of all the elements and the indices  $p_g$  and  $q_g$  represent the global indices given by

$$\begin{aligned} p_g &= 1, \dots, (N_x \cdot r_x + 1) \cdot (N_y \cdot r_y + 1) \\ q_g &= 1, \dots, (N_x \cdot r_x + 1) \cdot (N_y \cdot r_y + 1) \end{aligned} \quad (3.45)$$

### 3.4 Imposition of Boundary conditions

The boundary conditions corresponding to the stream function-vorticity formulation of the problem presented in section 2.7.2 are basically of the two types: homogeneous Neumann boundary conditions and Dirichlet boundary conditions. The variational formulation of the Helmholtz equation (3.8) using the functional (3.9) automatically satisfies homogeneous Neumann boundary conditions and, therefore, no modification of the elemental coefficient matrices in Equation (3.3.3) is needed to impose these boundary conditions.

Dirichlet boundary conditions may be imposed by matrix condensation. Accordingly, the rows and columns corresponding to grid points having Dirichlet boundary conditions are eliminated from the system matrix. Although, this method leads to computational economy by reducing the order of the original system matrix, it is somewhat complicated to implement.

To impose Dirichlet boundary conditions we apply a simple stratagem commonly used in the finite element method. The diagonal element of global matrix  $[C^{global}]$  in Equation (3.44) corresponding to the grid points having Dirichlet boundary conditions are equated to a very large number ( $10^{130}$ , say) and the corresponding element in the right side vector,  $\{e^{global}\}$  are set equal

to the specified boundary value multiplied by the same very large number. Then the resulting global equations are solved to obtain the solution. The advantage of this method lies in its simplicity of implementation, at the cost of only slight inefficiency of computation.

### 3.5 Solution of Global Equations

Once the global system of algebraic equations (3.44) is suitably modified to impose Dirichlet boundary conditions, an efficient method for solving linear system of algebraic equations is needed. Generally, the selection of an efficient matrix solver depends on the structure of matrix equation.

In the present case, the left hand side coefficient matrix is typically sparse. In addition, only the right hand side vector in the global matrix equation takes on different values in the successive time levels. For this situation, where the left hand side coefficient matrix remains the same in each successive time level, LU decomposition has a distinct advantage over other matrix solution methods. For, once we decompose the coefficient matrix into lower (L) and upper (U) triangular matrices, we can solve the matrix equation (3.44) for different right hand side vectors as many times as required to obtain the state solution merely at the cost of one forward and one backward substitution for each time step. Thus, the LU decomposition, being computationally least expensive, is employed to solve the system of linear algebraic equations (3.44).

### 3.6 Numerical Solution Procedure

The temporal discretization of the general transport equation for the flow property  $\phi$  has been presented in section 3.3.1. Adopting exactly the same discretization scheme, the time discretized form of each of the governing equations for temperature, vorticity and stream function are represented by a Helmholtz equation as given in Equation (3.8). The corresponding parameter  $\lambda^2$  and forcing function  $f$  are defined in Tables 3.1 and 3.2 for natural and mixed convective flows respectively.

The spatial discretization of the Helmholtz equation (3.8) by spectral element method leading to a system of linear algebraic equations (3.44) has been presented in section 3.2.2. Each of the Helmholtz equations for temperature, vorticity and stream function is discretized to obtain the corresponding system of linear algebraic equations. As the governing equations for temperature, vorticity and stream function are coupled, these systems of linear algebraic equations are solved in tandem at each time step. The asymptotic steady state solutions of the governing equations are obtained by time marching. The procedure is as given below:

1. Specify the initial guess ( $n=0$ ) for the temperature, vorticity, stream function and velocity components.
2. Solve the energy equation (2.28 or 2.30) for the  $(n+1)$ th time step.
3. Solve the vorticity transport equation (2.27 or 2.29) for the  $(n+1)$ th time step.
4. Solve the Cauchy-Kowaleska equation (2.26) for the stream function for the  $(n+1)$ th time step.
5. Compute the velocity field from the stream function using Equation (2.21).
6. Check the convergence by the criterion

$$rms = \sqrt{\frac{\sum_{i=1}^{N_{total}} (\phi_i^{n+1} - \phi_i^n)^2}{N_{total}}} < \varepsilon \quad (3.46)$$

for all fields.

7. Update all dependent variables, i.e.,  $\phi_i^n \leftarrow \phi_i^{n+1}; i=1, \dots, N_{total}$

Step 2-7 are repeated until the condition (3.46) is satisfied by all dependent variables  $\phi$ .

### 3.7 Spatial Derivatives at Collocation Points

Like the spectral method, spectral element method also allows an accurate evaluation of derivatives of dependent variables. The spatial derivatives of the dependent variable  $\phi$  with respect to  $X$  and  $Y$  are given by equation (3.29) and (3.30). For any point ( $X = x_r, Y = y_p$ ) in the  $i^{th}$  element, equation (3.29) can be rewritten as

$$\left( \frac{\partial \phi}{\partial X} \right)_r = \frac{2}{L_x} \frac{2}{N_x} \sum_{j=0}^{N_x} \sum_{n=0}^{N_x} \phi_{jp} F_{nj} D P_{nr} \quad (3.47)$$

Table 3.1 Expression for Parameter  $\lambda^2$  and forcing function  $f$  (natural convection flow)

Equation	$\phi$	$\lambda^2$	$f$
Energy	$\theta$	$\frac{Pr\sqrt{Gr_H}}{\Delta\tau}$	$-\text{Pr}\sqrt{Gr_H}\left[\frac{\theta^n}{\Delta\tau} - \left(\frac{\partial U\theta}{\partial X} + \frac{\partial V\theta}{\partial Y}\right)^n\right]$
Vorticity transport	$\Omega$	$\frac{\sqrt{Gr_H}}{\Delta\tau}$	$-\sqrt{Gr_H}\left[\frac{\Omega^n}{\Delta\tau} - \left(\frac{\partial U\Omega}{\partial X} + \frac{\partial V\Omega}{\partial Y} - \frac{\partial\theta}{\partial X}\right)^n\right]$
Stream function	$\Psi$	$\frac{1}{\Delta\tau}$	$-\left(\frac{\Psi^n}{\Delta\tau} + \Omega^n\right)$

Table 3.2 Expression for Parameter  $\lambda^2$  and forcing function  $f$  (mixed convection flow)

Equation	$\phi$	$\lambda^2$	$f$
Energy	$\theta$	$\frac{PrRe_H}{\Delta\tau}$	$-PrRe_H\left[\frac{\theta^n}{\Delta\tau} - \left(\frac{\partial U\theta}{\partial X} + \frac{\partial V\theta}{\partial Y}\right)^n\right]$
Vorticity transport	$\Omega$	$\frac{Re_H}{\Delta\tau}$	$-Re_H\left[\frac{\Omega^n}{\Delta\tau} - \left(\frac{\partial U\Omega}{\partial X} + \frac{\partial V\Omega}{\partial Y} - \frac{Gr_H}{Re_H^2}\frac{\partial\theta}{\partial X}\right)^n\right]$
Stream function	$\Psi$	$\frac{1}{\Delta\tau}$	$-\left(\frac{\Psi^n}{\Delta\tau} + \Omega^n\right)$

where

$$F_{nj} = \frac{1}{\bar{C}_j \bar{C}_n} \cos\left(\frac{n\pi j}{N_x}\right) \quad (3.48)$$

and

$$\begin{aligned}
 DP_{nr} &= \frac{n \sin\left(\frac{n\pi r}{N_x}\right)}{\sin\left(\frac{\pi r}{N_x}\right)} & r \neq 0 \quad \text{or} \quad N_x \\
 &= n^2 & r = 0 \\
 &= (-1)^{n-1} n^2 & r = N_x
 \end{aligned} \quad (3.49)$$

Similar treatment works to evaluate the derivative with respect to  $Y$ .

### 3.8 Accuracy of the Simulations

In the simulations that follow in Chapter 4, the computational domain is typically discretized in  $5 \times 3$  or  $6 \times 2$  (and for high aspect ratios,  $6 \times 1$ ) elements. The number of grid points in each element was always  $N_x=7$  and  $N_y=7$ , in the two directions. While the number of elements used may not seem to be very many, it should be recalled that the spectral element method

Table 3.3 Grid Convergence test based on average Nusselt numbers for three different aspect ratio of the channel in the natural convection case at  $Gr_H = 10^5$

$A_r$	$Nu_{av}$		$Nu'_{av}$	
	$5 \times 3$ elements	$6 \times 2$ elements	$5 \times 3$ elements	$6 \times 2$ elements
1.43	11.343	11.395	11.215	11.278
1.52	11.337	11.366	11.208	11.257
1.67	11.311	11.323	11.189	11.240

has exponential order accuracy, which means that the truncation error decreases faster than any finite power of the number of grid-points.

To illustrate the accuracy of the simulations, the computed average Nusselt numbers for three different aspect ratios in the natural convection problem, at  $Gr_H = 10^5$ , are shown in Table 3.3. The Nusselt numbers are computed in two different ways:  $Nu_{av}$  is obtained from the temperature derivative at the walls, and  $Nu'_{av}$  from an integral energy balance. The Table 3.3 shows that the computed values of the two Nusselt numbers are very close, as are the results from the  $5 \times 3$  and  $6 \times 2$  element discretizations. Throughout this study, the difference in the values of  $Nu_{av}$  and  $Nu'_{av}$  has been used as diagnostic of the numerical error. This difference is typically within 1.5%.





# Chapter 4

## Results and Discussion

In this chapter we present the results for the optimum spacing problem for the cases of (a) natural convection, and (b) mixed convection, between a series of heated vertical parallel plates. The formulation of these problems has been already presented in Chapter 2 of this thesis and will be only briefly summarized here. The numerical technique which applies the spectral element method to stream function, vorticity and energy equations had already been described in Chapter 3. Below we first present the results for the natural convection case, and then consider the mixed convection problem.

### 4.1 Natural Convection Case

The physical problem has been depicted in Figure 2.1 which shows a vertical parallel plate channel with symmetrically heated walls simulating either one element of a parallel array of such channels, or else as a single channel standing alone.

The equations solved for this case are (2.26), (2.27), and (2.28) presented in Chapter 2. The false transient technique is used to arrive at the steady state solutions of the stream function,  $\Psi$ , the vorticity,  $\Omega$ , and the temperature,  $\theta$ . These equations are solved with the boundary conditions shown in Figure 4.1. Note that the computational domain depicted in Figure 4.1 includes an inlet entrance region that extends to 10% of the plate height  $H$  below the plates. This region serves to simulate in the numerical solution

the gradual variation of flow and temperature that would occur at the inlet of the actual physical problem shown in Figure 2.1.

Recall that, for the natural convection case, the mass inflow is not known and has to emerge from the numerical solution. This means that the value of  $\Psi_b$  shown as a boundary condition in Figure 4.1 has to be arrived at through an iterative procedure. This procedure, which is described in Section 2.6.3 (subsection “Mass Flow Rate for Natural Convection”), needs that the balance of momentum, buoyancy and viscous forces, resulting in Equation (2.31), be satisfied. Various trial values of  $\Psi_b$  are used till the correct  $\Psi_b$  that yields temperature and velocity fields satisfying Equation (2.31) is obtained. These calculations for natural convection are thus very computationally intensive, as every solution requires a number of trial solutions to be computed.

Although we always compute, and sometimes depict, the temperature and flow fields, our main concern is with the optimum spacing between the parallel plates which will give the highest heat transfer rate. Obviously, for every Grashof number,  $Gr_H$ , we might obtain a different optimum spacing or, equivalently, a different optimum aspect ratio  $A_r$ . So we need to find, for each  $Gr_H$ , the  $A_r$  for which either the average Nusselt number  $Nu_{av}$  (for the single channel case) or  $Nu_{av}A_r$  (for the multiple channel case) are the maximum (the logic of maximizing  $Nu_{av}A_r$  in the later case is given in Section 2.7). This requires that the Nusselt number be computed from the temperature field. The optimum spacing is primarily affected by the  $Gr_H$ . We have considered a set of  $Gr_H = 10^3, 10^4$ , and  $10^5$  for our problem.

### 4.1.1 Fluid Flow and Heat Transfer Patterns

In this section, we briefly describe the velocity and temperature fields obtained in our numerical solutions. The emphasis here is not so much on the quantitative results but rather on the qualitative features of the solutions and the physics involved in obtaining them. The aim below is to demonstrate that the numerical solutions are quite compatible with our understanding of the physical processes operating in parallel plate channels. This will be done by considering the velocity and temperature fields for certain specific cases involving three different Grashof numbers,  $Gr_H = 10^3, 10^4$ , and  $10^5$ , and four different aspect ratios.

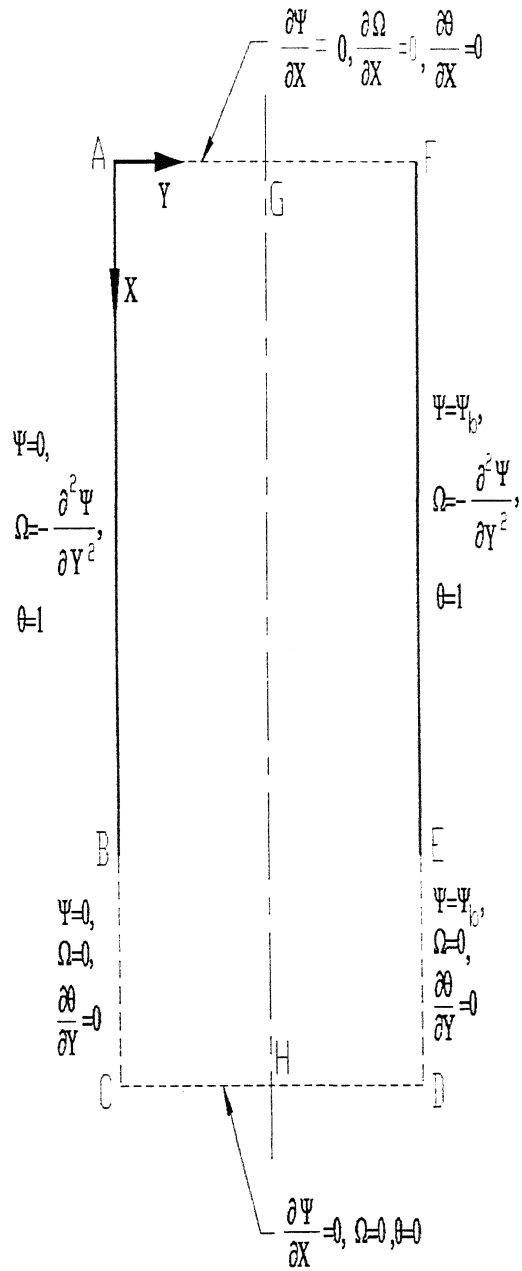


Figure 4.1: Computational domain with boundary conditions for stream-function, vorticity and temperature.

Figure 4.2 shows the velocity vector plots for an aspect ratio,  $A_r = 2.50$  and for three different Grashof numbers. In this figure, and in subsequent figures, the vertical and horizontal distances are shown, normalised by  $H$ , from the left corner of the inlet to the channel. Note that the plate starts at the vertical coordinate 0, the small region below being inlet upstream section included in the computational domain. It is evident from the figure that the velocity fields are roughly parabolic as expected and that the maximum velocity, attained at the central line, increases with Grashof number. In the case of the highest Grashof number, the velocity field is flatter in the central region indicating that the wall velocity boundary layers do not penetrate into the central zone of the channel. This too is expected as the boundary layer would be thinner for a higher Grashof number.

Figure 4.3 shows the streamlines for the same three cases. While the streamlines plots themselves are not very informative, the maximum stream function value indicated below the plots show that the induced volume flow rate is a strong function of Grashof number.

Figure 4.4 shows the isotherms for the same three cases. The difference between these plots is quite dramatic. The Figure 4.4(a) shows that for the lower Grashof number,  $Gr_H = 10^3$ , the fluid entering from the bottom of the channel is quickly heated as it rises and attains temperature very close to the wall temperature even half way along the channel. Figure 4.4(b) for the intermediate Grashof number shows the clear presence of thermal boundary layers and the central line temperatures do not come close to the wall temperature even at the exit of the channel. The plot for the highest Grashof number,  $Gr_H = 10^5$  shows even a stronger influence of the thermal boundary layers, with the central line temperatures remaining essentially at their inlet values deep into the channel.

We now consider the cases of four different aspect ratio channels for the intermediate Grashof number,  $Gr_H = 10^4$ . The aspect ratios considered are 1.000, 1.515, 2.000, and 3.125. It is to be noted that the higher aspect ratio channels are narrower. Figure 4.5 shows the velocity vector plots for these

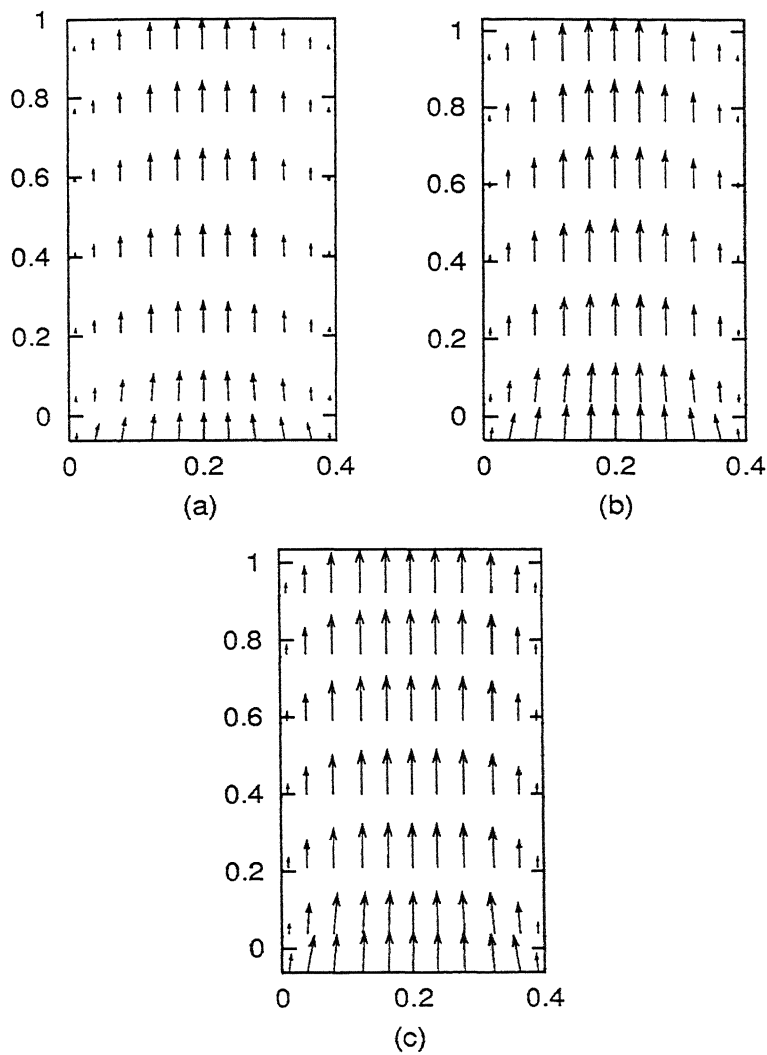


Figure 4.2: Vector plots for three different Grashof numbers and aspect ratio,  $A_r = 2.500$ , for the case of natural convection: (a)  $Gr_H = 10^3$ ; (b)  $Gr_H = 10^4$ ; (c)  $Gr_H = 10^5$ .

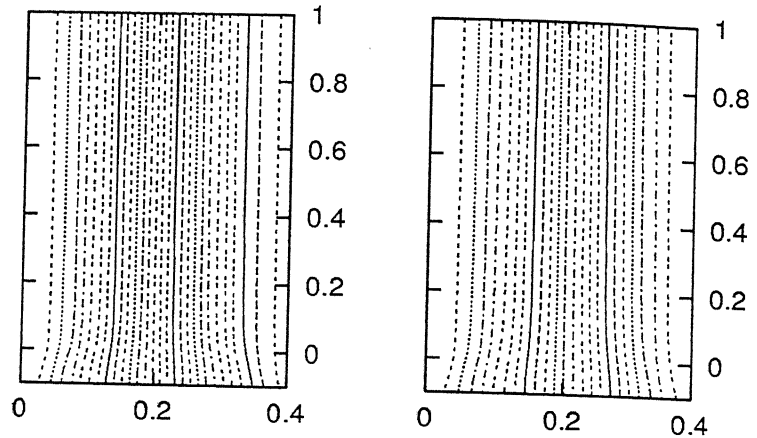
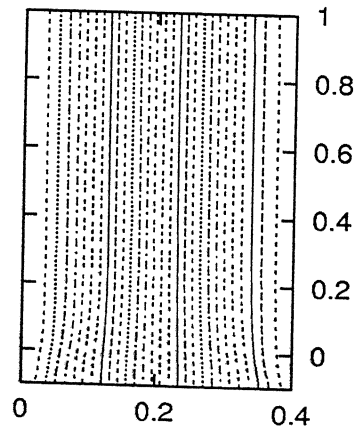
(a)  $|\Delta \Psi^*| = 4.472$ (b)  $|\Delta \Psi^*| = 23.698$ (a)  $|\Delta \Psi^*| = 90.726$ 

Figure 4.3: Streamlines for three different Grashof numbers and aspect ratio,  $A_r = 2.50$ , for the case of natural convection: (a)  $Gr_H = 10^3$ ; (b)  $Gr_H = 10^4$ ; (c)  $Gr_H = 10^5$ .

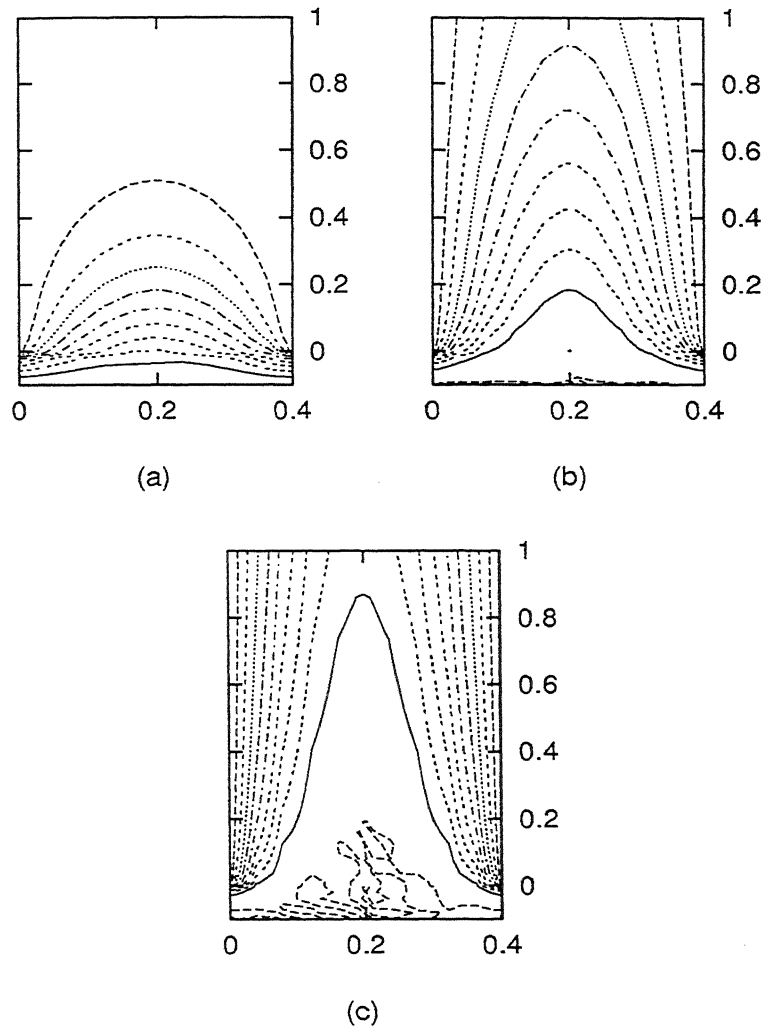


Figure 4.4: Isotherms for three different Grashof numbers and aspect ratio,  $A_r = 2.500$ , for the case of natural convection: (a)  $Gr_H = 10^3$ ; (b)  $Gr_H = 10^4$ ; (c)  $Gr_H = 10^5$ .



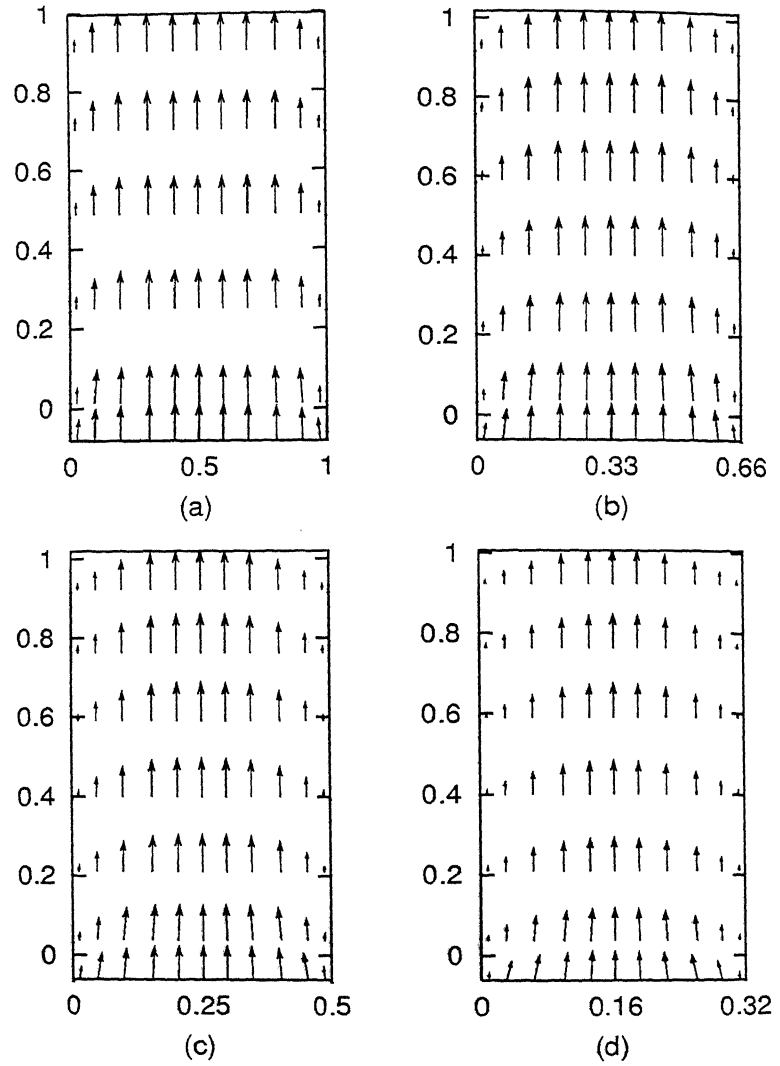


Figure 4.5: Vector plots for four different plate-to-plate channel spacing and  $Gr_H = 10^4$ , for the case of natural convection: (a)  $A_r = 1.000$ ; (b)  $A_r = 1.515$ ; (c)  $A_r = 2.000$ ; (d)  $A_r = 3.125$ .

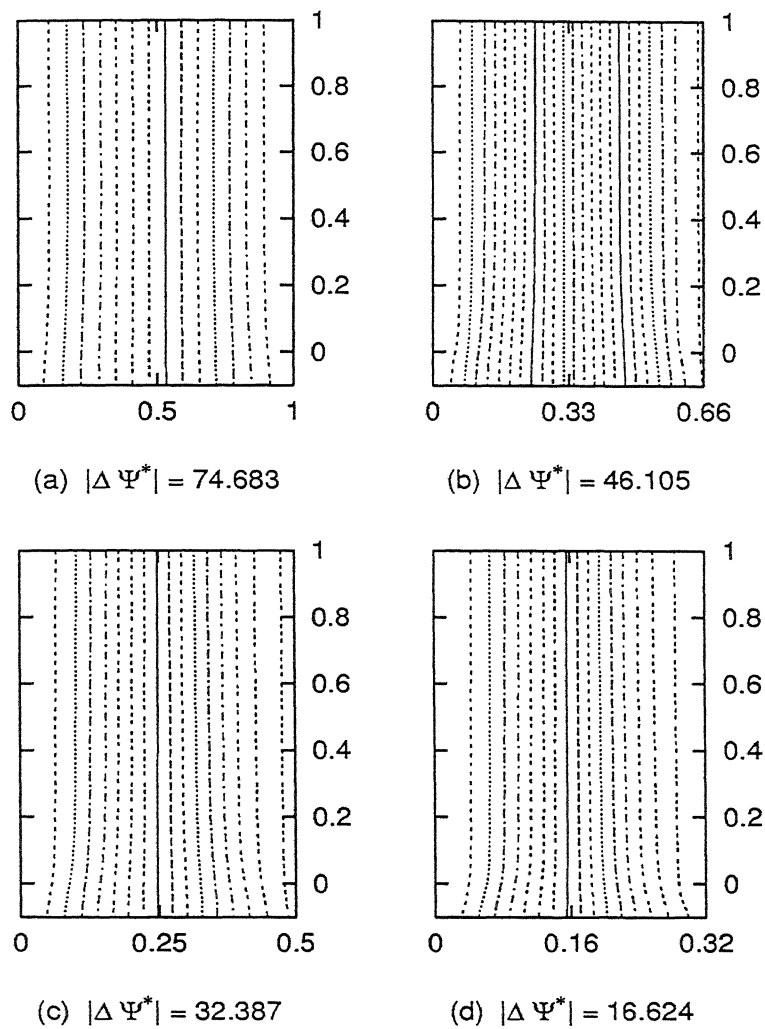


Figure 4.6: Streamlines for four different plate-to-plate channel spacing and  $Gr_H = 10^4$ , for the case of natural convection: (a)  $A_r = 1.000$ ; (b)  $A_r = 1.515$ ; (c)  $A_r = 2.000$ ; (d)  $A_r = 3.125$ .

four cases. The lowest aspect ratio channel, i.e., the widest among the four, shows a relatively flat profile in the central zone indicating that the width of the channel is much greater than the wall boundary layer thickness (although the four figures are scaled to be equally wide, the actual channel widths are quite different, as indicated by the horizontal coordinate). As the aspect ratio increases, the profile becomes closer to parabolic, i.e., closer to fully developed. The magnitude of the maximum velocity also decreases for the higher aspect ratio (narrower) channels. Figure 4.6 again shows the streamlines. The volume flow rate (maximum stream function value) indicated also show a decrease with increasing aspect ratio.

Figure 4.7 shows the isotherms for the same cases. It is quite clear that for the lowest aspect ratio (widest) channel, the thermal boundary layers do not penetrate into the central zone. As the channel becomes narrower, the boundary layers meet at the central line. For the narrowest channel [Figure 4.7 (d)], thermal boundary layers meet quite close to the inlet of the channel. Interestingly, as will be seen later, the case depicted in Figure 4.7(b) is close to the optimum spacing for the single channel case at this  $Gr_H$ , while Figure 4.7(d) shows the case close to the optimum spacing for the multiple channel case.

These figures show the physics involved in determining the optimum spacing. It is clear that the spacing in case (a) can be reduced further without significantly affecting the heat transfer as the boundary layers do not meet and the central zone is essentially still at the inlet temperature. However, once the boundary layers meet, further decrease in the spacing would reduce the volume flow rate without much increase in the heat transfer per unit volume flow as the outflow temperature is already close to the maximum attainable. So the optimum spacing for the single channel case seems to be that which allows the thermal boundary layer to meet somewhere close to the outflow plane. For the multiple channel case, we maximize  $Nu_{av}A_r$  and can thus decrease the spacing further as the resulting increase in the aspect ratio compensates for the decrease in  $Nu_{av}$ , up to a point. Thus, optimum spacing for the multiple channel case occurs at a higher aspect ratio as shown in figure 4.7(d).

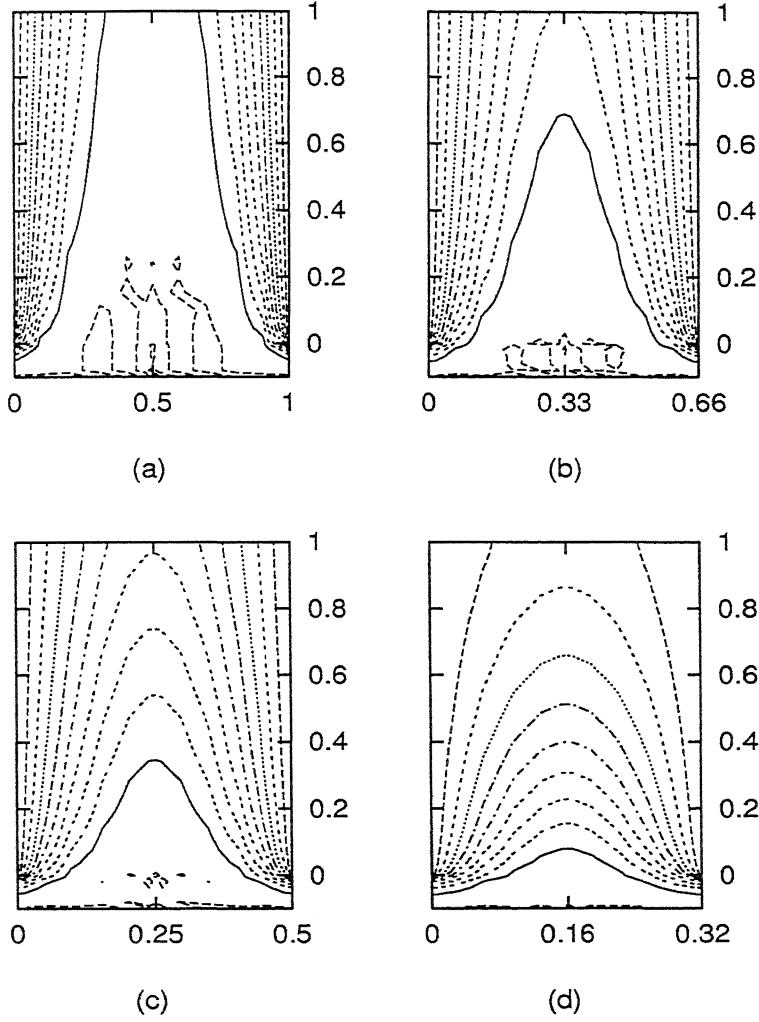


Figure 4.7: Isotherms for four different plate-to-plate channel spacing and  $Gr_H = 10^4$ , for the case of natural convection: (a)  $A_r = 1.000$ ; (b)  $A_r = 1.515$ ; (c)  $A_r = 2.000$ ; (d)  $A_r = 3.125$ .

Table 4.1 Dimensionless induced flow rate( $\Delta\Psi$ ), average Nusselt number, and the product of average Nusselt number and aspect ratio for different aspect ratio of the channel at  $Pr = 0.70$ ,  $Gr_H = 10^3$

$A_r$	$\Delta\Psi$	$Nu_{av}$	$Nu'_{av}$	$Nu_{av}A_r$	$Nu'_{av}A_r$
0.556	1.293	3.688	3.695	2.049	2.053
0.629	1.126	3.707	3.691	2.331	2.321
0.667	1.054	3.715	3.689	2.476	2.459
0.680	1.030	3.718	3.689	2.529	2.509
0.694	1.006	3.721	3.688	2.584	2.561
0.741	0.934	3.729	3.687	2.763	2.731
0.775	0.886	3.735	3.686	2.895	2.857
0.813	0.838	3.740	3.684	3.041	2.995
0.833	0.814	3.743	3.683	3.119	3.069
0.855	0.792	3.748	3.745	3.203	3.201
1.000	0.651	3.677	3.650	3.677	3.650
1.333	0.449	3.631	3.571	4.841	4.762
1.786	0.285	3.055	3.002	5.455	5.360
1.852	0.267	2.952	2.892	5.466	5.355
1.923	0.249	2.838	2.771	5.458	5.329
2.000	0.231	2.697	2.638	5.393	5.276
2.250	0.181	2.298	2.217	5.171	4.989
2.500	0.141	1.953	1.897	4.882	4.743
3.333	0.066	1.320	1.358	4.400	4.526

#### 4.1.2 Optimum Spacing and Volume Flow Rate in the Natural Convection Case

The numerical results are tabulated in full for the natural convection case in Tables 4.1, 4.2, and 4.3 respectively for  $Gr_H = 10^3, 10^4$  and  $10^5$ . In all cases, the Prandtl number,  $Pr$ , is taken to be 0.70. The range of aspect ratios in each case varies somewhat and is chosen so that the optimum spacing can be obtained for the chosen  $Gr_H$ .

The average Nusselt number,  $Nu_{av}$  over the heated walls of the channel has been computed in two different ways so as to provide a cross-check of

Table 4.2 Dimensionless induced flow rate ( $\Delta\Psi$ ), average Nusselt number, and the product of average Nusselt number and aspect ratio for different aspect ratio of the channel at  $Pr = 0.70$ ,  $Gr_H = 10^4$

$A_r$	$\Delta\Psi$	$Nu_{av}$	$Nu'_{av}$	$Nu_{av}A_r$	$Nu'_{av}A_r$
1.000	0.747	6.278	6.349	6.278	6.349
1.250	0.580	6.300	6.368	7.875	7.960
1.429	0.495	6.353	6.395	9.076	9.101
1.471	0.478	6.354	6.394	9.345	9.402
1.515	0.461	6.355	6.392	9.629	9.684
1.563	0.444	6.355	6.390	9.930	9.984
1.667	0.410	6.352	6.381	10.586	10.635
2.000	0.324	6.291	6.306	12.581	12.611
2.250	0.276	6.174	6.179	13.892	13.904
2.500	0.237	5.962	5.977	14.906	14.943
2.941	0.184	5.411	5.432	15.914	15.977
3.125	0.166	5.125	5.155	16.017	16.110
3.333	0.148	4.791	4.816	15.968	16.054
3.571	0.133	4.318	4.340	15.422	15.499
4.000	0.105	3.561	3.572	14.245	14.287
5.000	0.061	2.183	2.178	10.914	10.890

Table 4.3 Dimensionless induced flow rate ( $\Delta\Psi$ ), average Nusselt number, and the product of average Nusselt number and aspect ratio for different aspect ratio of the channel at  $Pr = 0.70$ ,  $Gr_H = 10^5$

$A_r$	$\Delta\Psi$	$Nu_{av}$	$Nu'_{av}$	$N'_{av}A_r$	$Nu'_{av}A_r$
1.333	0.597	11.343	11.214	15.123	14.952
1.389	0.570	11.342	11.213	15.753	15.574
1.429	0.552	11.343	11.215	16.204	16.021
1.449	0.544	11.343	11.214	16.439	16.252
1.471	0.543	11.335	11.205	16.669	16.478
1.515	0.521	11.337	11.208	17.178	16.982
1.613	0.488	11.339	11.210	18.288	18.080
1.667	0.468	11.311	11.189	18.852	18.649
2.000	0.378	11.298	11.218	22.595	22.436
2.500	0.287	11.268	11.196	28.171	27.990
3.333	0.197	11.204	11.109	37.347	37.030
5.000	0.114	9.918	9.855	49.588	49.275
5.263	0.104	9.531	9.439	50.162	49.680
5.555	0.095	9.071	8.974	50.393	49.852
5.882	0.086	8.513	8.412	50.076	49.483
6.667	0.067	7.086	6.989	47.237	46.594

the accuracy of the numerical results. The one which is based on the normal temperature gradient at the wall is

$$Nu_{av} = \int_0^1 \frac{\partial \theta}{\partial Y} \Big|_{Y=0} dX \quad (4.1)$$

The second method of computing the average Nusselt number is based on the energy balance of the heat flux from the walls and at the inlet and the outlet of the channel. For the latter, both the convective and conductive fluxes are considered. This balance yields the following dimensionless equation for the average Nusselt number:

$$\begin{aligned} Nu'_{av} = \frac{1}{2} \{ & -Pr\sqrt{G_{rH}} \int_0^{\frac{1}{A\tau}} U\theta \Big|_{X=0} dY - \int_0^{\frac{1}{A\tau}} \frac{\partial \theta}{\partial X} \Big|_{X=1} dY \\ & + \int_0^{\frac{1}{A\tau}} \frac{\partial \theta}{\partial X} \Big|_{X=0} dY + Pr\sqrt{G_{rH}} \int_0^{\frac{1}{A\tau}} U\theta \Big|_{X=1} dY \} \end{aligned} \quad (4.2)$$

where the first term on the right corresponds to convective heat flux at the outlet, the second term to conductive heat flux at the inlet, the third term to conductive heat flux at the outlet, and the fourth term to convective heat flux at the inlet of the channel.

Special care was taken for computing the second and the fourth integral of  $Nu'_{av}$ . These integrals were actually computed along a surface slightly outside the channel entrance in order to avoid the expected leading-edge singularity at the inlet of the channel. It was noticed that while the conduction term at the outlet of the channel was negligibly small (as the flow there is convection dominated), the outward (downward) flow of heat at the inlet due to conduction is surprisingly significant.

The two alternative ways of computing the Nusselt number provide us with a means of cross-checking the accuracy of the numerical simulations. It can be seen from Tables 4.1, 4.2, and 4.3 that the difference between the two values of the Nusselt numbers is never more than 3.5% and usually lies within 1.5%. This degree of correspondence is reassuring. In the plots that follows, only  $Nu_{av}$  (Equation 4.1) is presented, as the two different Nusselt numbers would be indistinguishable on a graph.



Table 4.4: Comparison of the present work with Anand et al. (1992), with regards to maximum average Nusselt number

Grashof number, $Gr_H$	Maximum average Nusselt number $(Nu_{av})_{max}$	
	Anand et al., 1992	Present study
$10^3$	3.55	3.74
$10^4$	6.15	6.36
$10^5$	10.85	11.34

### Single Channel Case

The Figure 4.8 shows the average Nusselt number as a function of the aspect ratio for all three Grashof numbers. It can be seen that, as expected, the Grashof number has a significant effect on the  $Nu_{av}$  and hence the heat transfer. For the single channel case, the maximum  $Nu_{av}$  would determine the optimum spacing. It can be seen from the figure that such an optimum does exist. This is because as the aspect ratio increases (i.e., the width decreases), the flow rate decreases but the temperature gradients increase and the overall heat transfer may be increased. As the aspect ratio increases, the “chimney effect” would also create a greater draft and hence greater heat transfer. These contrasting effects ensure that an optimum plate-to-plate spacing does exist which is greater than zero. However, from the Figure 4.8 we can see that the  $Nu_{av}$  dependency on aspect ratio is minimal for low  $Ar$ . So the optimum is not a strong one. In fact, it can be argued that any aspect ratio below 0.85 for  $Gr_H = 10^3$ , 1.67 for  $Gr_H = 10^4$  and 2.00 for  $Gr_H = 10^5$  would be close to optimum for the single channel case.

Table 4.4 shows the comparison of the present results with that of Anand et al. (1992) who solved the same problem using the boundary layer equations. The table shows the maximum  $Nu_{av}$  obtained in the two studies. It can be seen that the two results are quite close, thereby showing that the boundary layer approximation is surprisingly accurate for the quantities considered.

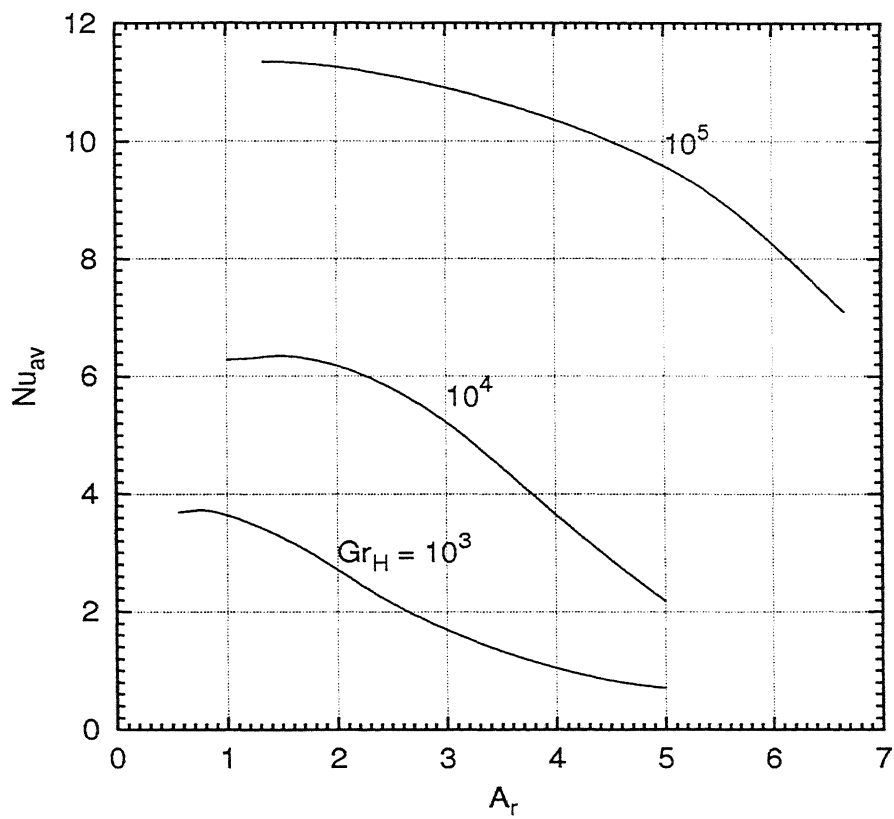


Figure 4.8: Variation of average Nusselt number with aspect ratio at three different Grashof numbers, for the natural convection case.

Table 4.5 Range of optimum aspect ratios and maximum heat transfer rate for the single and multiple channel cases

$Gr_H$	Single channel case		Multiple channel case	
	$(A_r)_{opt}$	$(Nu_{av})_{max}$	$(A_r)_{opt}$	$(Nu_{av}A_r)_{max}$
$10^3$	0.81 - 0.85	3.74	1.79 - 1.92	5.46
$10^4$	1.25 - 1.67	6.36	2.94 - 3.33	16.02
$10^5$	1.33 - 2.00	11.34	5.26 - 5.88	50.39

### Multiple Channel Case

For the multiple channel case, as was argued in Section 2.7, the maximum of the product  $Nu_{av}A_r$  determines the optimum  $A_r$ . Figure 4.9 shows the quantity  $Nu_{av}A_r$  versus aspect ratio,  $A_r$ , for the three Grashof numbers ( $Gr_H = 10^3, 10^4$ , and  $10^5$ ). It may be seen that the optimum is more clearly demarcated in these cases as compared to those in the single channel case. Table 4.5 shows the optimum spacing and the values  $Nu_{av}A_r$ . The trend is quite evident. As  $Gr_H$  increases, optimum aspect ratio also increases, i.e., the optimum channel width decreases.

As will be seen below, when  $Gr_H$  is kept constant and  $A_r$  is increased the volume flow rate drops quite sharply leading to lower heat transfer. When  $Gr_H$  is increased, higher volume flow rate and hence heat transfer rate will be maintained for a greater range of aspect ratios. Therefore, the optimum  $A_r$  tends to increase with increasing  $Gr_H$ . Practically, this means that with higher  $Gr_H$ , the channel walls should optimally be closer.

### Volume Flow Rate

Figure 4.10 shows the induced flowrate,  $\Delta\Psi$ , values for different  $A_r$  and  $Gr_H$ . This quantity gives the nondimensional volume flow rate,  $\Delta\Psi = \frac{\dot{v}}{\nu\sqrt{Gr_H}}$ , where,  $\dot{v}$  is the volume flow rate per unit depth of the channel. It can be seen in Figure 4.10 that the nondimensional volume flow rate increases only slightly with  $Gr_H$  for a constant aspect ratio. However, this is only an artefact of the nondimensionalisation used. Figure 4.11 shows the same data with a

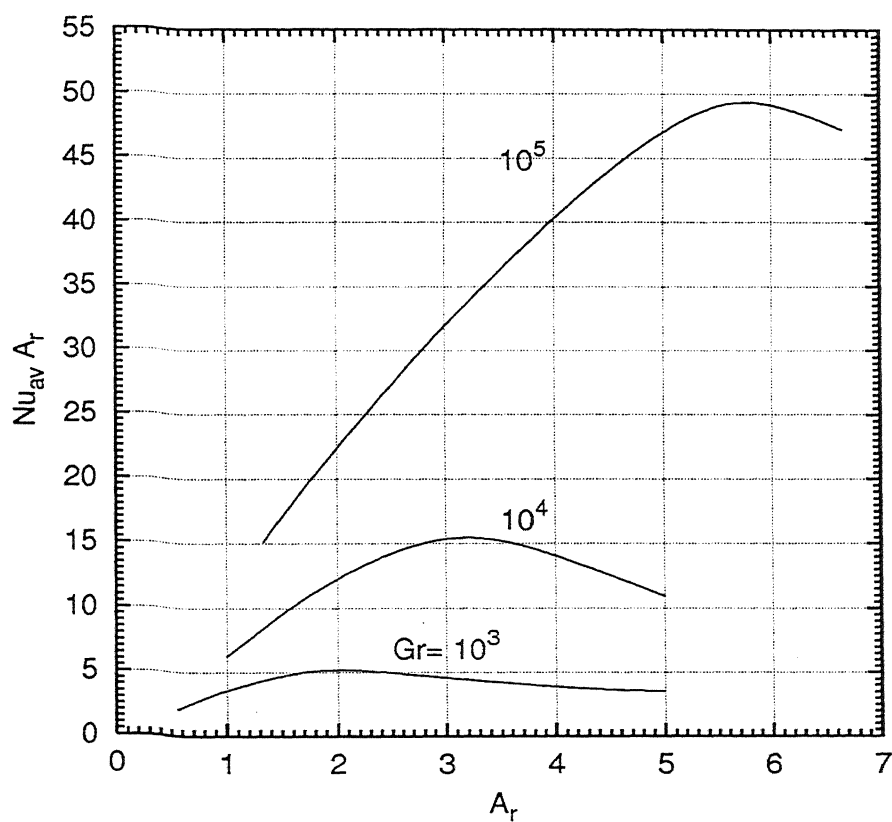


Figure 4.9: Variation of the product of average Nusselt number and aspect ratio with aspect ratio at three different Grashof numbers, for the natural convection case.

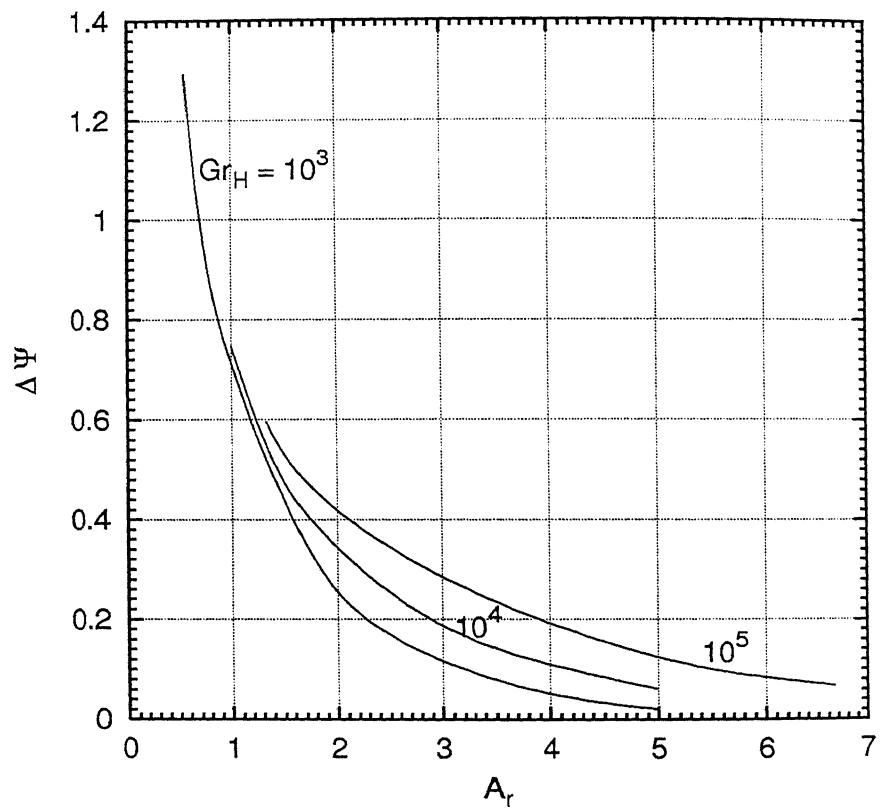


Figure 4.10: Variation of dimensionless induced volume flow rate with aspect ratio at three different Grashof numbers, for the natural convection case.

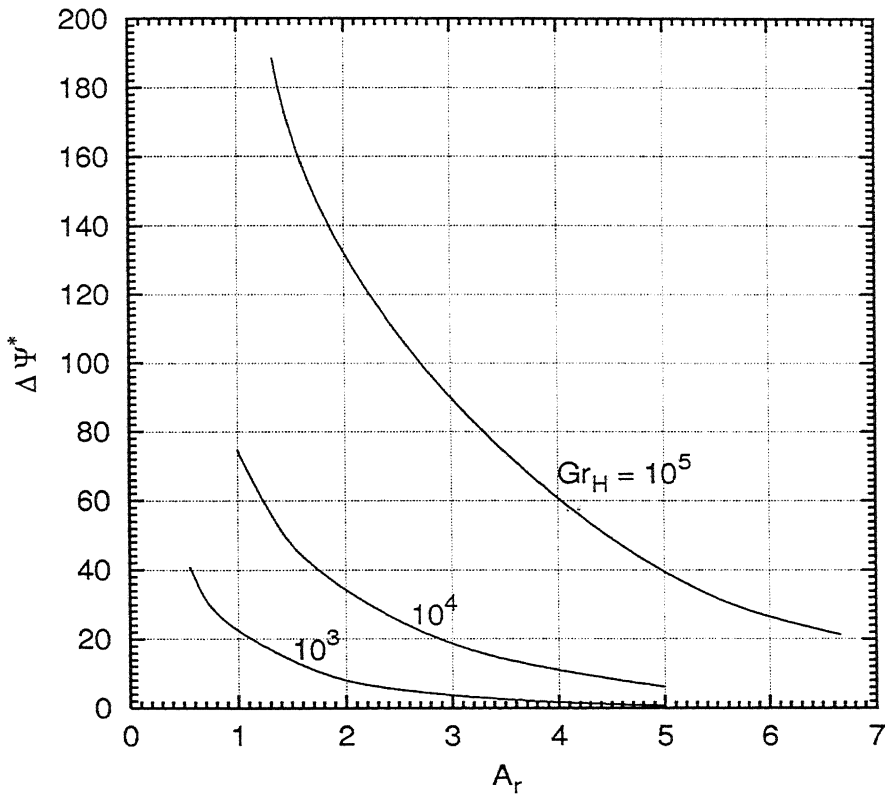


Figure 4.11: Variation of the induced volume flow rate, differently non-dimensionalised, with aspect ratio at three different Grashof numbers, for the natural convection case.

different nondimensionalisation of the volume flow rate,  $\Delta\Psi^* = \frac{\dot{v}}{\nu}$ . It can be seen that the effect of increasing  $Gr_H$  is quite dramatic, the volume flow rate increasing dramatically with  $Gr_H$ . As the computations were not done for very low aspect ratios (i.e., large channel width), the “chimney effect” is not discernible in these figures, for the flow rate decreases monotonically with increasing aspect ratio, in all cases.

## 4.2 Mixed Convection Case

In this section, the results for the mixed convection case are presented for both the single and the multiple channel cases for  $Pr = 0.70$ ,  $Gr_H = 10^3, 10^4$ , and  $10^5$ , and buoyancy parameter values of  $\frac{Gr_H}{Re_H^2} = 0.1, 0.5, 1.0$ , and  $1.5$ .

The physical situation is the same as depicted in Figure 2.1, except that an external flow is superimposed on the buoyancy-induced natural convection. The governing equations solved for this case are (2.26), (2.29), and (2.30) which use the false transient method to obtain the steady state solutions. These equations are solved with the boundary conditions shown in Figure 4.1. Note that the stream function, vorticity and the velocity components are nondimensionalised differently than in the natural convection case. Furthermore, unlike in the natural convection case, the stream function value at the right plate,  $\Psi_b$  is known *a priori* and is given by  $\Psi_b = -A_r^{-1}$  where,  $A_r$  is the aspect ratio of the channel (the dimensional  $\psi_b = -U_c L$ , nondimensionalised by dividing by  $U_c H$ , yields the non-dimensional  $\Psi_b$  is  $-L/H$  or  $-A_r^{-1}$ ). With this and the other boundary conditions, the problem can be solved by the usual method without iterating for the volume flow rate as was done in the natural convection case.

### 4.2.1 Fluid Flow and Heat Transfer Patterns

In this section, we qualitatively describe the numerical solutions to show that they are compatible with the physics of flows in vertical parallel plate channels. We consider specific cases involving three different Grashof numbers, four different aspect ratios, and four different values of the buoyancy parameter.

Figure 4.12 shows the velocity vector plots for an aspect ratio,  $A_r = 2.50$  and for three Grashof numbers,  $Gr_H = 10^3, 10^4$ , and  $10^5$  for a fixed buoyancy

parameter of 1.0. It is apparent from the figure that the velocity profiles are roughly parabolic for the lower Grashof numbers indicating that the flow becomes fully developed quickly along the channel. However, for the highest Grashof number, the velocity profile in the central region of the channel is relatively flat indicating that the boundary layers have not reached the central core of the channel. Figure 4.13 shows the streamlines for the same cases. The corresponding non-dimensional volume flow rate,  $\Delta\Psi$  ( $=\dot{v}/U_c H = A_r^{-1}$ , where  $\dot{v}$  is the volume flow rate per unit depth; Recall that [see Chapter 2] the dimensionless variables are differently defined for the natural and mixed convection cases) is the same in all cases as  $A_r$  is kept constant. However, the *dimensional* volume flow rate increases with Grashof number, for a fixed buoyancy parameter. However, unlike in the natural convection case, the inlet velocity in this case is essentially imposed and the volume flow rate increases only because a higher Grashof number for a fixed buoyancy parameter implies a higher Reynolds number, and thus a greater flow rate.

Figure 4.14 shows the isotherms for the same three cases. The differences between these plots are quite apparent. For the highest Grashof number,  $Gr_H$  (and  $Re_H$ ) case, the flow is obviously not fully developed and the boundary layers are clearly evident. For the low  $Gr_H$  (and  $Re_H$ ) cases the boundary layers meet in the flow domain and the outlet temperature is quite close to the plate temperature, particularly so for the lowest  $Gr_H$  (and  $Re_H$ ) case.

Figure 4.15 shows the velocity vector plots for  $Gr_H = 10^4$  and  $\frac{Gr_H}{Re_H^2} = 1.0$ , and four different aspect ratios 1.6667, 2.7778, 3.3333, and 5.0000. Here, the flow tends to become fully developed for the highest aspect ratio (i.e., the narrowest channel) while remaining relatively flat near the central line for the lowest aspect ratio case. Figure 4.16 shows the streamlines for the same cases indicating the corresponding non-dimensionalised volume flow rate,  $\Delta\Psi$ . Here, as both the Grashof number and buoyancy parameter are fixed, the volume flow rate (both dimensional and non-dimensional) is seen to decrease with increasing aspect ratio, as expected.

Figure 4.17 shows the isotherms for the same cases. It can be seen that the thermal boundary layers tend to meet closer to the inlet as the aspect ratio is increased. Interestingly, the case shown in Figure 4.17(b) corresponds to the optimum spacing (i.e. with the highest  $Nu_{av}$ ) for the single channel



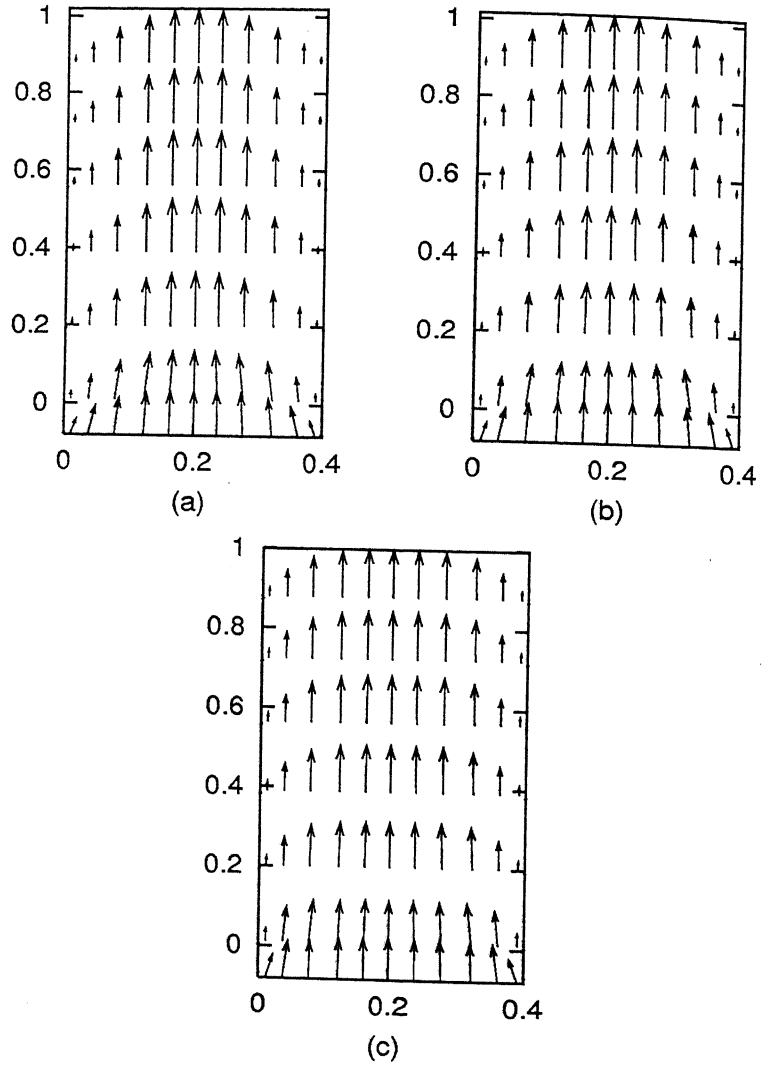


Figure 4.12: Vector plots for three different Grashof numbers and  $A_r = 2.50$ ,  $Gr_H/Re_H^2 = 1.0$ , for the case of mixed convection: (a)  $Gr_H = 10^3$ ; (b)  $Gr_H = 10^4$ ; (c)  $Gr_H = 10^5$ .

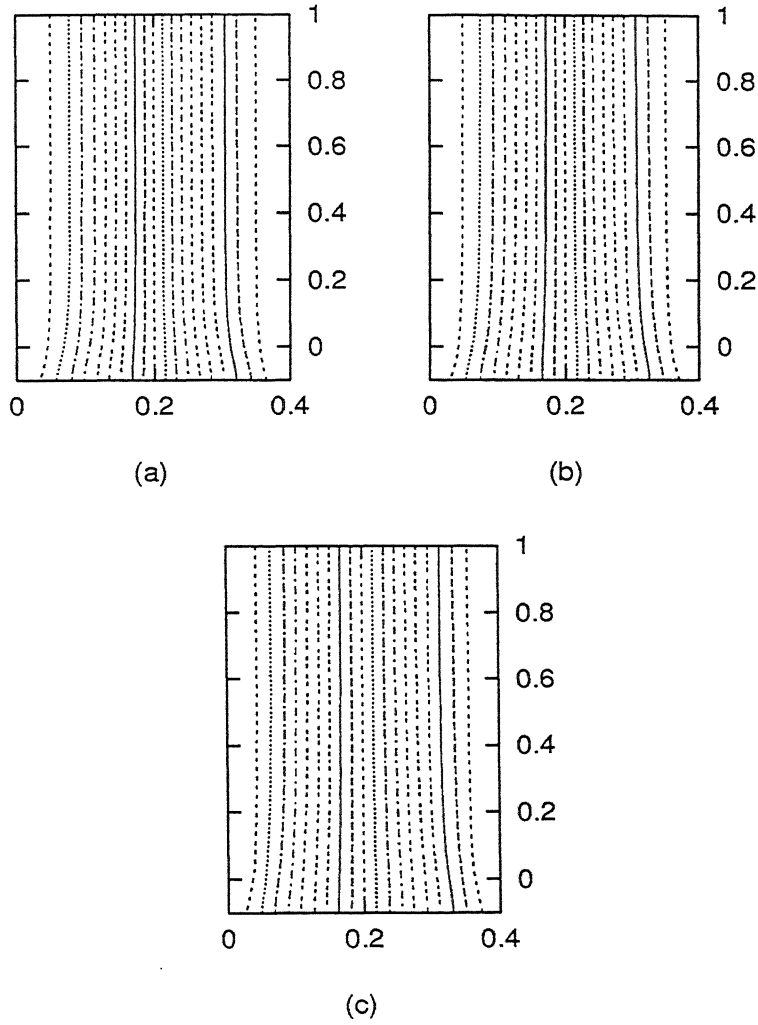


Figure 4.13: Streamlines for three different Grashof numbers and  $A_r = 2.50$ ,  $Gr_H/Re_H^2 = 1.0$ , for the case of mixed convection: (a)  $Gr_H = 10^3$ ; (b)  $Gr_H = 10^4$ ; (c)  $Gr_H = 10^5$ .

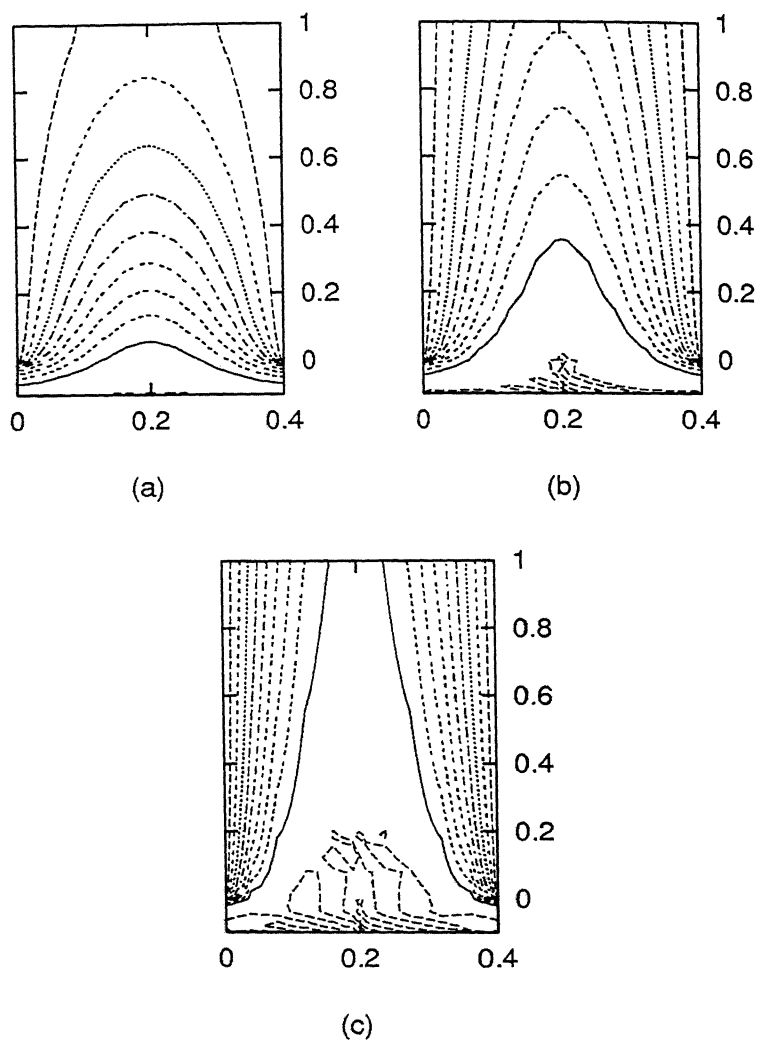


Figure 4.14: Isotherms for three different Grashof numbers and  $A_r = 2.50$ ,  $Gr_H/Re_H^2 = 1.0$ , for the case of mixed convection: (a)  $Gr_H = 10^3$ ; (b)  $Gr_H = 10^4$ ; (c)  $Gr_H = 10^5$ . The volume flow rate  $\Delta\Psi = 0.4$  for all cases.

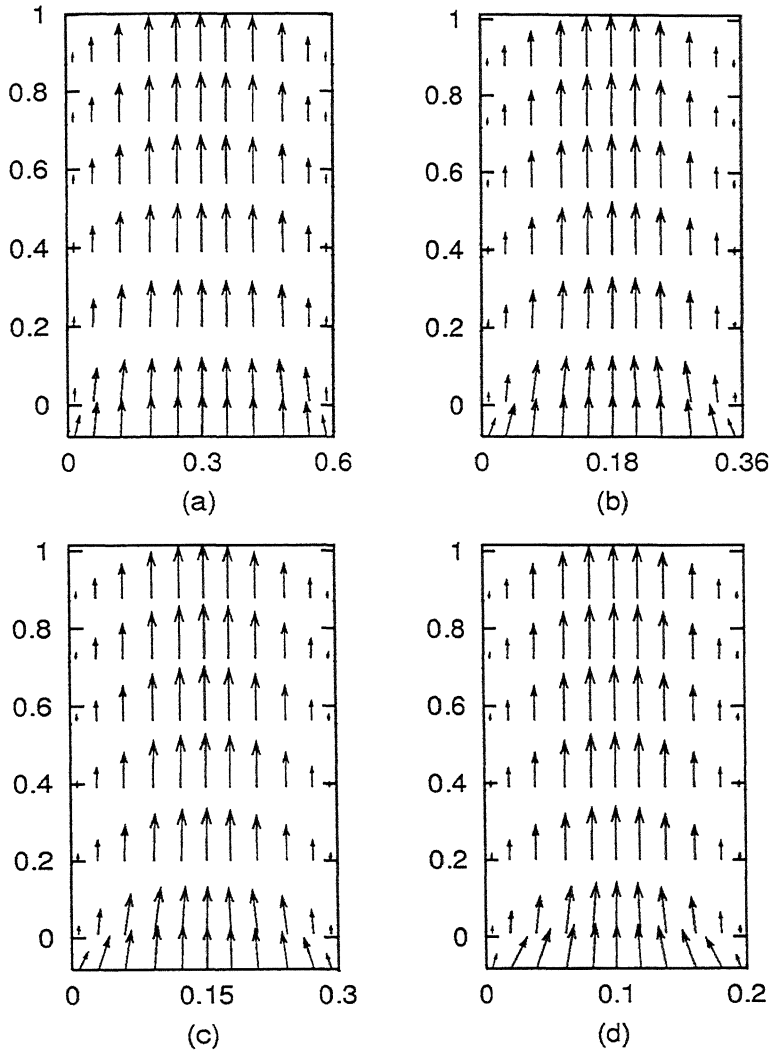


Figure 4.15: Vector plots for four different channel spacing and  $Gr_H = 10^4$ ,  $Gr_H/Re_H^2 = 1.0$ , for the case of mixed convection: (a)  $Ar = 1.6667$ ; (b)  $Ar = 2.7778$ ; (c)  $Ar = 3.3333$ ; (d)  $Ar = 5.0000$ .

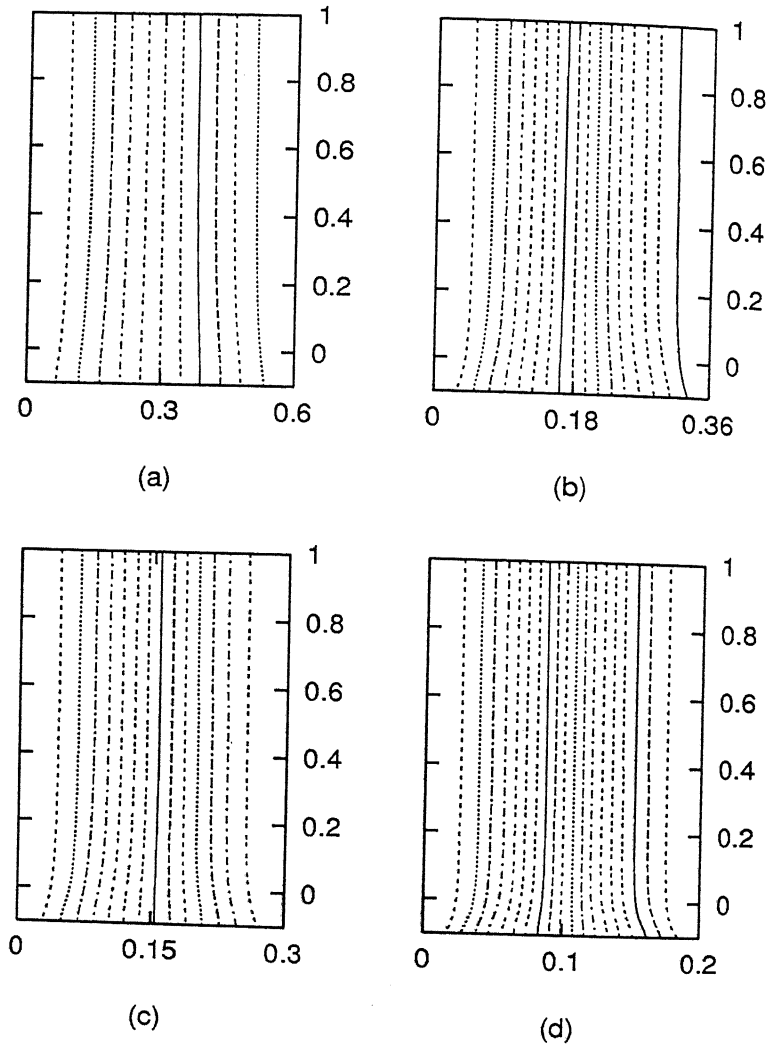


Figure 4.16: Streamlines for four different channel spacing and  $Gr_H = 10^4$ ,  $Gr_H/Re_H^2 = 1.0$ , for the case of mixed convection: (a)  $A_r = 1.6667$ ,  $\Delta\Psi = 0.6$ ; (b)  $A_r = 2.7778$ ,  $\Delta\Psi = 0.36$ ; (c)  $A_r = 3.3333$ ,  $\Delta\Psi = 0.30$ ; (d)  $A_r = 5.0000$ ,  $\Delta\Psi = 0.2$

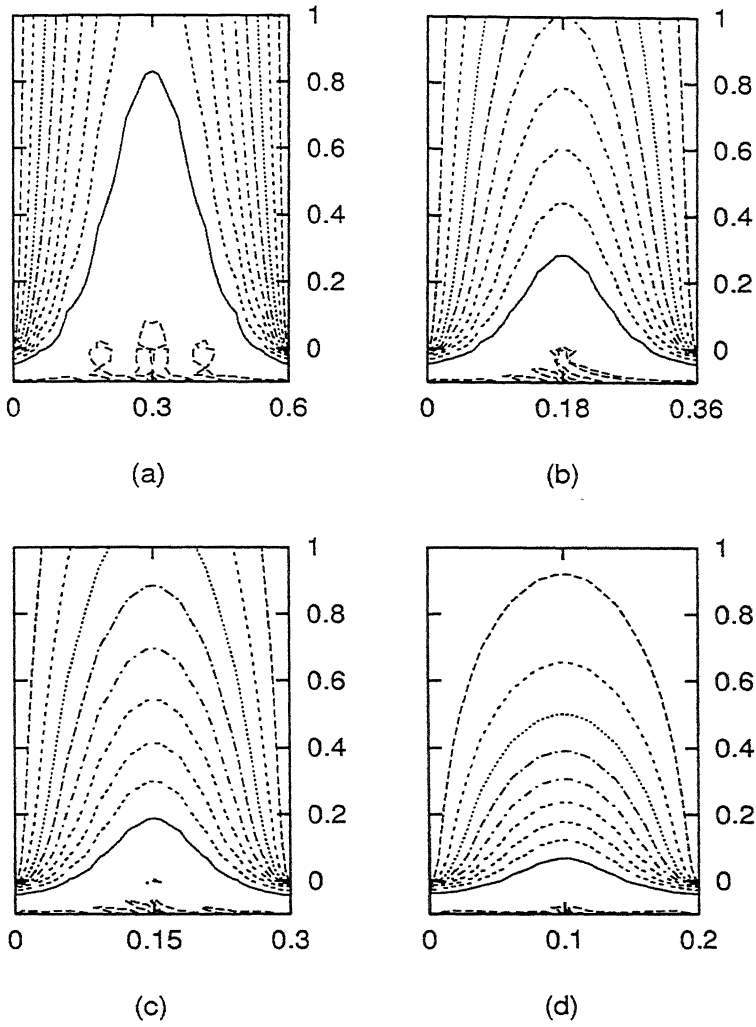


Figure 4.17: Isotherms for four different channel spacing and  $Gr_H = 10^4$ ,  $Gr_H/Re_H^2 = 1.0$ , for the case of mixed convection: (a)  $A_r = 1.6667$ ; (b)  $A_r = 2.7778$ ; (c)  $A_r = 3.3333$ ; (d)  $A_r = 5.0000$ .

at this  $Gr_H = 10^4$ . As the aspect ratio is increased the channel become narrower and the thermal gradient should become steeper. However, the volume flow rate of the imposed flow also decreases. These counter-acting effects seem to yield an optimum  $Nu_{av}$  when the boundary layers meet close to half way down the channel. For the multiple channel case, the net flow rate per unit width does not decrease as aspect ratio increases. Hence, the product  $Nu_{av}A_r$  keep on increasing with aspect ratio finally to an asymptotic maximum value at high aspect ratio (this will be shown later). Figure 4.17(d) shows a case very close to this asymptotic maximum.

Figure 4.18 shows the velocity vector plots for four different buoyancy parameters ( $= 0.1, 0.5, 1.0$ , and  $1.5$ ) at fixed  $A_r = 2.5$  and  $Gr_H = 10^4$ . It can be seen that as the buoyancy parameter increases from  $0.1$  to  $1.5$  (and  $Re_H$  decreases) the velocity boundary layers become thicker as expected. While the velocity profile at  $\frac{Gr_H}{Re_H^2} = 0.1$  is flat throughout the central core of the channel, it tends to become parabolic as buoyancy parameter increases (and  $Re_H$  decreases). Figure 4.19 depicts the streamlines for the same conditions showing corresponding dimensionless volume flow rate. Although the nondimensional volume flow rate remains constant for all the cases shown, as the buoyancy parameter increases and  $Re_H$  decreases, the dimensional volume flow rate decreases.

Figure 4.20 illustrates isotherms for four different buoyancy parameters ( $= 0.1, 0.5, 1.0$ , and  $1.5$ ) and  $Gr_H = 10^4$ . It is clearly evident from these isotherms that as the buoyancy parameter increases ( $Re_H$  decreases), the thermal boundary layer becomes thicker. At  $\frac{Gr_H}{Re_H^2} = 0.1$  (i.e., the highest  $Re_H$ ), the two thermal boundary layers do not meet inside the channel, indicating that inter-plate spacing has to be decreased further in order to obtain an optimum spacing. As  $\frac{Gr_H}{Re_H^2}$  increases to  $0.5$  and above, the two thermal boundary layers meet inside the channel and this meeting point moves towards the inlet of the channel.

### 4.2.2 Optimum Spacing in the Mixed Convection Case

The numerical results are tabulated for the mixed convection case in Tables 4.6-4.17 for  $Gr_H = 10^3, 10^4$ , and  $10^5$  and  $\frac{Gr_H}{Re_H^2} = 0.1, 0.5, 1.0$ , and  $1.5$ . The

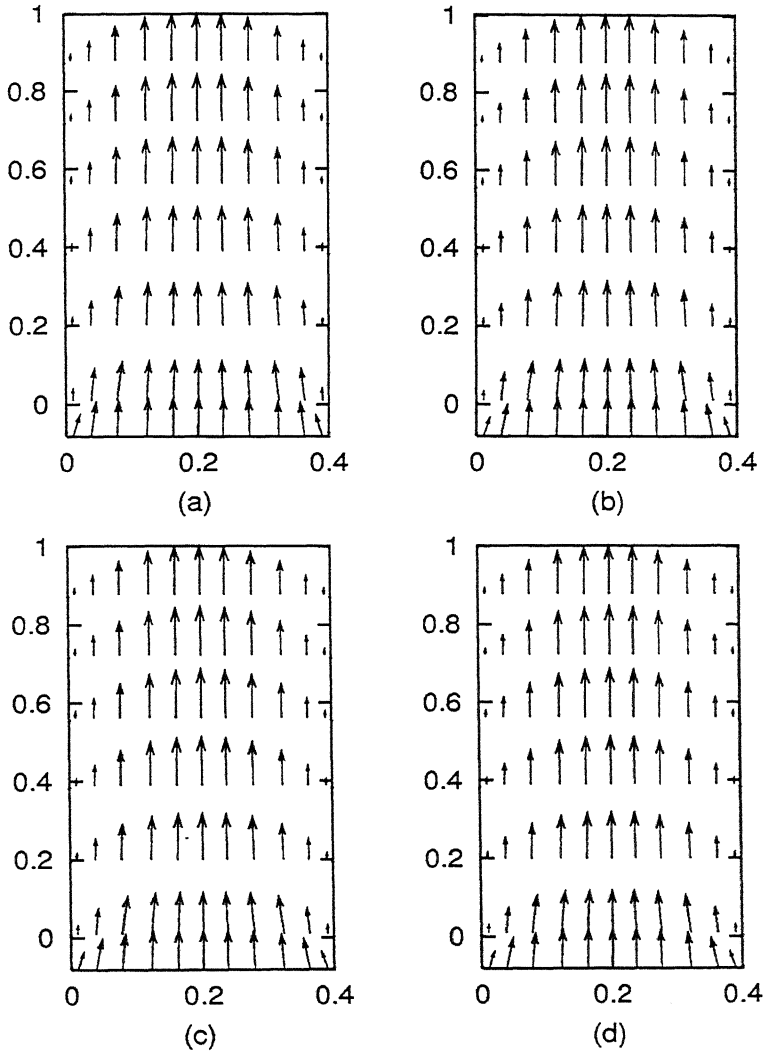


Figure 4.18: Vector plots for four different channel buoyancy parameters and  $Gr_H = 10^4$ ,  $A_r = 2.50$ , for the case of mixed convection: (a)  $Gr_H/Re_H^2 = 0.1$ ; (b)  $Gr_H/Re_H^2 = 0.5$ ; (c)  $Gr_H/Re_H^2 = 1.0$ ; (d)  $Gr_H/Re_H^2 = 1.5$ .



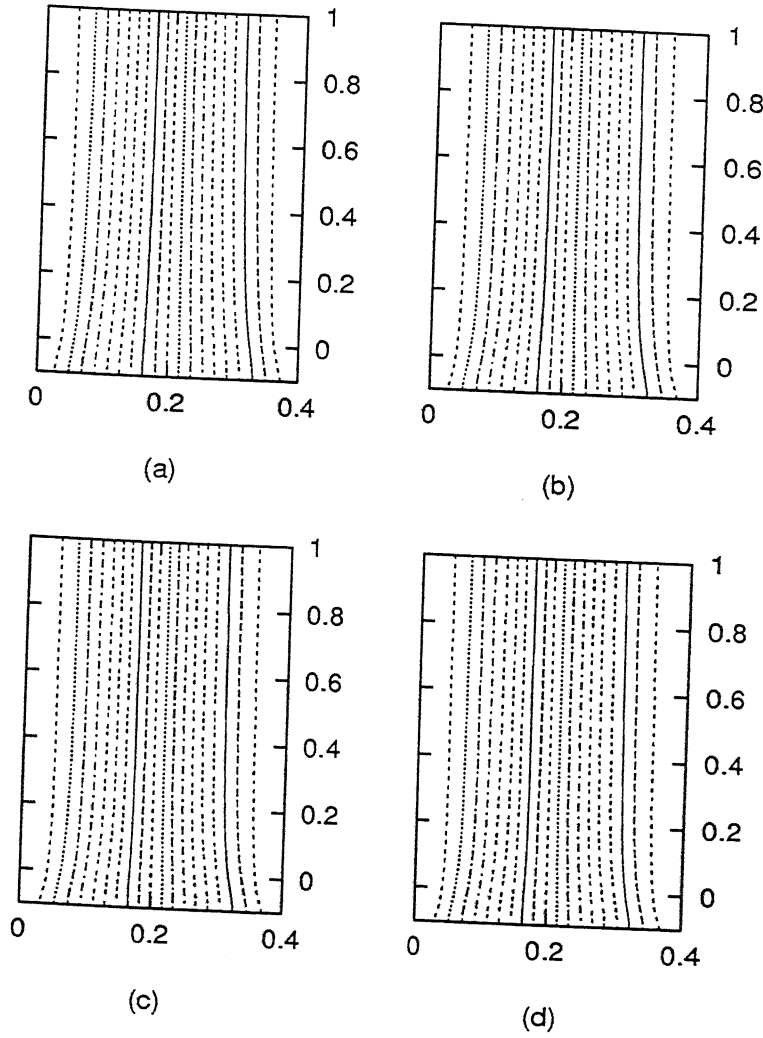


Figure 4.19: Streamlines for four different buoyancy parameters and  $Gr_H = 10^4$ ,  $A_r = 2.50$ , for the case of mixed convection: (a)  $Gr_H/Re_H^2 = 0.1$ ; (b)  $Gr_H/Re_H^2 = 0.5$ ; (c)  $Gr_H/Re_H^2 = 1.0$ ; (d)  $Gr_H/Re_H^2 = 1.5$ . The volume flow rate  $\Delta\Psi = 0.40$  for all cases.

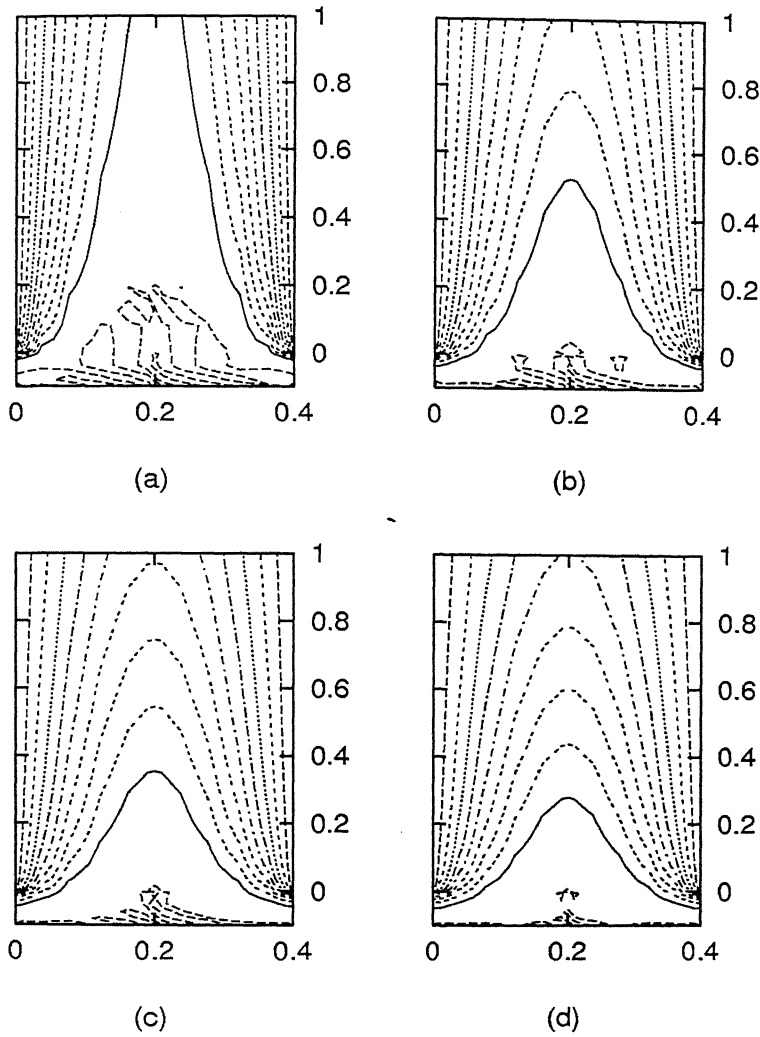


Figure 4.20: Isotherms for four different buoyancy parameters and  $Gr_H = 10^4$ ,  $A_r = 2.50$ , for the case of mixed convection: (a)  $Gr_H/Re_H^2 = 0.1$ ; (b)  $Gr_H/Re_H^2 = 0.5$ ; (c)  $Gr_H/Re_H^2 = 1.0$ ; (d)  $Gr_H/Re_H^2 = 1.5$ .

Table 4.6 Variation of pressure drop, average Nusselt number, and the product of average Nusselt number and aspect ratio, with aspect ratio for mixed convection case at  $Pr = 0.70$ ,  $Gr_H = 10^3$ , and  $\frac{Gr_H}{Re_H^2} = 0.1$

$A_r$	$\Delta P_{av}$	$Nu_{av}$	$Nu'_{av}$	$Nu_{av}A_r$	$Nu'_{av}A_r$
1.000	0.276	6.745	6.702	6.745	6.702
2.000	0.322	7.374	7.382	14.747	14.763
2.500	0.353	7.600	7.621	18.999	19.051
2.778	0.374	7.667	7.679	21.296	21.330
3.030	0.396	7.677	7.681	23.262	23.276
3.125	0.404	7.660	7.669	23.937	23.964
3.226	0.413	7.677	7.650	24.764	24.677
3.333	0.423	7.650	7.622	25.500	25.406
3.448	0.434	7.613	7.584	26.253	26.150
3.571	0.446	7.559	7.532	26.997	26.902
5.000	0.592	6.413	6.378	31.889	32.064
6.667	0.786	5.037	5.058	33.582	33.719
7.143	0.842	4.798	4.739	34.272	33.851
7.692	0.908	4.392	4.412	33.782	33.937
8.333	0.985	4.057	4.078	33.811	33.981
10.000	1.185	3.380	3.400	33.804	34.004

Prandtl number,  $Pr$ , in all these cases is 0.70. The average Nusselt numbers have been computed as before in two different ways;  $Nu_{av}$  using the temperature derivative at the wall and  $Nu'_{av}$  by using the heat balance. The difference between these two computed values are generally within 2 to 3 per cent. Thus only  $Nu_{av}$  is presented in the figures that follow.

### Single Channel Case

In the single channel case the optimum aspect ratio is determined simply by the maximum  $Nu_{av}$ . Figures 4.21, 4.22, and 4.23 show the average Nusselt number versus the aspect ratio for different buoyancy parameters, and  $Gr = 10^3, 10^4$ , and  $10^5$ , respectively. It can be seen that, unlike in the natural convection case, the maxima here are quite clear. However, it can also

Table 4.7 Variation of pressure drop, average Nusselt number, and the product of average Nusselt number and aspect ratio, with aspect ratio for mixed convection case at  $Pr = 0.70$ ,  $Gr_H = 10^3$ , and  $\frac{Gr_H}{Re_H^2} = 0.5$

$A_r$	$\Delta P_{av}$	$Nu_{av}$	$Nu'_{av}$	$Nu_{av}A_r$	$Nu'_{av}A_r$
1.667	0.444	5.227	5.298	8.712	8.831
1.754	0.459	5.246	5.312	9.204	9.319
1.786	0.470	5.220	5.292	9.322	9.450
1.852	0.477	5.257	5.317	9.736	9.846
1.923	0.495	5.229	5.293	10.056	10.178
1.961	0.497	5.258	5.311	10.310	10.414
2.000	0.509	5.225	5.285	10.451	10.570
2.500	0.613	5.039	5.098	12.599	12.744
3.333	0.815	4.441	4.462	14.804	14.873
5.000	1.253	3.093	3.127	15.463	15.636
5.263	1.325	2.946	2.977	15.507	15.668
5.556	1.406	2.798	2.825	15.546	15.692
5.882	1.496	2.649	2.671	15.585	15.710
6.250	1.597	2.499	2.514	15.619	15.713
6.667	1.711	2.291	2.359	15.275	15.725
7.143	1.842	2.137	2.201	15.266	15.724

Table 4.8: Variation of pressure drop, average Nusselt number, and the product of average Nusselt number and aspect ratio, with aspect ratio for mixed convection case at  $Pr = 0.70$ ,  $Gr_H = 10^3$ , and  $\frac{Gr_H}{Re_H^2} = 1.0$

$A_r$	$\Delta P_{av}$	$Nu_{av}$	$Nu'_{av}$	$Nu_{av}A_r$	$Nu'_{av}A_r$
1.449	0.413	4.511	4.601	6.538	6.668
1.515	0.430	4.518	4.602	6.845	6.973
1.587	0.449	4.519	4.598	7.173	7.299
1.667	0.470	4.513	4.587	7.521	7.645
1.754	0.495	4.498	4.566	7.891	8.011
1.852	0.524	4.471	4.534	8.280	8.396
1.961	0.557	4.430	4.486	8.686	8.796
2.000	0.572	4.364	4.453	8.729	8.907
2.083	0.596	4.368	4.417	9.099	9.203
2.222	0.644	4.241	4.319	9.424	9.597
2.500	0.740	4.044	4.110	10.110	10.274
4.000	1.309	2.791	2.860	11.163	11.438
5.000	1.711	2.224	2.318	11.120	11.588
5.882	2.064	1.898	1.981	11.162	11.652
6.667	2.376	1.679	1.753	11.192	11.684
7.143	2.564	1.568	1.637	11.199	11.694

Table 4.9: Variation of pressure drop, average Nusselt number, and the product of average Nusselt number and aspect ratio, with aspect ratio for mixed convection case at  $Pr = 0.70$ ,  $Gr_H = 10^3$ , and  $\frac{Gr_H}{Re_H^2} = 1.5$

$A_r$	$\Delta P_{av}$	$Nu_{av}$	$Nu'_{av}$	$Nu_{av}A_r$	$Nu'_{av}A_r$
1.333	0.322	4.161	4.261	5.547	5.681
1.389	0.339	4.162	4.257	5.780	5.913
1.449	0.359	4.158	4.249	6.027	6.158
1.515	0.382	4.150	4.236	6.288	6.419
1.587	0.407	4.135	4.216	6.563	6.692
1.667	0.436	4.111	4.187	6.852	6.978
1.754	0.469	4.077	4.148	7.153	7.277
1.852	0.507	4.031	4.095	7.464	7.584
1.961	0.551	3.969	4.027	7.782	7.896
2.083	0.603	3.887	3.938	8.098	8.204
2.500	0.793	3.524	3.592	8.809	8.981
3.333	1.215	2.769	2.863	9.230	9.542
5.000	2.039	1.876	1.974	9.379	9.870
5.882	2.481	1.606	1.692	9.446	9.952
6.667	2.868	1.425	1.500	9.497	9.999
7.143	3.101	1.332	1.402	9.514	10.016
7.692	3.368	1.242	1.307	9.552	10.053

Table 4.10 Variation of pressure drop, average Nusselt number, and the product of average Nusselt number and aspect ratio, with aspect ratio for mixed convection case at  $Pr = 0.70$ ,  $Gr_H = 10^4$ , and  $\frac{Gr_H}{Re_H^2} = 0.1$

$A_r$	$\Delta P_{av}$	$Nu_{av}$	$Nu'_{av}$	$Nu_{av}A_r$	$Nu'_{av}A_r$
1.667	0.145	11.585	11.468	19.308	19.113
1.961	0.149	11.832	11.729	23.199	22.998
2.222	0.155	12.327	12.046	27.394	26.769
2.500	0.158	12.285	12.126	30.712	30.315
3.333	0.171	13.071	12.767	43.570	42.557
5.000	0.200	13.358	13.308	66.789	66.540
5.263	0.208	13.374	13.314	70.388	70.073
5.556	0.217	13.359	13.288	74.217	73.824
5.882	0.227	13.304	13.221	78.257	77.771
6.667	0.253	13.017	12.906	86.777	86.041
7.692	0.288	12.381	12.253	95.239	94.253
10.000	0.372	10.513	10.382	105.125	103.824
12.500	0.466	8.637	8.526	107.959	106.580
16.667	0.624	6.502	6.424	108.368	107.071
20.000	0.751	5.415	5.355	108.307	107.095

Table 4.11 Variation of pressure drop, average Nusselt number, and product of average Nusselt number and aspect ratio with aspect ratio for mixed convection case at  $Pr = 0.70$ ,  $Gr_H = 10^4$ , and  $\frac{Gr_H}{Re_H^2} = 0.5$

$A_r$	$\Delta P_{av}$	$Nu_{av}$	$Nu'_{av}$	$Nu_{av}A_r$	$Nu'_{av}A_r$
1.667	0.178	8.368	8.381	13.947	13.969
1.961	0.191	8.581	8.586	16.826	16.835
2.222	0.207	8.847	8.783	19.659	19.519
2.500	0.219	8.984	8.935	22.459	22.337
2.857	0.237	9.041	9.019	25.831	25.768
3.125	0.252	9.109	9.094	28.465	28.418
3.333	0.264	9.202	9.125	30.673	30.415
3.571	0.278	9.192	9.124	32.829	32.587
3.704	0.287	9.178	9.110	33.992	33.740
4.000	0.306	9.110	9.041	36.439	36.163
5.000	0.373	8.318	8.320	41.588	41.602
6.667	0.510	6.985	6.969	46.568	46.458
10.000	0.800	4.805	4.795	48.050	47.947
11.111	0.897	4.322	4.318	48.023	47.982
12.500	1.018	3.843	3.837	48.038	47.967



Table 4.12: Variation of pressure drop, average Nusselt number, and the product of average Nusselt number and aspect ratio, with aspect ratio for mixed convection case at  $Pr = 0.70$ ,  $Gr_H = 10^4$ , and  $\frac{Gr_H}{Re_H^2} = 1.0$

$A_r$	$\Delta P_{av}$	$Nu_{av}$	$Nu'_{av}$	$Nu_{av}A_r$	$Nu'_{av}A_r$
1.754	0.157	7.404	7.435	12.989	13.044
1.961	0.172	7.520	7.542	14.745	14.788
2.222	0.196	7.692	7.670	17.092	17.045
2.500	0.216	7.764	7.748	19.411	19.370
2.564	0.221	7.777	7.760	19.941	19.896
2.778	0.239	7.800	7.779	21.666	21.608
2.857	0.245	7.726	7.733	22.075	22.094
3.030	0.261	7.788	7.763	23.599	23.524
3.333	0.289	7.681	7.648	25.602	25.494
5.000	0.465	6.353	6.380	31.764	31.898
5.556	0.533	5.892	5.914	32.732	32.855
6.667	0.674	5.038	5.057	33.586	33.714
8.333	0.889	4.059	4.077	33.826	33.976
9.091	0.986	3.722	3.740	33.840	33.999
10.000	1.102	3.382	3.400	33.823	33.002

Table 4.13 Variation of pressure drop, average Nusselt number, and the product of average Nusselt number and aspect ratio, with aspect ratio for mixed convection case at  $Pr = 0.70$ ,  $Gr_H = 10^4$ , and  $\frac{Gr_H}{Re_H^2} = 1.5$

$A_r$	$\Delta P_{av}$	$Nu_{av}$	$Nu'_{av}$	$Nu_{av}A_r$	$Nu'_{av}A_r$
1.961	0.125	6.955	6.987	13.638	13.700
2.222	0.154	7.067	7.058	15.705	15.685
2.381	0.170	7.079	7.075	16.855	16.845
2.564	0.188	7.083	7.076	18.161	18.144
2.778	0.212	7.057	7.046	19.601	19.573
3.030	0.241	6.985	6.970	21.167	21.123
3.333	0.278	6.847	6.827	22.824	22.757
5.000	0.512	5.332	5.374	26.658	26.870
6.667	0.783	4.128	4.164	27.520	27.760
7.143	0.861	3.858	3.892	27.560	27.802
7.692	0.951	3.544	3.618	27.569	27.828
8.333	1.055	3.310	3.341	27.581	27.844
9.091	1.177	3.033	3.064	27.577	27.851
10.000	1.321	2.756	2.785	27.562	27.849

Table 4.14 Variation of pressure drop, average Nusselt number, and the product of average Nusselt number and aspect ratio, with aspect ratio for mixed convection case at  $Pr = 0.70$ ,  $Gr_H = 10^5$ , and  $\frac{Gr_H}{Re_H^2} = 0.1$

$A_r$	$\Delta P_{av}$	$Nu_{av}$	$Nu'_{av}$	$Nu_{av}A_r$	$Nu'_{av}A_r$
2.222	0.076	21.136	19.752	46.970	43.893
3.333	0.082	21.464	20.648	71.545	68.827
4.000	0.083	22.119	21.013	88.475	84.051
5.000	0.085	22.259	21.785	111.297	108.924
6.667	0.091	23.239	22.843	154.929	152.284
7.692	0.100	23.661	23.282	182.005	179.091
8.333	0.106	23.858	23.468	198.817	195.563
9.091	0.113	23.974	23.570	217.949	214.270
10.000	0.122	23.940	23.521	239.400	235.214
11.111	0.134	23.653	23.224	262.813	258.042
12.500	0.149	22.971	22.550	287.139	281.877
16.667	0.196	19.752	19.374	329.198	322.900
25.000	0.295	13.741	13.496	343.530	337.411
33.333	0.395	10.269	10.119	342.287	337.287

Table 4.15 Variation of pressure drop, average Nusselt number, and the product of average Nusselt number and aspect ratio, with aspect ratio for mixed convection case at  $Pr = 0.70$ ,  $Gr_H = 10^5$ , and  $\frac{Gr_H}{Re_H^2} = 0.5$

$A_r$	$\Delta P_{av}$	$Nu_{av}$	$Nu'_{av}$	$Nu_{av}A_r$	$Nu'_{av}A_r$
2.381	0.090	14.738	14.328	35.091	34.115
3.333	0.104	15.311	15.026	51.035	50.086
3.704	0.110	15.540	15.283	57.556	56.603
5.000	0.119	15.761	15.380	78.803	76.902
5.882	0.137	15.969	15.856	93.938	93.267
6.250	0.146	15.997	15.855	99.978	99.091
6.667	0.155	15.961	15.808	106.410	105.384
7.692	0.179	15.645	15.465	120.342	118.962
10.000	0.237	14.114	13.913	141.143	139.128
12.500	0.304	12.040	11.855	150.500	148.189
16.667	0.419	9.213	9.074	153.542	151.226
20.000	0.511	7.684	7.573	153.687	151.453
25.000	0.649	6.140	6.061	153.499	151.512

Table 4.16 Variation of pressure drop, average Nusselt number, and the product of average Nusselt number and aspect ratio, with aspect ratio for mixed convection case at  $Pr = 0.70$ ,  $Gr_H = 10^5$ , and  $\frac{Gr_H}{Re_H^2} = 1.0$

$A_r$	$\Delta P_{av}$	$Nu_{av}$	$Nu'_{av}$	$Nu_{av}A_r$	$Nu'_{av}A_r$
2.222	0.066	12.849	12.536	28.552	27.858
3.030	0.085	13.207	13.002	40.022	39.400
3.333	0.092	13.363	13.174	44.542	43.914
4.546	0.110	13.397	13.376	60.896	60.799
4.762	0.116	13.432	13.402	63.960	63.818
5.000	0.123	13.452	13.413	67.259	67.065
5.263	0.132	13.451	13.401	70.795	70.531
5.556	0.141	13.421	13.359	74.561	74.217
5.882	0.151	13.352	13.277	78.539	78.102
6.667	0.178	13.042	12.937	86.944	86.248
10.000	0.304	10.513	10.383	105.130	103.835
12.500	0.405	8.636	8.526	107.955	106.579
16.667	0.575	6.503	6.424	108.385	107.072
20.000	0.708	5.417	5.355	108.336	107.096

Table 4.17: Variation of pressure drop, average Nusselt number, and the product of average Nusselt number and aspect ratio, with aspect ratio for mixed convection case at  $Pr = 0.70$ ,  $Gr_H = 10^5$ , and  $\frac{Gr_H}{Re_H^2} = 1.5$

$Ar$	$\Delta P_{av}$	$Nu_{av}$	$Nu'_{av}$	$Nu_{av} Ar$	$Nu'_{av} Ar$
2.778	0.046	12.120	11.943	33.666	33.174
3.030	0.056	12.224	12.070	37.042	36.576
3.333	0.065	12.345	12.197	41.152	40.655
4.167	0.077	12.162	12.180	50.674	50.749
4.348	0.084	12.178	12.188	52.949	52.992
4.546	0.091	12.184	12.185	55.380	55.385
4.762	0.099	12.173	12.164	57.968	57.926
5.000	0.109	12.142	12.120	60.711	60.602
6.667	0.180	11.383	11.303	75.890	75.353
8.333	0.261	10.067	9.974	83.894	83.113
10.000	0.344	8.712	8.620	87.115	86.197
12.500	0.474	7.059	6.987	88.232	87.343
14.286	0.566	6.185	6.120	88.352	87.430
16.667	0.687	5.300	5.247	88.313	87.446

Table 4.18 Range of optimum aspect ratio and corresponding average Nusselt number for different Grashof numbers and buoyancy parameters: Single Channel case

$Gr_H$	$\frac{Gr_H}{Re_H^2} = 0.1$		$\frac{Gr_H}{Re_H^2} = 0.5$		$\frac{Gr_H}{Re_H^2} = 1.0$		$\frac{Gr_H}{Re_H^2} = 1.5$	
	$A_r$	$Nu_{av}$	$A_r$	$Nu_{av}$	$A_r$	$Nu_{av}$	$A_r$	$Nu_{av}$
$10^3$	2.78-3.23	7.66	1.75-1.96	5.25	1.45-1.67	4.52	1.33-1.45	4.16
$10^4$	5.00-5.55	13.37	3.13-3.70	9.20	2.50-3.03	7.80	2.22-2.78	7.08
$10^5$	8.33-10.00	23.97	5.88-6.67	15.99	4.76-5.56	13.45	3.03-4.55	12.35

be seen that a range of aspect ratios give values of  $Nu_{av}$  close enough to the maximum that all may be considered optimum.

Table 4.18 shows the range of optimum aspect ratio and corresponding  $Nu_{av}$  for each  $Gr_H$  and for all buoyancy parameters considered. Some trends are immediately evident: as  $Gr_H$  increases, for a fixed buoyancy parameter, the optimum  $A_r$  increases (implying smaller plate-to-plate spacing) and the maximum  $Nu_{av}$  also increases. While it is clear that the  $Nu_{av}$  should increase with increasing  $Gr_H$ , it is not so obvious why the optimum spacing should decrease. However, it should be remembered that a fixed buoyancy parameter and increased  $Gr_H$  means a higher Reynolds number, and hence thinner momentum boundary layers. As  $Pr$  is fixed, the thinner momentum boundary layers directly imply thinner thermal boundary layers. As the optimum spacing is intimately related to the thickness of the thermal boundary layers at the walls, it is then understandable that thinner boundary layers should yield a lower optimum spacing.

Table 4.18 also shows that, for fixed  $Gr_H$ , the maximum  $Nu_{av}$  and the optimum  $A_r$  both decrease with an increasing buoyancy parameter. The cause of the decrease in the  $Nu_{av}$  is clear: when  $Gr_H$  is kept fixed, an increase in the buoyancy parameter implies decreased  $Re_H$ , which in turn implies greater viscosity and, as  $Pr$  is fixed, a greater  $\alpha$ . This in turn implies thickened boundary layers and hence lower temperature gradients and  $Nu_{av}$ . The thicker boundary layer also imply that the optimum spacing should increase (and the optimum  $A_r$  should decrease).

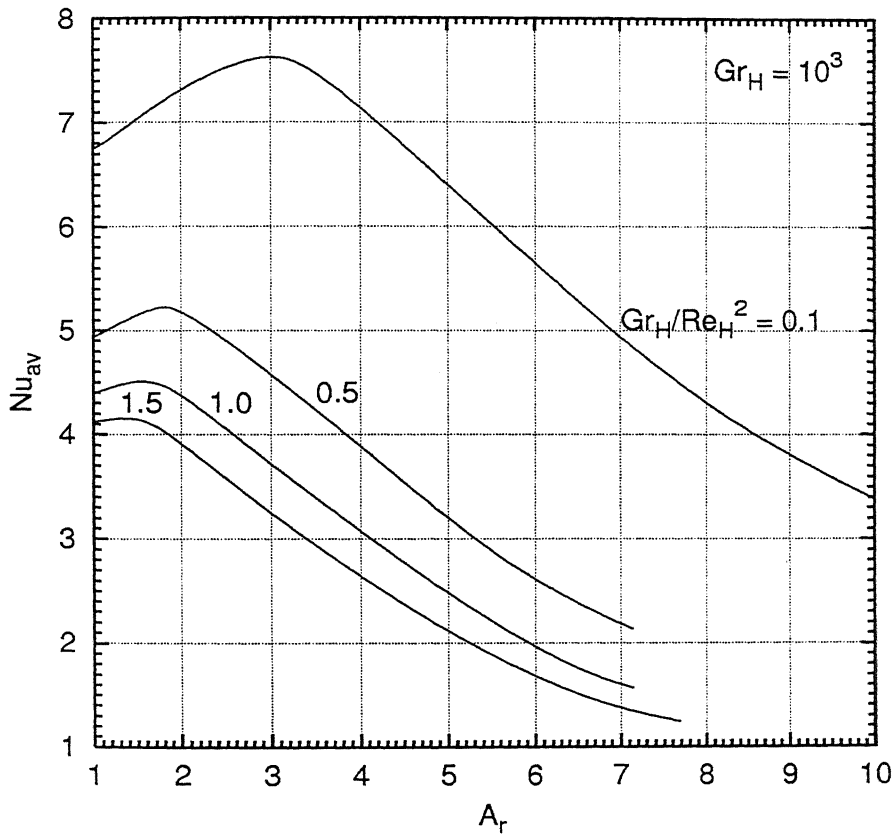


Figure 4.21: Variation of average Nusselt number with aspect ratio and buoyancy parameter,  $Gr_H/Re_H^2$ , at  $Gr_H = 10^3$ , for the case of mixed convection.



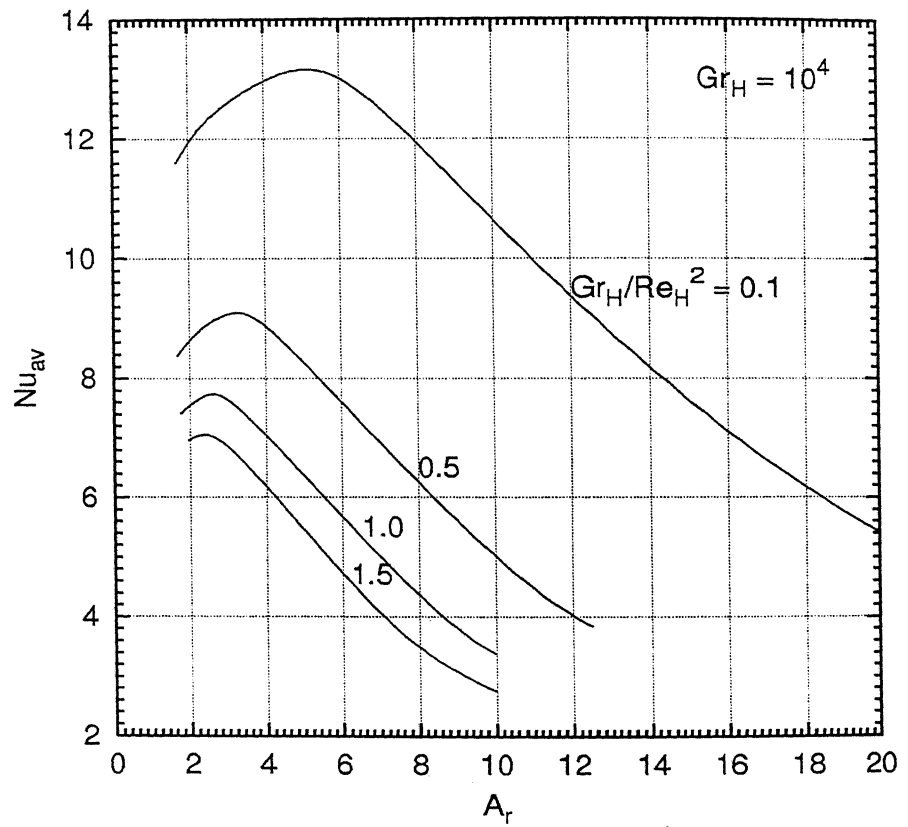


Figure 4.22: Variation of average Nusselt number with aspect ratio and buoyancy parameter,  $Gr_H/Re_H^2$ , at  $Gr_H = 10^4$ , for the case of mixed convection.

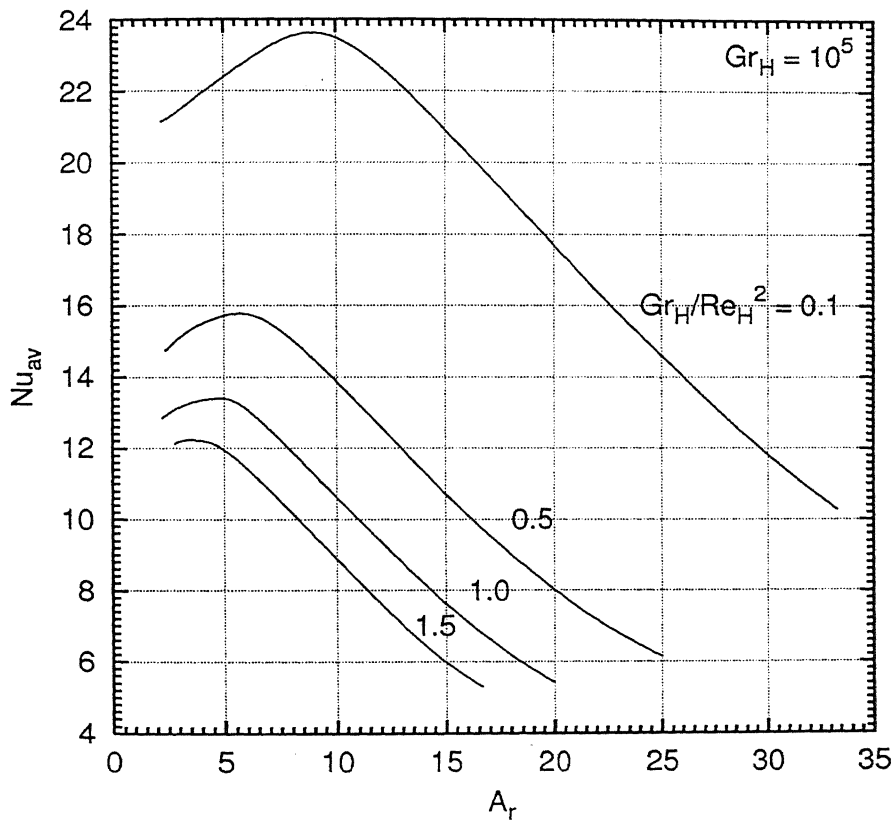


Figure 4.23: Variation of average Nusselt number with aspect ratio and buoyancy parameter,  $Gr_H/Re_H^2$ , at  $Gr_H = 10^5$ , for the case of mixed convection.

### Multiple Channel Case

As was elucidated in Section 2.7, the optimum spacing for the multiple channel case is the one that maximises the product  $Nu_{av}A_r$ . However, in the mixed convection  $Nu_{av}A_r$  reaches a maximum as  $A_r$  tends to infinity in the limit of small plate-to-plate spacing.

The reason for this is evident when we consider that  $U_o$  remains fixed for all inter-plate spacing. So the flow rate per unit width of the channel remains fixed. Yet when the spacing becomes small, the outflow temperature will tend to reach its maximum which is  $\theta = 1$ , i.e., ( $T = T_w$ ). So if we quantify the problem, the average heat transfer coefficient is,

$$h_{av} = \frac{1}{(T_w - T_\infty)H} \int_0^H q_w dx$$

where,  $q_w$  is the local wall heat flux.

For the symmetrically heated walls case, the overall rate of heat transfer rate to the channel,  $Q_{ch}$  is given by

$$Q_{ch} = 2 \int_0^H q_w dx$$

Therefore,

$$h_{av} = \frac{Q_{ch}}{2(T_w - T_\infty)H}$$

As the plate-to-plate spacing,  $L$  tends to zero, the fluid within the channel gets heated to almost wall temperature,  $T_w$ . Therefore,

$$\lim_{L \rightarrow 0} Q_{ch} = \dot{m} c_p (T_w - T_\infty)$$

where the mass flow rate,  $\dot{m}$ , is given by

$$\dot{m} = \rho U_0 L$$

Therefore, when the spacing  $L \rightarrow 0$

$$h_{av} = \frac{\rho L c_p U_0}{2H}$$

The average Nusselt number,  $Nu_{av}$  is then given by

$$Nu_{av} = \frac{h_{av} H}{k} = \frac{Pr Re_H}{2A_r}$$

where  $k$  is the thermal conductivity of the fluid (air).

Thus,

$$\lim_{A_r \rightarrow \infty} Nu_{av} = \frac{Pr Re_H}{2A_r} \quad (4.3)$$

So in the limit of large  $A_r$ ,  $Nu_{av} A_r$  tends to become a known constant. This can serve as a check for the accuracy of our simulation in the mixed convection case. Table 4.19 shows the limiting values of  $Nu_{av} A_r$  obtained in the computation compared with the corresponding theoretical values. The comparison is quite good, indicating the accuracy of the computation.

Figures 4.24, 4.25, and 4.26 show the product  $Nu_{av} A_r$  versus  $A_r$  for the various buoyancy parameter and for different Grashof numbers ( $Gr_H = 10^3, 10^4$ , and  $10^5$ ). The Table 4.20 shows the aspect ratio  $(A_r)_{min.opt}$  beyond which the value of  $Nu_{av} A_r$  falls within 3% of the maximum value. Thus, any aspect ratio which is equal to or greater than the given values of  $(A_r)_{min.opt}$  in Table 4.20 would be close to optimum, from the point of view of heat transfer. However, an increase in aspect ratio would cause a greater penalty, due to the higher pressure drop in a narrower channel. So it would be better to keep the aspect ratio very close to  $(A_r)_{min.opt}$  in a practical situation.

Table 4.19: Comparison of the theoretical and numerical values of the maximum product of average Nusselt number and aspect ratio for different Grashof numbers and buoyancy parameters

$Gr_H$	$\frac{Gr_H}{Re_H^2}$	$(Nu_{av} A_r)_{max}$	
		Theoretical	Numerical
$10^3$	0.1	35.00	34.27
	0.5	15.65	15.62
	1.0	11.07	11.19
	1.5	9.04	9.55
$10^4$	0.1	110.68	108.37
	0.5	49.50	48.05
	1.0	35.00	33.84
	1.5	28.58	27.58
$10^5$	0.1	350.00	343.53
	0.5	156.52	153.69
	1.0	110.68	108.39
	1.5	90.37	88.35

Table 4.20: Optimum aspect ratio for different Grashof numbers and buoyancy parameters: multiple channel case

$Gr_H$	$(A_r)_{min.opt}$			
	$\frac{Gr_H}{Re_H^2} = 0.1$	$\frac{Gr_H}{Re_H^2} = 0.5$	$\frac{Gr_H}{Re_H^2} = 1.0$	$\frac{Gr_H}{Re_H^2} = 1.5$
$10^3$	6.67	5.00	4.00	3.33
$10^4$	10.00	6.67	5.56	5.00
$10^5$	25.00	12.50	10.00	8.33

### 4.2.3 Pressure Drop

In the case of mixed convection there is a pressure drop expected between the inlet and the outlet of the channel. The numerical computation allow the pressure drop to be calculated by a balance between the viscous, inertial and buoyancy forces using

$$\Delta P_{av} = \frac{Gr_H}{Re_H^2} \left[ \int_0^{\frac{1}{A_r}} U^2 |_{X=1+\epsilon_l} dY - \int_0^{\frac{1}{A_r}} U^2 |_{X=0} dY + \int_0^{1+\epsilon_l} \int_0^{\frac{1}{A_r}} \theta dX dY \right] + \frac{\sqrt{Gr_H}}{Re_H^2} \left[ \int_0^{1+\epsilon_l} \frac{\partial U}{\partial Y} |_{Y=0} dX - \int_0^{1+\epsilon_l} \frac{\partial U}{\partial Y} |_{Y=\frac{1}{A_r}} dX \right] \quad (4.4)$$

where,  $\Delta P_{av}$  is the nondimensionalised pressure ( $= \frac{\Delta p}{\rho U_0^2}$ ). The value  $X = 1 + \epsilon_l$  appearing in the integral limits denotes the entrance to the computational domain which extends 10% of the channel height below the plates (i.e.,  $\epsilon_l = 0.1$ ). The pressure drop, obtained for various values of the buoyancy parameter and  $Gr_H = 10^3, 10^4$ , and  $10^5$  versus  $A_r$  is presented in Figure 4.27, 4.28, and 4.29. In all cases, it can be seen that the pressure drop is substantially less than what could be expected in the fully developed forced convection limit (which would be  $\Delta P_{av} = \frac{12A_r^2}{Re_H^2}$ ). Thus, buoyancy plays a very important role in reducing the pressure drop as compared to the forced convection case of equivalent  $Re_H$ .

The trends, for a given  $Gr_H$  and buoyancy parameter, in Figures 4.27, 4.28, and 4.29 are easily understandable. The pressure drop increases with the aspect ratio as a narrower channel would, obviously, cause an increased pressure drop. For a given  $Gr_H$  and fixed  $A_r$ , the  $\Delta P_{av}$  typically rises with increase in buoyancy parameter. This is because higher buoyancy parameter for fixed  $Gr_H$  corresponds to lower  $Re_H$  and hence greater frictional loss.

However, for some low aspect ratios,  $\Delta P_{av}$  actually decreases when the buoyancy parameter is increased from 0.5 to 1.0 and also from 1.0 to 1.5 in all the figures. This may seem to be anomalous. However, this too can be explained: at low aspect ratios the channel spacing is wide and the thermal boundary layers of the opposite walls do not meet within the channel. The thermal boundary layers for higher buoyancy parameters would be thicker

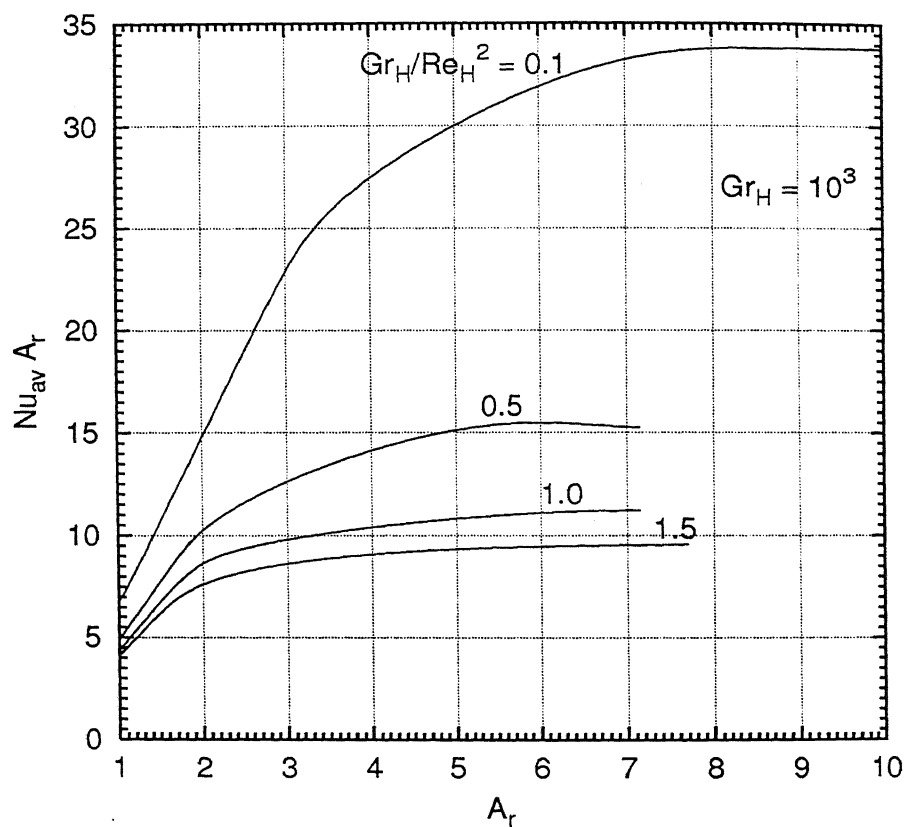


Figure 4.24: Variation of the product of average Nusselt number and aspect ratio with aspect ratio and buoyancy parameter,  $Gr_H/Re_H^2$ , at  $Gr_H = 10^3$ , for the case of mixed convection.

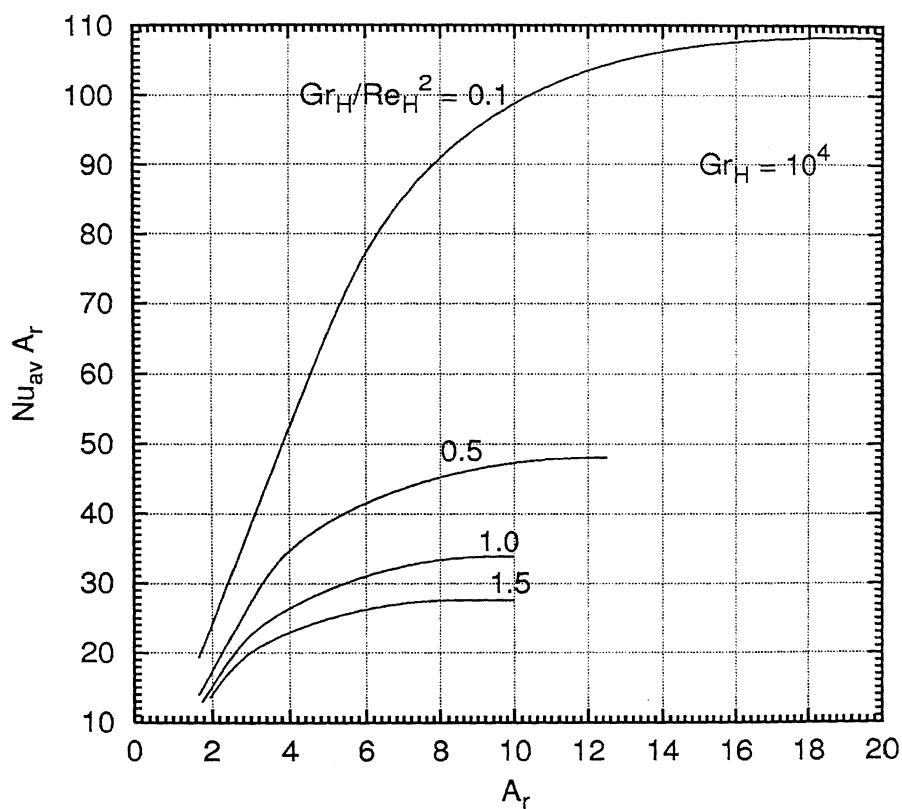


Figure 4.25: Variation of the product of average Nusselt number and aspect ratio with aspect ratio and buoyancy parameter,  $Gr_H / Re_H^2$ , at  $Gr_H = 10^4$ , for the case of mixed convection.



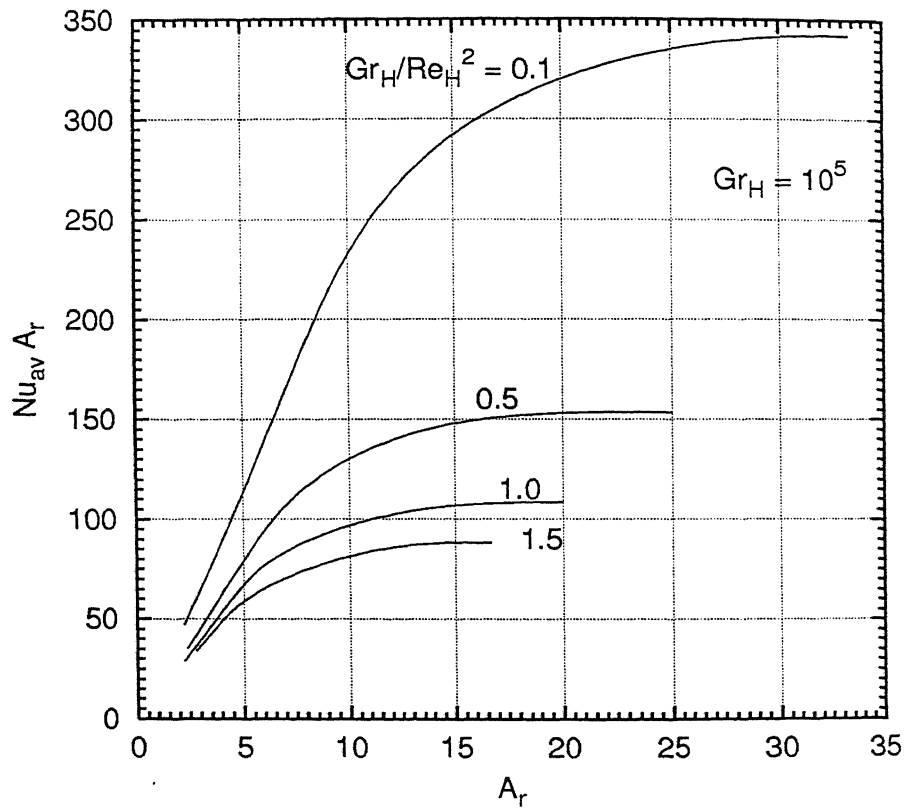


Figure 4.26: Variation of the product of average Nusselt number and aspect ratio with aspect ratio and buoyancy parameter,  $Gr_H / Re_H^2$ , at  $Gr_H = 10^5$ , for the case of mixed convection.

and, therefore, heat more of the channel fluid. The enhanced buoyancy effect due to this seems to more than compensate for the increased viscosity (i.e. lower Reynolds number) at higher buoyancy parameter values. This increased buoyancy leads to a decrease in the pressure drop required to impose the flow. However, this effect does not carry over for higher aspect ratios when the thermal boundary layers meet within the channel and the major portion of the channel fluid is anyway heated for all buoyancy parameter values.

#### 4.2.4 Flow Rates in Natural and Mixed Convection

The flow rate,  $\Delta\Psi$  for the natural convection case is compared with the mixed convection cases for various buoyancy parameters and for all  $Gr_H = 10^3, 10^4$ , and  $10^5$  in Figures 4.30, 4.31, and 4.32. In all cases, the  $\Delta\Psi$  is nondimensionalised as in the natural convection case for the sole purpose of comparison (i.e.,  $\Delta\Psi = \frac{\dot{v}}{\nu\sqrt{Gr_H}}$ , where  $\dot{v}$  is the volume flow rate per unit channel depth).

It can be seen that the mixed convection flow rates are higher than in the natural convection cases. This is expected, as the pressure drop is positive (i.e., the outlet pressure is lower than the inlet pressure) in the mixed convection cases, as shown in Figures 4.27, 4.28, and 4.29, compared to the zero pressure drop in the natural convection cases. The pressure thus partially forces the flow in mixed convection, yielding a higher volume flow rate.

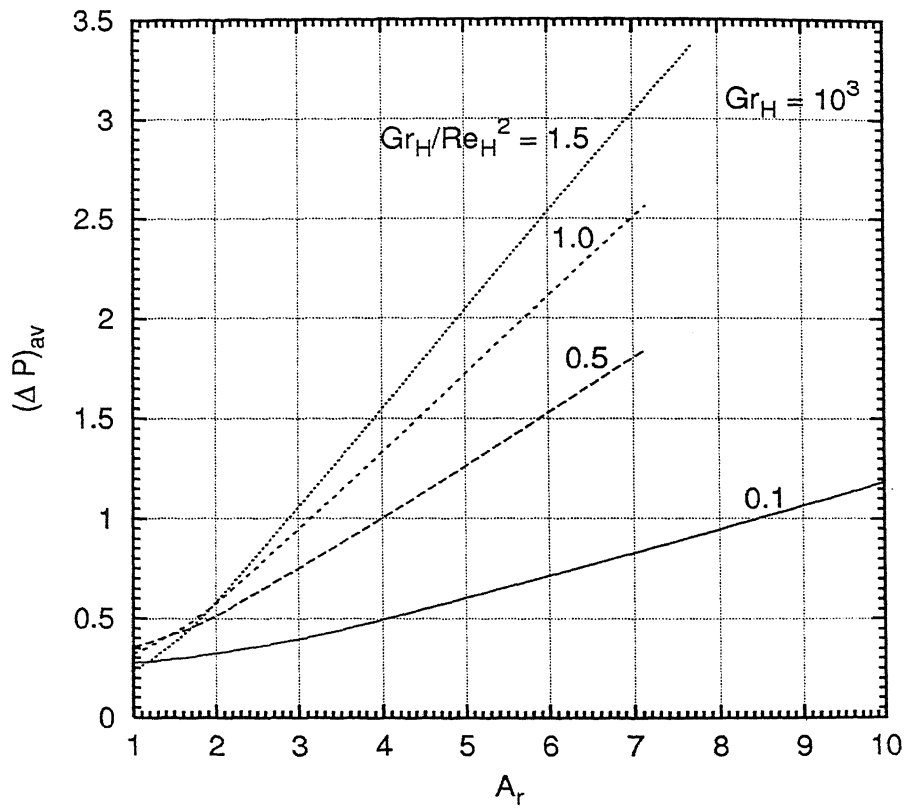


Figure 4.27: Variation of average pressure drop with aspect ratio and buoyancy parameter,  $Gr_H/Re_H^2$ , at  $Gr_H = 10^3$ , for the case of mixed convection.

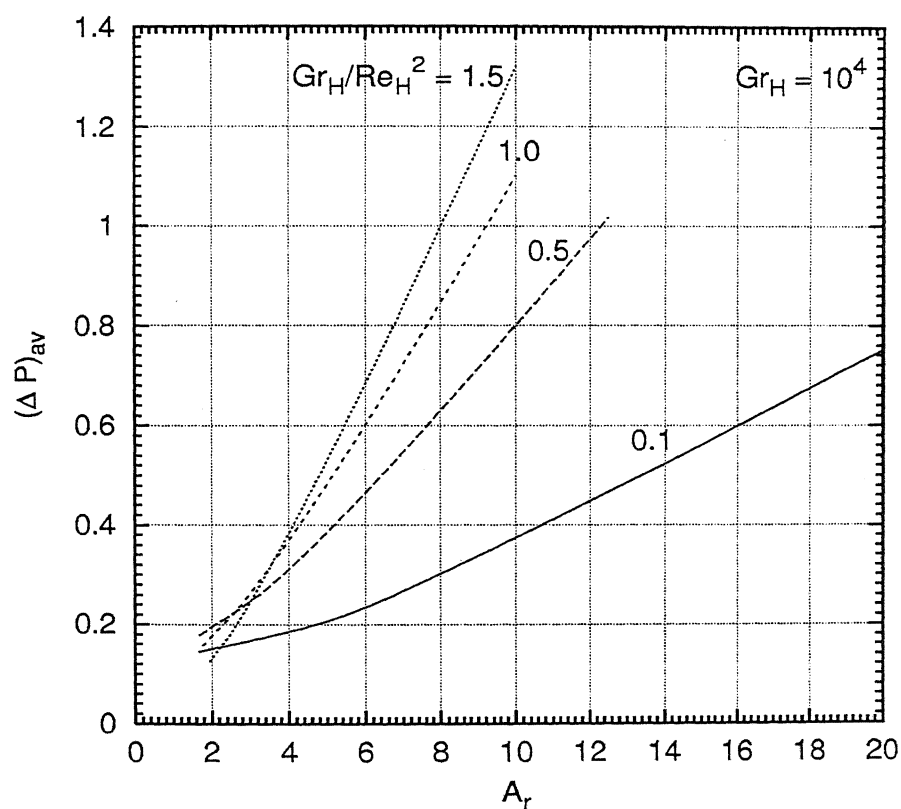


Figure 4.28: Variation of average pressure drop with aspect ratio and buoyancy parameter,  $Gr_H/Re_H^2$ , at  $Gr_H = 10^4$ , for the case of mixed convection.

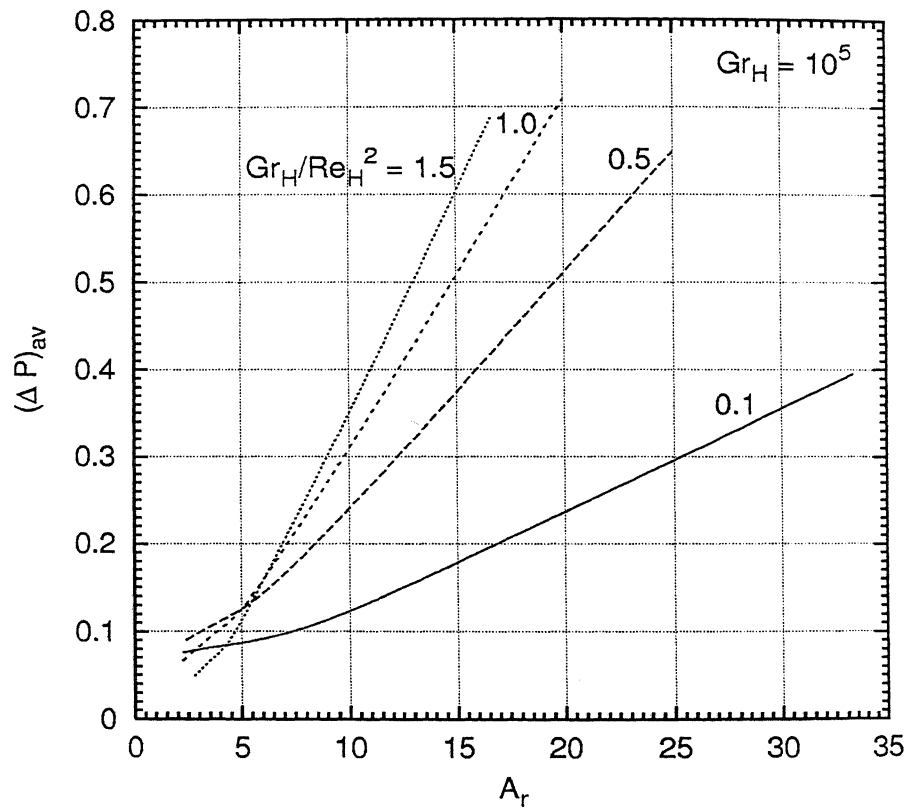


Figure 4.29: Variation of average pressure drop with aspect ratio and buoyancy parameter,  $Gr_H/Re_H^2$ , at  $Gr_H = 10^5$ , for the case of mixed convection.

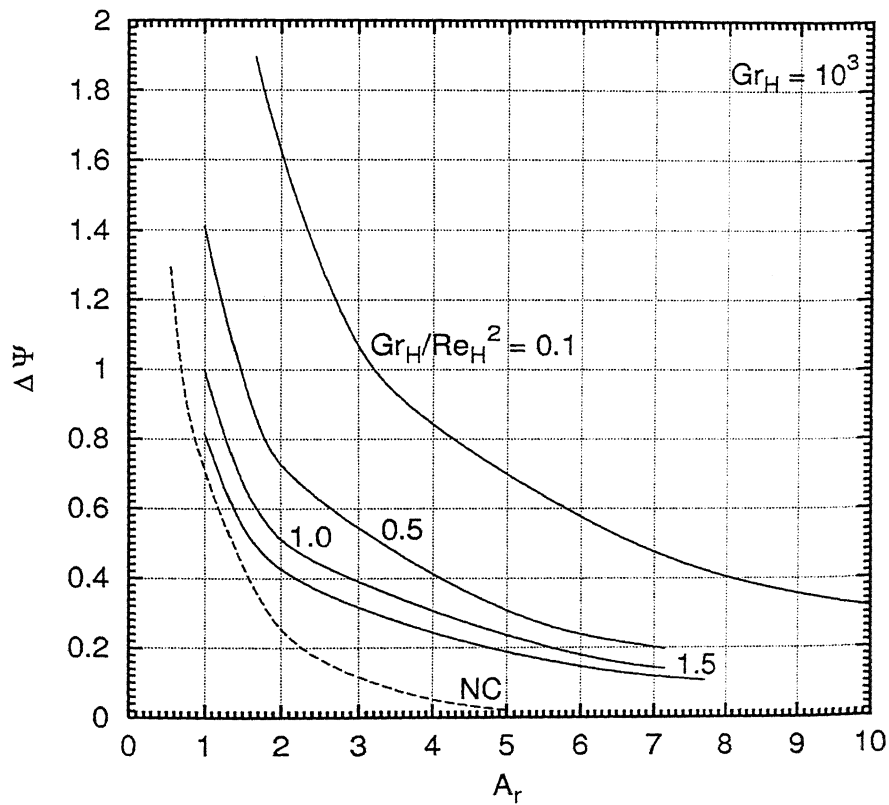


Figure 4.30: Variation of imposed volume flow rate with aspect ratio and buoyancy parameter,  $Gr_H/Re_H^2$ , at  $Gr_H = 10^3$  and their comparison with the induced volume flow rate in the natural convection case.

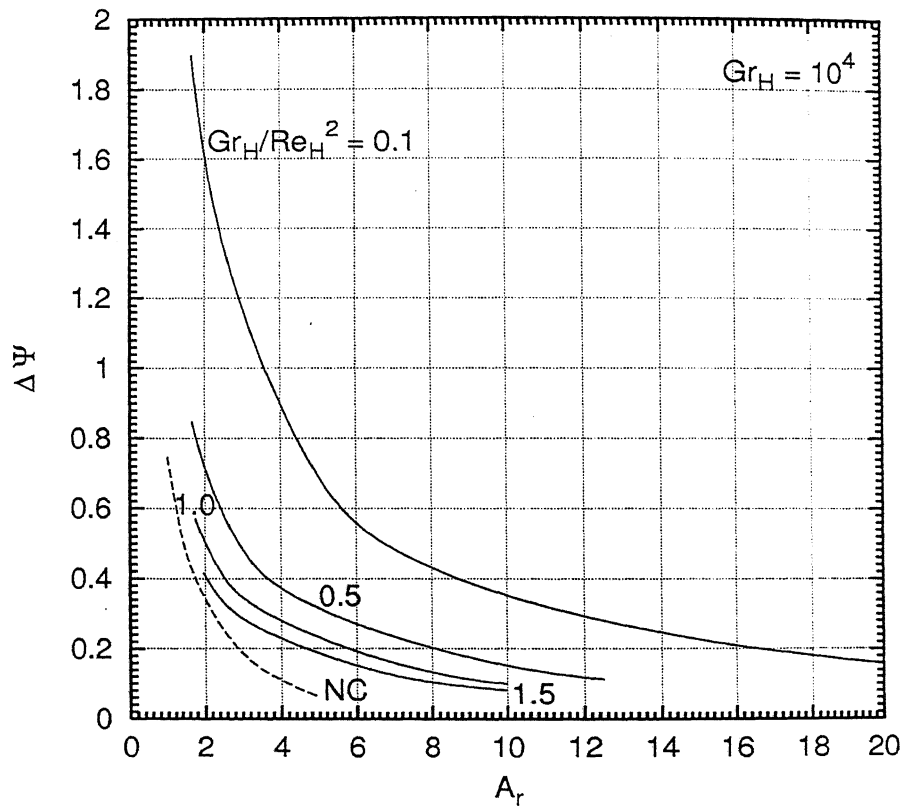


Figure 4.31: Variation of imposed volume flow rate with aspect ratio and buoyancy parameter,  $Gr_H/Re_H^2$ , at  $Gr_H = 10^4$  and their comparison with the induced volume flow rate in the natural convection case.

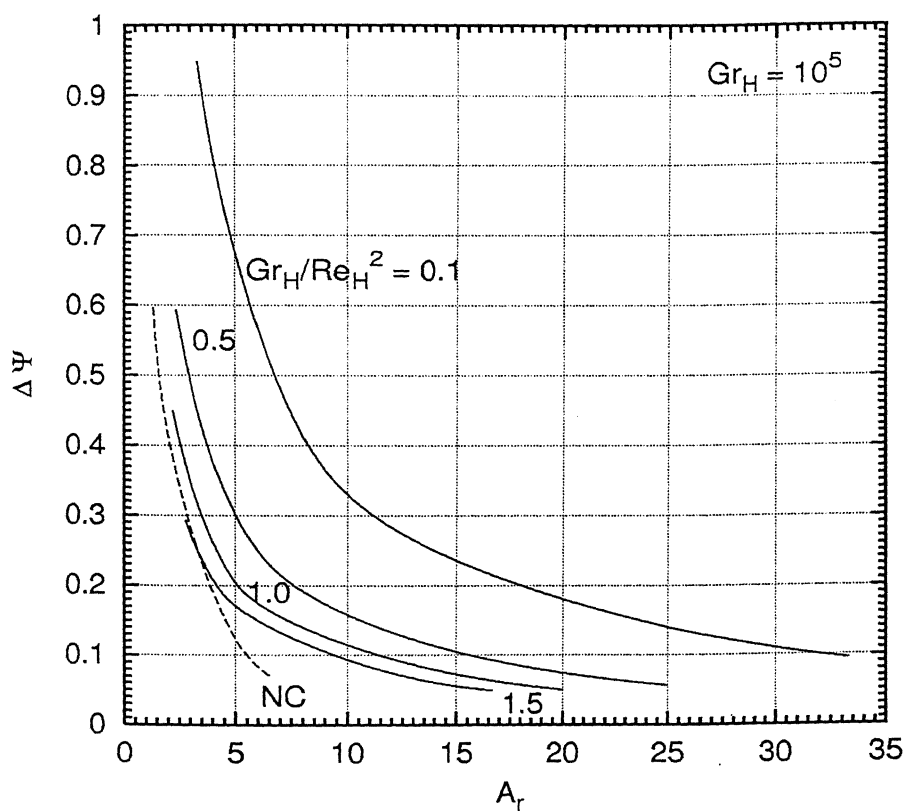


Figure 4.32: Variation of imposed volume flow rate with aspect ratio and buoyancy parameter,  $Gr_H/Re_H^2$ , at  $Gr_H = 10^5$  and their comparison with the induced volume flow rate in the natural convection case.





## Chapter 5

# Conclusions and Scope for Future Work

### 5.1 Conclusions

The determination of optimum spacing between heated vertical parallel plates mounted equidistantly in an array of specified volume is a fundamental thermal design problem associated with the efficient cooling of finned heat exchange surfaces, nuclear reactors and electronic packages. Despite these important applications, this problem had not been addressed for mixed convection cooling. Although a number of studies of this problem with natural convection cooling have been reported in the literature, the *volume constrained* optimisation of inter-plate spacing has not received attention. These unexamined aspects associated with optimisation of inter-plate spacing constitute the central motivation for the present investigation.

To simulate the air cooling of electronic packages, an array of vertical, parallel, equidistant electronic circuit boards with electronic components mounted on both sides of each board has been modelled as a series of symmetrically heated, vertical, equal-spaced smooth parallel plates maintained uniformly at constant temperature. There can exist two different optimum inter-plate spacings such that the overall heat transfer is maximum. One corresponds to plates arranged in a constrained volume, whereas the other is associated with plates in an unconstrained volume. The latter optimum

spacing is essentially applicable to a single channel formed by a pair of symmetrically heated vertical parallel plates. Consideration is given in this thesis to both constrained volume as well as unconstrained volume optimisation of inter-plate spacing.

The optimum inter-plate spacing both for natural as well as mixed convection cooling have been determined by numerically obtaining the flow and thermal fields between two adjacent plates. The numerical results have been presented and discussed for a range of Grashof numbers (for natural convection cooling), and combinations of Grashof number and buoyancy parameter ( $\equiv Gr_H/Re_H^2$ ) values (for mixed convection cooling), for a fluid Prandtl number of 0.70. On the basis of the results, the following qualitative conclusions can be drawn:

1. The optimum spacing is intimately related to the boundary layer thickness at the two plates. The optimum spacing is typically reached at a configuration where the boundary layers meet well within the channel.
2. The volume constrained optimum spacing is lower than the volume unconstrained optimum, in all cases.
3. In natural convection cooling, the volume constrained optimum is stronger (i.e., more clearly evident), while in mixed convection it is the volume unconstrained optimum that is so.
4. In mixed convection, the volume constrained spacing attains an asymptotic optimum value as the spacing tends to zero. Beyond a limit, decreases in inter-plate spacing results in higher pressure-drop without significant increase in overall heat transfer.
5. The weak optimum at finite spacing (rather than an asymptotic optimum at infinity) seen in natural convection is possibly due to the 'chimney effect'.
6. For natural convection cooling, the optimum spacing decreases with increasing Grashof number. This is true for both volume constrained as well as volume unconstrained optimisation. The maximum Nusselt numbers attained at the optima are strongly and positively correlated

with the Grashof number.

7. For mixed convection cooling, both optimum spacings decrease with increasing Grashof number, for a fixed buoyancy parameter value. The maximum Nusselt numbers attained are strongly and positively correlated with the Grashof number.
8. For mixed convection cooling, both optimum spacings increase with increasing buoyancy parameter values, for a fixed Grashof number. The maximum Nusselt numbers attained are strongly and inversely correlated with the buoyancy parameter value (and thus strongly and positively correlated with the Reynolds number).

The quantitative results for specific parameter values are in Chapter 4.

## 5.2 Scope of Future Work

The aspects to be considered in the study of heated parallel plate channels are many, and greatly depend on the physical model involved. In the present investigation, the mathematical model has been obtained on the basis of certain approximations and idealisations presented in Section 2.3. Although, the present study brings out many important features related to thermal optimisation of spacing between heated parallel plates, the deviation of the present model from realistic applications in electronic cooling needs to be examined in future work. In the light of this, future research may be along the following lines:

1. The problem of optimum spacing between electronic circuit boards with mounted components may be further studied by modelling them as heated plates with either protruding type or flush-mounted discrete heat sources. This problem can be studied for both natural as well as mixed convection cooling, with either constant heat flux or constant temperature wall conditions.

2. Certain classes of electronic packages are composed of circuit boards having components mounted on only one side of each board. Such electronic packages can be modelled as a series of asymmetrically heated plate channels. Taking one wall of each channel to be either at uniform wall temperature or with uniform heat flux, and the other wall to be insulated, the problem of optimum spacing can be studied for natural and mixed convection. This problem also can be extended by considering discrete heat sources, as suggested above.
3. In certain situations, the heated parallel plate channels may be modelled by plates with finite thickness and thermal conductivity. Under such situations, the heat generated on the surface of the plates will not be removed by convection alone but will also be conducted through the walls to the adjacent channels. Thus, the problem of optimum spacing of plates cooled by natural, mixed or forced convection can be studied by considering the heat transfer interactions with the neighbouring channels.
4. Most of the previous studies on optimum spacing, including the present one, invoke the Boussinesq approximation and assume constant thermophysical properties. However, in the cooling of heat generating nuclear fuel plates, for example, these assumptions are invalid. Therefore, the effect of variable properties, etc, on the optimum spacing problem could be investigated for such situations.

# Bibliography

1. Acharya, S. and Mehrotra, A. (1993), Natural Convection Heat Transfer in Smooth and Ribbed Vertical Channels, *Int. J. Heat Mass Transfer*, **36**, 236-241.
2. Akbari, H. and Borgers, T.R. (1979), Free Convective Laminar Flow Within the Trombe Wall Channel, *Solar Energy*, **22**, 165-174.
3. Amon, C.H. (1995), Spectral Element-Fourier Method for Unsteady Conjugate Heat Transfer in Complex Geometry Flows, *J. Thermophys. Heat Transfer*, **9**, 247-253.
4. Amon, C.H. (1995), Spectral Element-Fourier Method for Transition Flow in Complex Geometries, *AIAA Journal*, **31**, 42-48.
5. Amon, C.H. and Mikic, B.B. (1991), Spectral Element Simulation of Unsteady Forced Convective Heat Transfer: Application to Compact Heat Exchanger Geometries, *Numer. Heat Transfer, Part A*, **19**, 1-19.
6. Anand, N.K., Kim, S.H. and Aung, W. (1990), Effect of Wall Conduction on Free Convection Between Asymmetrically Heated Vertical Plates: Uniform Wall Temperature, *Int. J. Heat Mass Transfer*, **33**, 1025-1028.
7. Anand, N.K., Kim, S.H. and Fletcher, L.S. (1992), The Effect of Plate Spacing on Free Convection Between Heated Parallel Plates, *ASME J. Heat Transfer*, **114**, 515-518.
8. Anderson, D.A., Tannehill, J.C. and Pletcher, R.H. (1984), *Computational Fluid Mechanics and Heat Transfer*, Hemisphere, Washington, DC.

9. Aung, W. (1972), Fully Developed Laminar Free Convection Between Vertical Plates Heated Asymmetrically, *Int. J. Heat Mass Transfer*, **15**, 1577-1580.
10. Aung, W., Fletcher, L.S. and Sernas, V. (1972), Developing Laminar Free Convection Between Vertical Flat Plates with Asymmetric Heating, *Int. J. Heat Mass Transfer*, **15**, 2293-2308.
11. Aung, W. (1987), Mixed Convection in Internal Flow, in: Kakac, S., Shah, R.K. and Aung, W., eds., *Handbook of Single-Phase Convective Heat Transfer*, Wiley, New York, Chap.15.
12. Aung, W. and Worku, G. (1986a), Developing Flow and Flow Reversal in a Vertical Channel With Asymmetric Wall Temperatures, *ASME J. Heat Transfer*, **108**, 299-304.
13. Aung, W. and Worku, G. (1986b), Theory of Fully Developed, Combined Convection Including Flow Reversal, *ASME J. Heat Transfer*, **108**, 485-488.
14. Aung, W. and Worku, G. (1987), Mixed Convection in Ducts With Asymmetric Wall Heat Fluxes, *ASME J. Heat Transfer*, **109**, 947-951.
15. Baek, B.J., Plaski, D.A., Armaly, B.F. and Chen, T.S. (1990), Mixed Convection in an Asymmetrically Heated Vertical Parallel Plate Duct Flow, *Heat Transfer* 90, Proc. Ninth Int. Heat Transfer Conf., Jerusalem, Israel, **2**, 369-374.
16. Bar-Cohen, A. and Rohsenow, W.M. (1984), Thermally Optimum Spacing of Vertical, Natural Convection Cooled, Parallel Plates, *ASME J. Heat Transfer*, **106**, 116-123.
17. Barletta, A. (1998), Laminar Mixed Convection With Viscous Dissipation in a Vertical Channel, *Int. J. Heat Mass Transfer*, **41**, 3501-3513.
18. Barletta, A. (1999), Analysis of Combined Forced and Free Flow in a Vertical Channel With Viscous Dissipation and Isothermal Isoflux Boundary Conditions, *ASME J. Heat Transfer*, **121**, 349-456.
19. Bejan, A. (1995), *Convection Heat Transfer*, 2nd ed., John Wiley, New York.

20. Bejan, A., Morega, A.M., Lee, S.W. and Kim, S.J. (1993), The Cooling of Heat-Generating Board Inside a Parallel Plate Channel, *Int. J. Heat and Fluid Flow*, **14**, 170-176.
21. Bejan, A. and Sciubba, E. (1992), The Optimal Spacing of Parallel Plates Cooled by Forced Convection, *Int. J. Heat Mass Transfer*, **35**, 3259-3264.
22. Bodoia, J.R. and Osterle, J.F. (1962), The Development of Free Convection Between Heated Vertical Plates, *ASME J. Heat Transfer*, **84**, 40-44.
23. Burch, T., Rhodes, T. and Acharya, S. (1985), Laminar Natural Convection Between Finitely Conducting Vertical Plates, *Int. J. Heat Mass Transfer*, **28**, 1173-1186.
24. Cai, W., Lee, H.C. and Oh, H.-S. (1993), Coupling of Spectral Methods and the p-Version of the Finite Element Method for Elliptic Boundary Value Problems Containing Singularities, *J. Comput. Phys.*, **108**, 314-326.
25. Campo, A., Manca, O. and Morrone, B. (1999), Numerical Analysis of Partially Heated Vertical Parallel Plates in Natural Convection Cooling, *Numer. Heat Transfer, Part A*, **36**, 129-151.
26. Canuto, C., Hussaini, M.Y., Quarteroni, A. and Zang, T.A. (1988), *Spectral Methods in Fluid Dynamics*, Springer-Verlag, New York.
27. Carpenter, J.R., Briggs, D.G. and Sernas, V. (1976), Combined Radiation and Developing Laminar Free Convection Between Vertical Flat Plates With Asymmetric Heating, *ASME J. Heat Transfer*, **98**, 95-100.
28. Chang, T.S. and Lin, T.F. (1989), Transient Buoyancy-Induced Flow Through a Heated, Vertical Channel of Finite Height, *Numer. Heat Transfer, Part A*, **16**, 15-35.
29. Chang, T.S. and Lin, T.F. (1990), On the Reversed Flow and Oscillating Wake in an Asymmetrically Heated Channel, *Int. J. Numer. Methods Fluids*, **10**, 443-459.



30. Chappadi, P.R. and Eno, B.E. (1990), A Comparative Study of the Effect of Inlet Conditions on a Free Convection Flow in a Vertical Channel, *ASME J. Heat Transfer*, **112**, 1082-1085.
31. Cheng, C.-H., Kou, H.-S. and Huang, W.-H. (1990), Flow Reversal and Heat Transfer of Fully Developed Mixed Convection in Vertical Channels, *J. Thermophys. Heat Transfer*, **4**, 375-383.
32. Chow, L.C., Husain, S.R. and Campo, A. (1984), Effects of Free Convection and Axial Conduction on Forced Convection Heat Transfer Inside a Vertical Channel at Low Peclet Numbers, *ASME J. Heat Transfer*, **106**, 297-303.
33. Comini, G., Manzan, M., and Cortella, G. (1997), Open Boundary Conditions for the Stream Function-Vorticity Formulation of Unsteady Laminar Convection, *Numer. Heat Transfer, Part B*, **31**, 217-234.
34. Dalbert, A. M. (1982), Natural, Mixed and Forced Convection in a Vertical Channel With Asymmetric Uniform Heating, *Heat Transfer* 82, *Proc. Seventh Int. Heat Transfer Conf., Munich, west Germany*, **3**, 431-434.
35. Darie, E., Kimura, S. and Okajima, A. (1998), Natural Convection Heat Transfer in an Asymmetrically Heated Vertical Channel Controlled by Through Flows, *JSME Int. J., Series B*, **41**, 227-232.
36. Elenbaas, W. (1942), Heat Dissipation of Parallel Plates by Free Convection, *Physica*, **9**, 1-28.
37. Elperin, T. and Rudin, G. (1995), Temperature Field in a Multilayer Assembly Affected by a Local Laser Heating, *Int. J. Heat Mass Transfer*, **38**, 3143-3147.
38. Floryan, J. M. and Novak, M. (1995), Free Convection Heat Transfer in Multiple Vertical Channels, *Int. J. Heat and Fluid Flow*, **16**, 244-253.
39. Fowler, A.J., Ledezma, G.A. and Bejan, A. (1997), Optimum Geometric Arrangement of Staggered Plates in Forced Convection, *Int. J. Heat Mass Transfer*, **40**, 1795-1805.

40. Fujii, M., Tomimura, T., Zhang, X. and Gima, S. (1994), Natural Convection from an Array of Vertical Parallel Plates, *Heat Transfer* 94, Proc. Tenth Int. Heat Transfer Conf., Brighton, UK, 7, 49-54.
41. Garimella, S.V. and Schlitz. D.J. (1995), Heat Transfer Enhancement in Narrow Channels Using Two and Three-Dimensional Mixing Devices, *ASME J. Heat Transfer*, 117, 590-596.
42. Gau, C., Yih, K.A. and Aung, W. (1992), Measurements of Heat Transfer and Flow Structure in Heated Vertical Channels, *J. Thermophys. Heat Transfer*, 6, 707-712.
43. Gau, C., Yih, K.A. and Aung, W. (1992), Reversed Flow Structure and Heat Transfer Measurements for Buoyancy-Assisted Convection in a Heated Vertical Duct, *ASME J. Heat Transfer*, 114, 928-935.
44. Gebhart, B. (1971), *Heat Transfer*, 2nd ed., McGraw-Hill, New York.
45. Gebhart, B., Jaluria, Y., Mahajan, R.L. and Sammakia, B. (1988), *Buoyancy-Induced Flows and Transport*, Hemisphere, Washington, DC.
46. Ghaddar, N.K., Karniadakis, G.E. and Patera, A.T. (1986), A Conservative Isoparametric Spectral Element Method for Forced Convection; Application to Fully Developed Flow in Periodic Geometries, *Numer. Heat Transfer*, 9, 277-300.
47. Gray, D.D. and Giorgini, A. (1976), The Validity of the Boussinesq Approximation for Liquid and Gases, *Int. J. Heat Mass Transfer*, 19, 545-551.
48. Guo, B.-Y. and Cao, W.-M. (1992), A Combined Spectral-Finite Element Method for Solving Two Dimensional Unsteady Navier-Stokes Equations, *J. Comput. Phys.*, 101, 375-385.
49. Guo, Z.-Y. and Wu, X.-B. (1993), Thermal Drag and Critical heat Flux for Natural Convection of Air in Vertical Parallel Plates, *ASME J. Heat Transfer*, 115, 124-129.
50. Habchi, S. and Acharya, S. (1986), Laminar Mixed Convection in a Symmetrically or Asymmetrically Heated Vertical Channel, *Numer. Heat Transfer*, 9, 605-618.

51. Hamadah, T. T. and Wirtz, R.A. (1991), Analysis of Laminar Fully Developed Mixed Convection in a Vertical Channel With Opposing Buoyancy, *ASME J. Heat Transfer*, **113**, 507-510.
52. Hernandez, J., Zamora, B. and Campo, A. (1994), on the Effect of Prandtl Number and Aspect Ratio upon Laminar Natural-Convection Flows in Vertical Channels Heat Transfer 1994, *Proc. Tenth Int. Heat Transfer Conf.*, Brighton, UK, **5**, 483-488.
53. Huang, P.C., and Vafai, K. (1994), Internal Heat Transfer Augmentation in a Channel Using an Alternate Set of Porous Cavity-Block Obstacles, *Numer. Heat Transfer, Part A*, **5**, 519-539.
54. Incropera, F.P. (1988), Convection Heat Transfer in Electronic Equipment Cooling, *ASME J. Heat Transfer*, **110**, 1097-1111.
55. Ingham, D.B., Keen, D.J., and Heggs, P.J. (1988a), Two Dimensional Combined Convection in Vertical Parallel Plate Ducts, Including Situations of Flow Reversal, *Int. J. Numer. Methods.Eng.*, **26**, 1645-1664.
56. Ingham, D.B., Keen, D.J. and Heggs, P.J. (1988b), Flows in Vertical Channels with Asymmetric Wall Temperatures and Including Situations Where Reverse Flows Occur, *ASME J. Heat Transfer*, **110**, 910-917.
57. Jaluria, Y. (1980), *Natural Convection Heat and Mass Transfer*, Pergamon Press, New York.
58. Jaluria, Y. (1987), Basics of Natural Convection, in Kakac, S., Shah, R.K; and Aung, W., eds., *Handbook of Single Phase Convective Heat Transfer*, Wiley, New York Chap.12.
59. Jaluria, Y. and Torrance, K.E. (1986), *Computational Heat Transfer*, Hemisphere, Washington, DC.
60. Jeng, Y.N., Chen, J.L. and Aung, W. (1992), On the Reynolds-Number Independence of Mixed Convection in a Vertical Channel Subjected to Asymmetric Wall Temperatures With and Without Flow Reversal, *Int. J. Heat and Fluid Flow*, **13**, 329-339.

61. Jones, A.T. and Ingham, D.B. (1993), Combined Convection Flow in a Vertical Duct With Wall Temperatures That Vary Linearly With Depth, *Int. J. Heat and Fluid Flow*, **14**, 37-47.
62. Jones, A.T. and Ingham, D.B. (1994), Combined Convection Flow and Heat Transfer to a Power Law Fluid in a Vertical Duct, Including Reverse Flow Situations, *Numer. Heat Transfer, Part A*, **25**, 57-73.
63. Joshi, H.M. (1988), Transient Effects in Natural Convection cooling of Vertical Parallel Plates, *Int. Comm. Heat Mass Transfer*, **15**, 227-238.
64. Kettleborough, C.F. (1972), Transient Laminar Free Convection Between Heated Vertical Plates Including Entrance Effects, *Int. J. Heat Mass Transfer*, **15**, 883-895.
65. Kihm, K.D., Kim, J.H. and Fletcher, L.S. (1995), Onset of Flow Reversal and Penetration Length of Natural Convective Flow Between Isothermal Vertical Walls, *ASME J. Heat Transfer*, **117**, 776-779.
66. Kim, S.H., Anand, N.K. and Aung. W. (1990), Effect of Wall Conduction on Free Convection Between Asymmetrically Heated Vertical Plates: Uniform Wall Heat Flux, *Int. J. Heat Mass Transfer*, **33**, 1013-1023.
67. Kim, S.H., Anand, N.K. and Fletcher, L.S. (1991), Free Convection Between Series of Vertical Parallel Plates With Embedded Line Heat Sources, *ASME J. Heat Transfer*, **113**, 108-115.
68. Kim, S.J. and Lee, S.W., eds. (1996), *Air Cooling Technology for Electronic Equipment*, CRC Press, Boca Raton, FL.
69. Korczak, K.Z. and Patera, A.T. (1986), An Isoparametric Spectral Element Method for Solution of the Navier-Stokes Equations in Complex Geometry, *J. Comput. Phys.*, **62**, 361-382.
70. Langerman, M.A. (1993), A Non-Boussinesq Integral Method for Laminar Free Convection Between Vertical Flat Plates Subject to a Uniform Wall Heat Flux, *Int. J. Heat Mass Transfer*, **36**, 3429-3435.
71. Lee, K.-T. (1994), Natural Convection in Vertical Parallel Plates With an Unheated Entry or Unheated Exit, *Numer. Heat Transfer, Part A*, **25**, 477-493.

72. Ledezma, G.A. and Bejan, A. (1997), Optimal Geometric Arrangement of Staggered Vertical Plates in Natural Convection, *ASME J. Heat Transfer*, **119**, 700-708.
73. Levy, E.K. (1971), Optimum Plate Spacings for Laminar Natural Convection Heat Transfer From Parallel Vertical Isothermal Flat Plates, *ASME J. Heat Transfer*, Series C, **93**, 463-465.
74. Levy, E.K., Eichen, P.A., Cintani, W.R. and Shaw, R.R. (1975), Optimum Plate Spacings for Laminar Natural Convection Heat Transfer From Parallel Vertical Isothermal Flat Plates: Experimental Verification, *ASME J. Heat Transfer*, **97**, 474-476.
75. Lin, H.H. and Hung, Y.H. (1993), Transient Forced Convection Heat Transfer in a Vertical Rib-Heated Channel Using a Turbulence Promotor, *Int. J. Heat Mass Transfer*, **36**, 1553-1571.
76. Lin, T.F., Yin, C.P. and Yan, W.M. (1991), Transient Laminar Mixed Convective Heat Transfer in a Vertical Flat Duct, *ASME J. Heat Transfer*, **113**, 384-390.
77. Ma, H. (1993), A Spectral Element Basin Model for the Shallow Water Equations, *J. Comput. Phys.*, **109**, 133-149.
78. Manca et al. (2000), Natural Convection in Open Channels, in: Sunden B. and Comini G., eds., *Computational Analysis of Convection Heat Transfer*, WIT Press, Southampton, Chap.7.
79. Martin, L., Raithby, G.D. and Yovanovich, M.M. (1991), On the Low Rayleigh Number Asymptote for Natural Convection Through an Isothermal, Parallel Plate Channel, *ASME J. Heat Transfer*, **113**, 899-905.
80. Mereu, S., Sciubba, E., and Bejan, A. (1993), The Optimal Cooling of a Stack of Heat Generating Boards With Fixed Pressure Drop, Flowrate or Pumping Power, *Int. J. Heat Mass Transfer*, **36**, 3677-3686.
81. Middleman, S. (1998), *An Introduction to Mass and Heat Transfer: Principles of Analysis and Design*, John Wiley, New York.
82. Miyatake, O. and Fujii, T. (1972), Free Convective Heat Transfer Between Vertical Parallel Plates - One Plate Isothermally Heated and

- the Other Thermally Insulated, Heat Transfer - Japanese Research, **1**, 30-38.
83. Miyatake, O. and Fujii, T. (1973), Natural Convection Heat Transfer Between Vertical Parallel Plates at Unequal Uniform Temperatures, Heat Transfer-Japanese Research, **2**, 79-88.
  84. Miyatake, O. and Fujii, T. (1974), Natural Convective Heat Transfer Between Vertical Parallel Plates With Unequal Heat Fluxes, Heat Transfer-Japanese Research, **3**, 29-33.
  85. Miyatake, O., Fujii, T., Fujii, M., and Tanaka, H. (1973), Natural Convective Heat Transfer Between Vertical Parallel Plates - One Plate With a Uniform Heat Flux and the Other Thermally Insulated, Heat Transfer - Japanese Research, **2**, 25-33.
  86. Morega, A.M. and Bejan, A. (1994), Optimum Spacing of Parallel Boards With Discrete Heat Sources Cooled by Laminar Forced Convection, Numer. Heat Transfer, Part A, **25**, 373-392.
  87. Morega, A.M., Bejan, A. and Lee, S.W. (1995), Free Stream Cooling of a Stack of Parallel Plates, Int. J. Heat Mass Transfer, **38**, 519-531.
  88. Morrone, B., Campo, A. and Manca, O. (1997), Optimum Plate Separation in Vertical Parallel Plate Channels for Natural Convective Flows: Incorporation of Large Spaces at the Channel Extremes, Int. J. Heat Mass Transfer, **40**, 993-1000.
  89. Nakamura, H., Asako, Y., and Naitou, T. (1982), Heat Transfer by Free Convection Between Two Parallel Flat Plates, Numer. Heat Transfer, **5**, 95-106.
  90. Naylor, D., Floryan, J.M. and Tarasuk, J.D. (1991), A Numerical Study of Developing Free Convection Between Isothermal Vertical Plates, ASME J. Heat Transfer, **113**, 620-626.
  91. Nigen, J.S. and Amon, C.H. (1995), Effect of Material Composition and Localised Heat Generation on Time-Dependent Conjugate Heat Transport, Int. J. Heat Mass Transfer, **38**, 1565-1576.

92. Patankar, S.V. (1980), Numerical Heat Transfer and Fluid Flow, Hemisphere, Washington, DC.
93. Patera, A.T. (1984), A Spectral Element Method for Fluid Dynamics: Laminar Flow in a Channel Expansion, *J. Comput. Phys.*, **54**, 468-488.
94. Peterson, G.P. and Ortega, A. (1990), Thermal Control of Electronic Equipment and Devices, *Adv. Heat Transfer*, **20**, 181-314.
95. Pica, A.L., Rodono, G. and Volpes, R. (1993), An Experimental Investigation on Natural Convection of Air in a Vertical Channel, *Int. J. Heat Mass Transfer*, **36**, 611-616.
96. Prakash, S. (1995), Application of the Spectral Element Method to Buoyancy Driven Flows, M.Tech. Thesis, Dept. of Mechanical Engg., Indian Institute of Technology, Kanpur, India.
97. Quintiere, J. and Mueller, W.K. (1973), An Analysis of Laminar Free and Forced Convection Between Finite Vertical Parallel Plates, *ASME J. Heat Transfer*, **95**, 53-59.
98. Ramanathan, S. and Kumar, R. (1991), Correlations for Natural Convection Between Heated Vertical Plates, *ASME J. Heat Transfer*, **113**, 97-107.
99. Refai, G. and Yovanovich, M.M. (1992), Numerical study of Natural Convection from Discrete Heat Sources in a Vertical Square Enclosure, *J. Thermophys. Heat Transfer*, **6**, 121-127.
100. Roache, P.J. (1972), Computational Fluid Dynamics, Hermosa, Albuquerque, NM.
101. Roberts, D.A. and Floryan, J.M. (1998), Heat Transfer Enhancement in the Entrance Zone of a Vertical Channel, *ASME J. Heat Transfer*, **120**, 290-291.
102. Shahin, G.A. and Floryan, J.M. (1999), Heat Transfer Enhancement Generated by the Chimney Effect in System of Vertical Channels, *ASME J. Heat Transfer*, **121**, 230-232.

103. Shyy, W., Gingrich, W.K. and Gebhart, B. (1992), Adaptive Grid Solution for Buoyancy-Induced Flow in Vertical Slots, Numer. Heat Transfer, Part A, **22**, 51-70.
104. Shyy, W., Rao, M.M. (1993), Simulation of Transient Natural Convection Around an Enclosed Vertical Channel, ASME J. Heat Transfer, **115**, 946-954.
105. Sidilkover D. and Karniadakis, G.E. (1993), Non-Oscillatory Spectral Element Chebyshev Method for Shock Wave Calculations, J. Comput. Phys., **101**, 207-217.
106. Sparrow, E.M. and Azevedo, L.F.A. (1985), Vertical-Channel Natural Convection Spanning Between the Fully-Developed Limit and the Single Plate Boundary-Layer Limit, Int. J. Heat Mass Transfer, **28**, 1847-1857.
107. Sparrow, E.M. and Bahrami, P.A. (1980), Experiments on Natural Convection From Vertical Parallel Plates With Either Open or Closed Edges, ASME J. Heat Transfer, **102**, 221-227.
108. Sparrow, E.M., Chrysler, G.M., and Azevedo, L.F. (1984), Observed Flow Reversals and Measured-Predicted Nusselt Numbers for Natural Convection in a One-Sided Heated Vertical Channel, ASME J. Heat Transfer, **106**, 325-332.
109. Straatman, A.G., Tarasuk, J.D. and Floryan, J.M. (1993), Heat Transfer Enhancement From a Vertical Isothermal Channel Generated by the Chimney Effect, ASME J. Heat Transfer, **115**, 395-402.
110. Tao, L.N. (1960), On Combined Free and Forced Convection in Channels, ASME J. Heat Transfer, **82**, 233-238.
111. Taylov, M., Tribbia, J. and Iskandarani, M. (1997), The Spectral Element Method for the Shallow Water Equations on the Sphere, J. Comput. Phys., **130**, 92-108.
112. Waston, J.C., Anand, N.K., and Fletcher, L.S. (1996), Mixed Convective Heat Transfer Between a Series of Vertical Parallel Plates With Planar Heat Sources, ASME J. Heat Transfer, **118**, 984-990.



113. Webb, B.W. and Hill, D.P. (1989), High Rayleigh Number Laminar Natural Convection in an Asymmetrically Heated Vertical Channel, *ASME J. Heat Transfer*, **111**, 649-659.
114. Wirtz, R.A. and Stutzman, R.J. (1982), Experiments on Free Convection Between Vertical Plates With Symmetric Heating, *ASME J. Heat Transfer*, **104**, 501-507.
115. Yamada, Y. (1988), Combined Radiation and Free Convection Heat Transfer in a Vertical Channel With Arbitrary Wall Emissivities, *Int. Heat Mass Transfer*, **31**, 429-440.
116. Yan, W.-M. and Lee K.-T. (1995), Unsteady Conjugated Mixed Convection in a Vertical Channel, *ASME J. Heat Transfer*, **117**, 234-238.
117. Yao, L.S. (1983), Free and Forced Convection in the Entry Region of a Heated Vertical Channel, *Int. J. Heat Mass Transfer*, **26**, 65-72.
118. Zanchini, E. (1998), Effect of Viscous Dissipation on Mixed Convection in a Vertical Channel With Boundary Conditions of the Third Kind, *Int. J. Heat Mass Transfer*, **41**, 3949-3959.
119. Zhong, Z.Y., Yang, K.T. and Lloyd, J.R. (1985), Variable Property Effects in Laminar Natural Convection in a Square Enclosure, *ASME J. Heat Transfer*, **107**, 133-138.